UNIVERSITÄT PADERBORN
Die Universität der Informationsgesellschaft

FAKULTÄT FÜR NATURWISSENSCHAFTEN
DEPARTMENT CHEMIE

Alternative, environmentally friendly pretreatments on multi-metal constructions by organosilane-based conversion layers

DISSERTATION

VON

STEFAN BIRKENHEUER

AUS PADERBORN

Erstgutachter: Prof. Dr. Ing. Grundmeier

Zweitgutachter: Prof. Dr. Ing. Warnecke

PADERBORN 2012

Abstract

The present study deals with the spectroscopic, microscopic and electrochemical characterization of alternative conversion layers for application as adhesion promoters and anti-corrosion layers on multi-metal constructions. Since the “classic” system applied in the automotive industry is based on a tri-cationic zinc phosphatization, which contains environmentally harmful ions like nickel, the development of environmentally friendly systems has become the focus of recent research. Therefore, organosilane-based ultra-thin conversion layers applied on pure iron as well as on different commercial alloys were investigated in order to enhance their barrier properties and surface coverage as well as their corrosion inhibition properties, especially with respect to the deceleration of cathodic delamination at the metal/adhesive interface.

Therefore zirconia/γ-aminopropyltriethoxysilane (γ-APS) bilayer and hybrid systems were studied. The chemical compositions of the applied films were studied by means of Fourier-Transformed Infrared Reflection–Absorption Spectroscopy (FT-IRRAS) and X-ray Photoelectron Spectroscopy (XPS) while the morphologies of the bare surfaces and of the subsequently applied layers were studied by Field-Emission Secondary Electron Microscopy (FE-SEM) and Atomic Force Microscopy (AFM). In order to predict the behavior of these films in corrosive environments, the barrier properties and surface coverage were electrochemically studied by means of Electrochemical Impedance Spectroscopy (EIS), Cyclovoltammetry (CV) and Linear Sweep Voltammetry (LSV). Moreover, the cathodic delamination at the metal/conversion layer interface was investigated by means of a Height-Regulated Scanning Kelvin Probe (HR-SKP).

In order to improve the properties of the conversion layers, different post-treatments were studied, in addition to the effects of the incorporation of nanocontainers. Furthermore, the influence of physical process parameters like bath temperatures and stirring velocities were investigated.

Danksagung/Acknowledgement

Diese Arbeit entstand in der Zeit von Juli 2009 bis März 2012 im Department für Technische und Makromolekulare Chemie an der Universität Paderborn.

Ich möchte Herrn Prof. Dr.-Ing. Guido Grundmeier für die Aufnahme in seinen Arbeitskreis, sowie die Betreuung dieser Arbeit, sein stetes Interesse an ihrem Fortgang und für viele hilfreiche Diskussionen und Ideen bei der Lösung anspruchsvoller, wissenschaftlicher Fragestellungen herzlich danken.

Herrn Prof. Dr. Ing. Hans-Joachim Warnecke danke ich für die Übernahme des Koreferates, Herrn Prof. Dr. rer. nat. Michael Tiemann für den Vorsitz der Prüfungskommission sowie Herrn PD Dr. rer. nat. Hans Egold für die Tätigkeit als 3. Prüfer.

Allen Mitarbeitern der Technischen Chemie an der Universität Paderborn danke ich für die angenehme Atmosphäre und die stete Hilfsbereitschaft. Insbesondere danke ich Herrn M.Sc. Christian Kunze für die Durchführung von rasterkraftmikroskopischen und röntgenphotoelektonischen Analysen. Frau Dipl. Chem. Ing. Nadine Buitkamp und Frau M. Sc. Nora Pollmann danke ich für die Anfertigung von elektronenmikroskopischen Aufnahmen.

Darüber hinaus möchte ich meinen Projektpartnern, der Chemetall GmbH in Frankfurt a.M. und der BMW AG in München für die finanzielle und wissenschaftliche Unterstützung meiner Arbeit danken.

Mein ganz besonderer Dank gilt meinen Eltern für ihre langjährige Unterstützung. Ohne Sie wäre die Entstehung dieser Arbeit erst gar nicht möglich gewesen.

Content

1 General Introduction

1.1 Corrosion and passivity of metal substrates in corrosive environments

For the manufacture of metallic constructions, it is not only consideration of the mechanical properties of the materials used that needs to be in focus, but also economic aspects with respect to the costs of the raw materials. Therefore, the metals that are mainly used are widely available, easily convertible and possess chemical stabilities that are adequate or can easily be improved by additional treatments. Therefore iron, zinc, aluminium and their alloys are mostly used for industrial applications. However, all of these materials tend more or less to corrode depending on the environmental condition.

1.1.1 Chemical and electronic structures of passive films

In both wet and dry environments iron, zinc, aluminium and many other metals, like Nb, Ta, Ti, Zr and Hf, form passive layers on their surfaces which exhibit protective properties towards corrosive attacks.

These native passive films are usually oxides or oxyhydroxides of their substrates with a thickness of a few nanometers which can grow up to tens of nanometers due to the potential drops at the metal/metal oxide/electrolyte interfaces. They cause an electrical field strength of up to some 10^6 V/cm which enables ion migration through the passive film and thereby further film growth. The chemical structures of passive films are often complex and show several differences to the corresponding crystalline oxides since their films are usually amorphous or nanocrystalline, show a high degree of hydration, and contain nanodefects in their matrices. Moreover, they form double or even multi-layers made of an ultra-thin protective oxide film on the metallic surface and thicker, hydroxide-richer and less protective layers above.[1-4] As a result, the oxidation state of the passive films advances from the metal/metal oxide interface to the metal oxide surfaces which can be additionally increased by anodic polarization.[5-7]

The electrically semi-conducting or insulating properties of the passive films are based on the band gap between the valence band and the conducting band. This range depends on their chemical structure. Amorphous oxide layers reveal smaller band gaps than crystalline oxides and also contain more intrinsic defects near to the band edge.

At appropriate pH these passive films are stable and become dissolved in strongly acidic or alkaline environments as described by the pH-potential diagrams of Pourbaix.[8,9] Some metals, like Fe, Ni and Cr, also reveal stability in very acidic solutions which are far away from the dissolution equilibrium of their passive films.[10] The reason for this is the kinetically inhibited dissolution of the passive film. Thus the passivity of these metals exists contradictory to the thermodynamics described by the Pourbaix diagrams.

1.1.2 Breakdown of passivity

The protective properties of passive films can be significantly removed or even eliminated under the attack of aggressive anions likes halides. A serious problem in this case is chloride which effectively attacks thin oxide layers and is present in many environments such as seawater and salt on roads. The breakdown of passivity is the initiating step of pitting corrosion on many metals like Fe, Ni, Cu or Al, whereas chromium is one of the few elements which are immune to pitting corrosion.

Three main mechanisms of the breakdown of passivity are discussed. These are: the penetration mechanism, the film-breaking mechanism and the adsorption mechanism, as illustrated in Figures 1.1–1.3.[11]

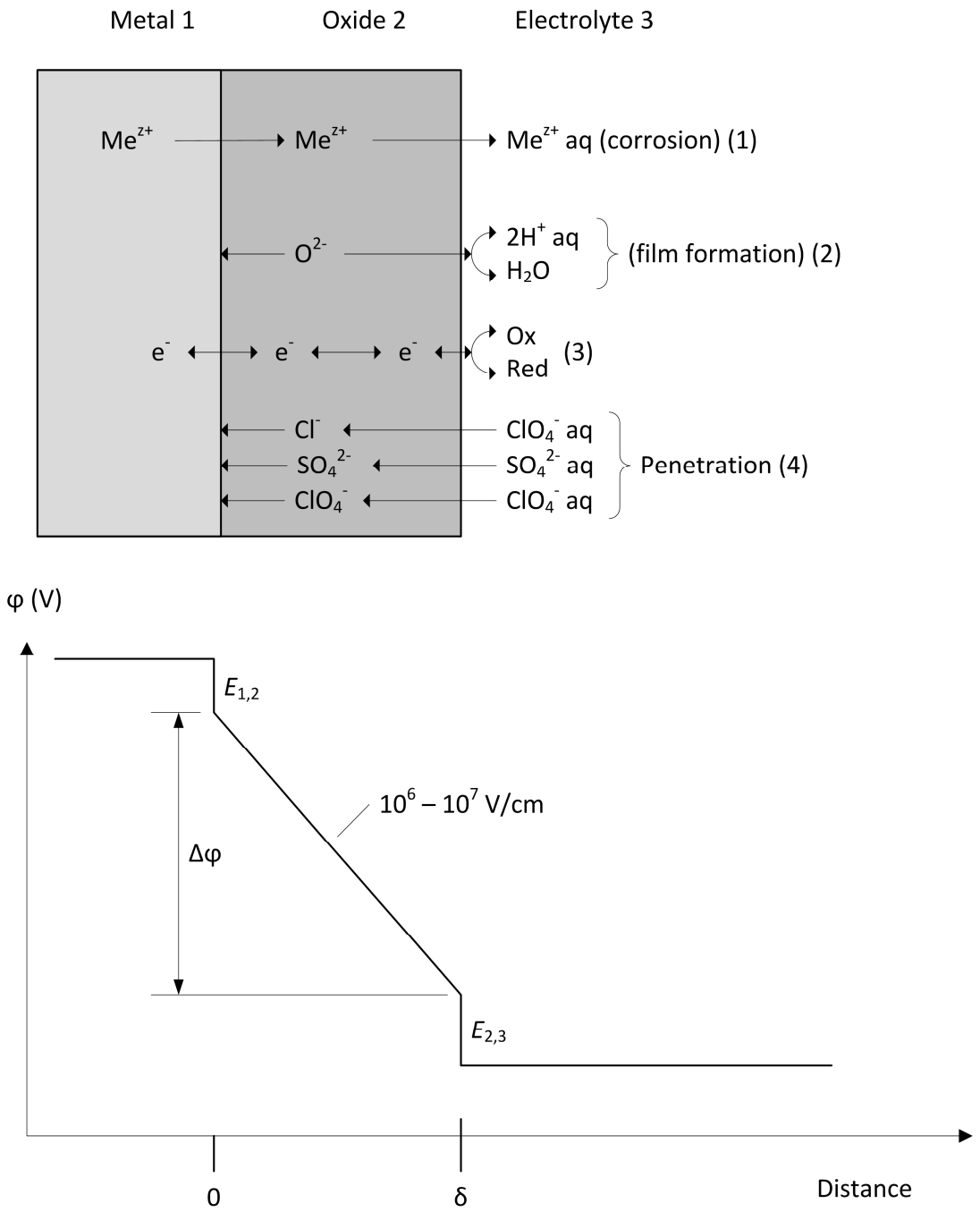

Fig. 1.1: Scheme of penetration mechanism and Galvani-potential drop at the metal/oxide/electrolyte interfaces.[11]

The penetration mechanism describes the transportation of anions through the thin oxide film of metals.[12] The driving force is the high electrical field of 10^6-10^7 V/cm caused by the Galvani-potential drop along the metal/oxide/electrolyte interface. In order to enable anion transportation a disordered passive film is required. McDonald and co-workers assumed a penetration model including the transportation of cation vacancies.[13,14] These migrate from the oxide surface to the metal/oxide interface while cations are transported in the other direction. Thereby anions, e.g.

chloride, get incorporated into the vacancies at the oxide/electrolyte interface and subsequently migrate through the passive film. If the penetration rate through the oxide is faster than through the metal, a local concentration results from the accumulation of vacancies at the metal/oxide interface. Even though the exact processes which occur at this moment at the metal/oxide interface are not fully understood, it is assumed that local enrichment of aggressive anions is the reason for the subsequent breakdown of passivity.

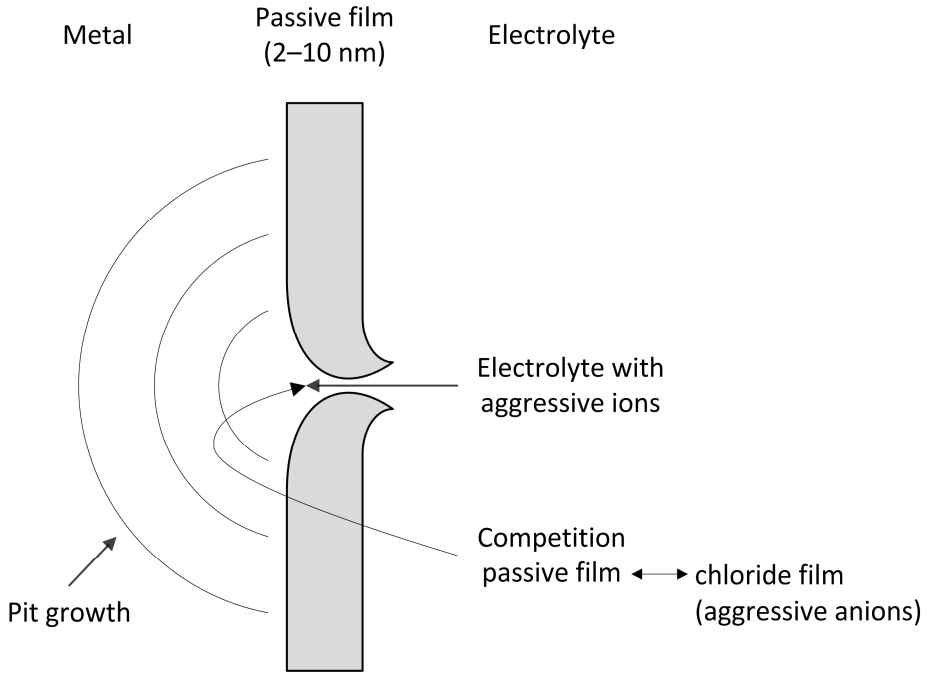

Fig. 1.2: Scheme of film-breaking-mechanism. Aggressive anions hinder repassivation at the microscopic subsurfaces in cracks which leads to pit growth.[11]

The film-breaking mechanism describes corrosion after breaking of the oxide films which enables the unhindered transport of aggressive ions through the passive film.[15-17] It is assumed that micro-cracks are easily formed in the passive film as a result of e.g. mechanical stress. Usually the released bare metal surface is immediately repassivated. In the presence of aggressive anions the repassivation is prevented which leads to local pit growth.

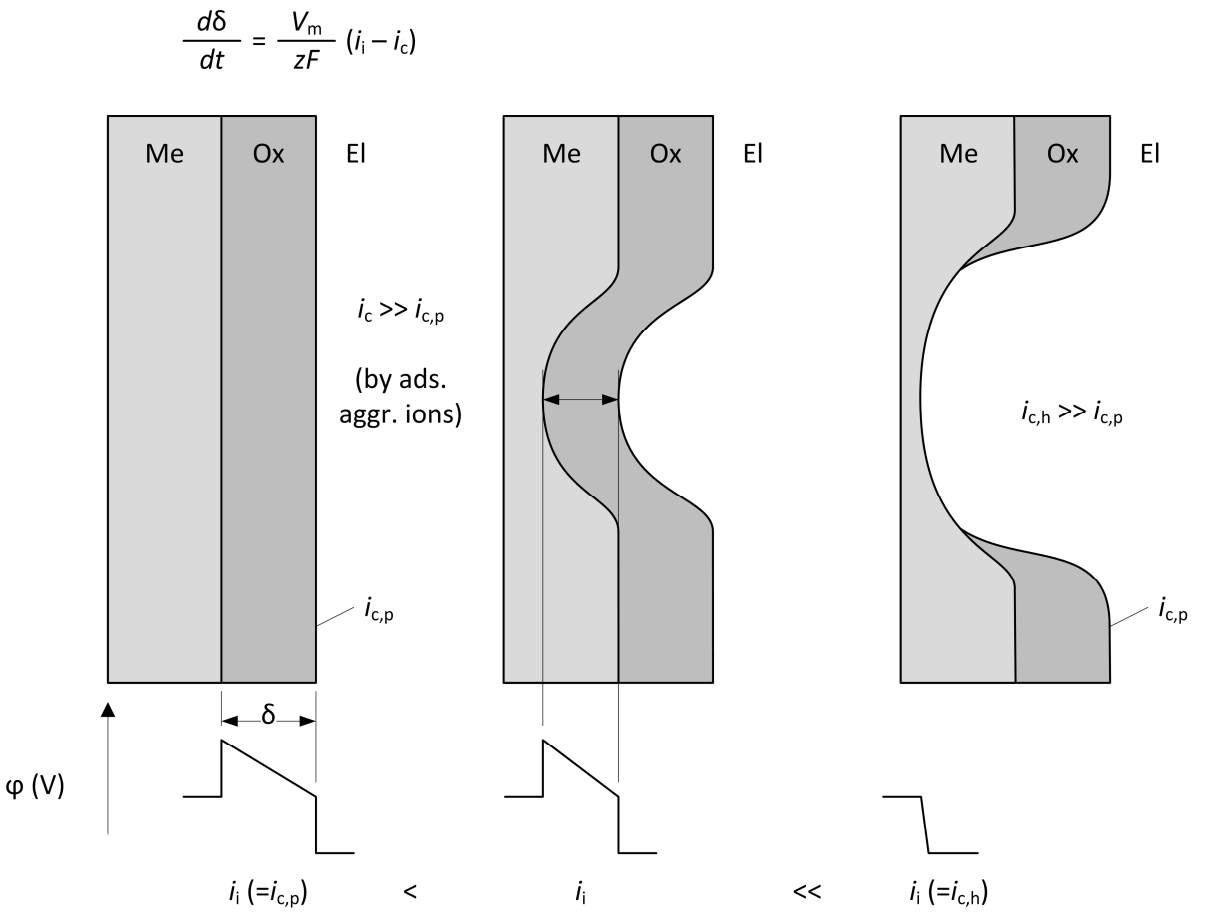

Fig.1.3: Scheme of adsorption mechanism with enhanced local metal dissolution due to the increased corrosion current density i_c. Complexation and release of metal cations by aggressive anions causes loss of passivity and an increase in the electrical field strength which lead to a much higher corrosive current density in the pit $i_{c,h}$ than on the passive film $i_{c,p}$.[11]

The adsorption mechanism is initiated by adsorption of corrosive anions on the passive film surfaces which catalytically enhances the transportation of metal cations from the covered metallic matrix through the passive film to the electrolyte.[18,19] In this way, the thickness of the passive film can be reduced up to a maximum point of total loss. Protecting this causes subsequently intensive local dissolution. The aggressive anions form surface complexes, which can subsequently be transferred much faster to the electrolyte than the uncomplexed metal cations.[20-23] This leads, especially in halide-containing electrolytes, to fast corrosive dissolution of the metal substrates.

1.1.3 Corrosion on iron

Iron is usually used in steel, since it is less stiff and chemically stable in its raw form. Carbon is incorporated into the iron lattice which leads to significantly improved material properties. Depending on the amount of matrix-embedded carbon, different types of steel can be distinguished. Non-alloyed steel contains less than 1.7 wt% carbon and mostly other elements (manganese, chromium, silicon), while low-alloyed steel contains less than 5 wt% carbon, and high-alloyed steel more than 5 wt%. Especially interesting with respect to the corrosion protection are chemically stable steels which contain more than 12 wt% chromium, and other alloying compounds like nickel, niob, manganese or molybdenum.

The most common sort of corrosion on steel is based on the reaction between iron and oxygen in alkaline, neutral or low-acidic electrolytes. This process leads to the formation of rust, which is a mixture of crystalline α-, β-, γ- and δ-FeOOH phases and the corresponding amorphous oxide hydrates, as well as phases containing Fe_3O_4 and α-, γ-Fe_2O_3. Furthermore, different forms of iron sulphates and chlorides might appear depending on the environmental conditions. However, the exact composition of rust depends on the chemical environment and this is described elsewhere.[24-28]

As previously described, iron forms passive layers on its surface which inhibit corrosion. The range of protection is thereby mainly dependent on the adhesion at the metal/oxide interface. A formation of a highly dense, protective film is thereby based on a proper equality in the volume ratio of the metal (Me) and metal oxide (MeO). In this case the grid constants for Fe is 2.86 Å, while it is 5.42 Å for Fe_2O_3, which is a volume coefficient Me/MeO of 2.16.[29] The different volumes hinder a proper adhesion at the metal/oxide interface which results in a porous film morphology that can hardly prevent the diffusion of ions through the film. This leads, furthermore, to non-inhibited progress of metal dissolution in a corrosive environment.

In order to avoid this problem, steel often gets coated with sacrificial anodes which are usually based on zinc, aluminium, magnesium and their alloys.[30-34] These sacrificial anodes have two protecting properties. One is based on their Galvani potential being lower than the protected metal, which only causes the dissolution of the sacrificial anode in a corrosive environment while the substrate remains unaffected. The other is the formation of non-porous passive films with a high adhesion to the protected metal, which hinders the migration of corrosive ions to the metal/sacrificial anode

interface. Thus, adequate long-term corrosion stability can also be achieved on iron-based constructions.

1.1.4 Corrosion on zinc

Zinc is widely used industrially for alloying, in batteries and for anodic protection of metals. For the latter application, zinc layers of even more than 100 µm thickness are deposited on metal surfaces either by hot dip or electro galvanizing.[35-37] These layers work subsequently as sacrificial anodes since their Nernst potential is relatively low in contrast to other metals. The anodic protection of steel is thereby the main application for these zinc layers.

Zinc is amphoteric owing to its solubility in both an acidic and an alkaline environment. Under moderate pH values zinc is relatively stable since it rapidly forms ZnO and amorphous $Zn(OH)_2$ as well as β-$Zn(OH)_2$ or ε- $Zn(OH)_2$ on its surface. These zinc modifications are slightly soluble in water and therefore protect the zinc matrix underneath. The anti-corrosion properties are caused by the semiconducting properties of zinc oxides and hydroxides.[38-42]

In atmosphere, the primary zinc hydroxide formation is followed by further, much slower oxidation steps causing the formation of $ZnCO_3$ and $Zn_5(OH)_6(CO_3)_2 \cdot H_2O$, which also reveal good stability in moderate pH.

1.1.5 Corrosion on aluminium

Aluminium alloys are widely used for lightweight construction due to their low density which is only 2,7 g/cm^3. Aluminium is either used in purities of up to 99.98%, or alloyed with other metals, of which Mg, Mn, Si and Cu are mostly used. The disadvantage of aluminium and aluminium alloys in contrast to steel is their much lower stability in an alkaline and marine environment.

In a moderate environment (pH 4–pH 9), aluminium surfaces are protected by a 1–2 nm thin passive layer of amorphous γ-Al_2O_3.[43-45] Under corrosive conditions aluminium further forms different phases of crystalline α-$Al(OH)_3$, β-, γ- $Al(OH)_3$, α-AlOOH, and γ-AlOOH, as well as amorphous $Al(OH)_3$. In a humid atmosphere, aluminium oxide also embeds a significant amount of water in its lattices by the formation of $Al_2O_3 \cdot H_2O$.

However, all modified aluminium oxides and hydroxides are soluble in acidic and alkaline media which results in a limited area of application of unprotected aluminium alloys. In contrast, the stability of aluminium in neutral aqueous solution without corrosive anions is extremely high. Its native oxide layer has a strong insulating ability and hence causes a nearly complete inhibition of cathodic and anodic processes. This fact is based on the very similar grit constants of Al (4.04 Å) and Al_2O_3 (5.15 Å), which cause the formation of a non-porous layer with a high degree of surface coverage and good adhesion at the metal/oxide interface. While the compact layer hinders ionic transportation processes from the electrolyte to the interface, the high band gap of the aluminium oxide impedes the electric conductivity between anode and cathode.

In order to enlarge the thickness of aluminium oxides and hence their protection properties, high anodic voltage fields are applied to the substrates. By doing this, 5–25 µm-thick Al_2O_3 layers are achievable which are subsequently treated in hot water or water vapour for the purpose of plugging pores with aluminium hydroxides.[46-48] These layers illustrate higher harnesses and better anti-corrosion properties.

1.1.6 Contact corrosion on iron, zinc and aluminium-based multi-metal constructions

If two dissimilar metals are in the same electrolyte, both form a galvanic cell with an open circuit potential which corresponds to the Galvani-potential difference between both half-cells. If there is a short-circuit, the metal with the lower Galvani potential will anodically dissolve while the one with the higher Galvani potential will dissolve much slower or even not at all. This process is known as contact corrosion and is intentionally used in some cases, e.g. zinc as a sacrificial anode on steel. Thereby the velocity of the corrosion process is often limited not for thermodynamic reasons but for kinetic ones.

Since zinc and aluminium forms under atmospheric conditions passive layers made of alkaline zinc carbonate and Al_2O_3 (see above) the dissolution of both metals in contact with steel is usually inhibited. However, the stability under contact corrosion is strongly dependent of the environmental conditions. The passivity of zinc and aluminium is little under marine conditions since the passive layers can be dissolved under impact of chloride. This leads to unhindered contact corrosion of both metals.

Since it is clear corrosive attacks cannot be totally avoided in practice, the constructions can be adjusted for the purpose of minimizing corrosive degradation. Therefore, the area of the compound

which reveals the most anodic galvani potential needs to be large in contrast to those with more cathodic Galvani potentials. This leads to a small dissolution/surface area ratio since the progress of anodic dissolution is limited by the progress of the cathodic counter-reaction which is indeed low for a cathode with a small surface area.

However, under conditions of atmospheric contact corrosion the long-term stability of multi-metal constructions made of zinc, steel and aluminium is achieved without difficulty. If the conditions become more corrosive, it is necessary to avoid contact of these metals by using insulating materials between the contact areas.

1.2 Electrochemical delamination at metal/polymer interfaces

Corrosion of reactive metallic substrates can be powerfully inhibited by coating with organic layers. These coatings are characterized by strong adhesion at the metal/coating interface which is either caused by physical or chemical bonding between the organic and inorganic matrices or even by a mixture of both. The corrosion inhibition properties are thereby mainly caused by the barrier properties of the organic layer against the diffusion of ions and the extension of the electric double layer at the metal/coating interface. The latter effect minimizes the Galvani-potential gradient at the interface which is the driving force for electron transfer reactions.[49]

If the formerly intact coating is damaged down to the metal surface, corrosion occurs due to the missing barrier between the substrate and its environment. If, furthermore, an aerated electrolyte appears at the defect area (something that usually occurs in a humid atmosphere), a galvanic element derives from the electrochemical reactions at the defect centre and its lateral extensions. The mechanisms which thereby describe the progress of the corrosion are distinguished by the part of the electrochemical reaction which occurs at the defect/coating transition: either the anodic metal dissolution (anodic undermining) or the cathodic counter reaction (cathodic delamination). Both sorts of delamination lead to de-adhering of the organic coating. Even though de-adhesion at the metal/coating interface can already be caused by ingress of water to the interface area, much stronger and faster de-adhering is effected by electrochemical corrosion processes.

Which form and velocity of delamination occurs at the metal/coating interfaces depends on several aspects. The most determining factors are the chemical and electronic nature of the metal oxide, the oxygen permeability and adhesion of the coating, the form of the defect, and the humidity of the atmosphere.[50-54]

1.2.1 Cathodic delamination

Cathodic delamination arises on zinc and iron in high atmospheric humidity.[53,54] Different electrochemical processes characterize the defect area, the delamination front and the intact polymer-coated metal/coating interface area. Since these areas are characterized by different electrochemical processes which influence the steady state of the diffuse electric double layer at the

interface, the areas can also be distinguished by their Galvani potentials. The progress of cathodic delamination and exposed Galvani-potential differences on iron substrates is illustrated in Figure 1.4.

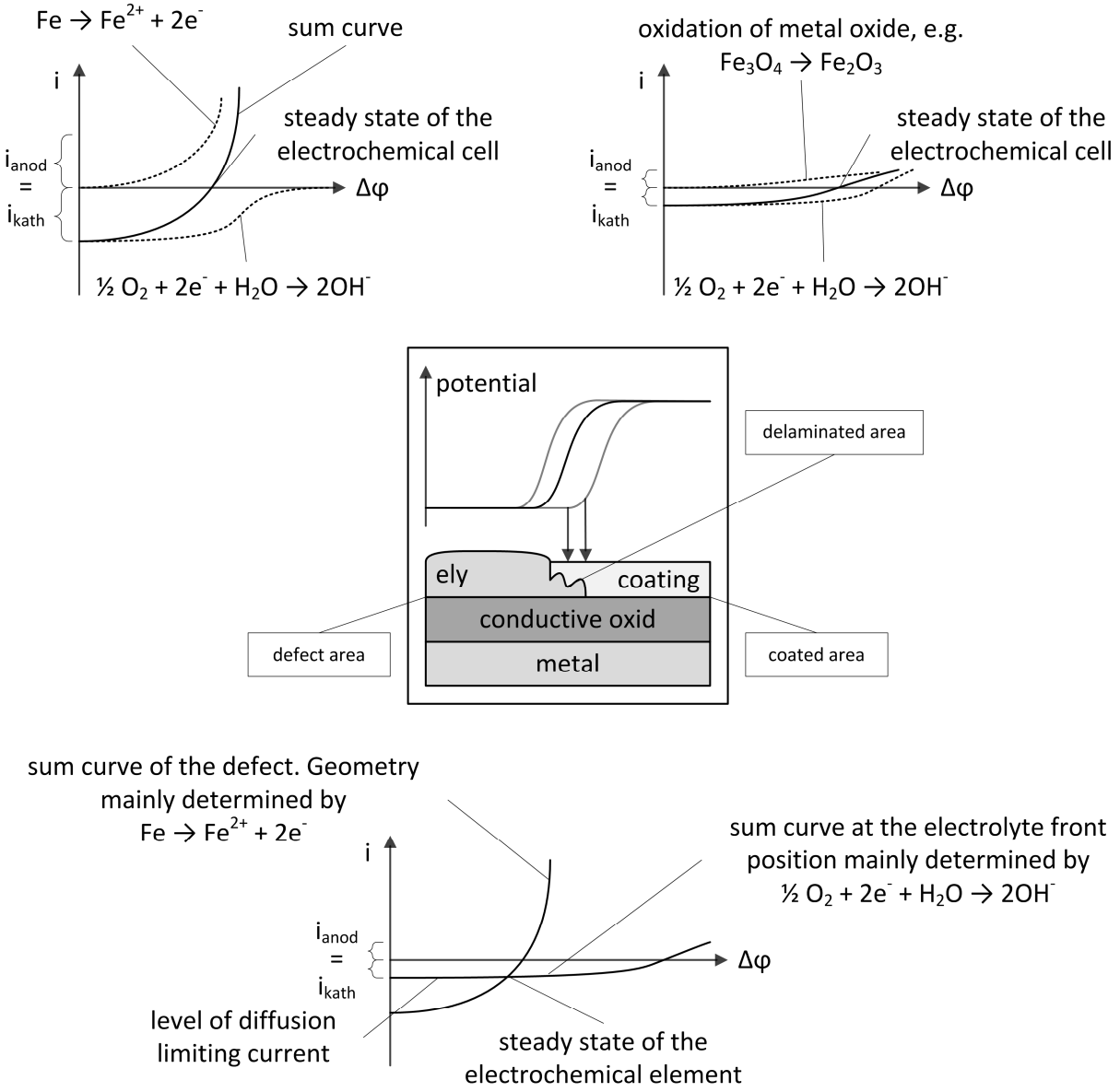

Fig. 1.4: Scheme of cathodic delamination on coated iron substrates with illustration of the current (i)/potential (Δφ) curves on selected spots along the iron/coating and iron/electrolyte interfaces.[56]

Thereby the anodic reaction is generally the dissolution of the substrate matrix

$$Fe \rightleftarrows Fe^{2+} + 2e^- \qquad (1.1)$$

while the cathodic counter reaction in aerated, neutral or alkaline electrolytes is the reduction of oxygen, which is the most common kind of corrosion.[53-55]

$$½O_2 + H_2O + e^- \rightleftarrows 2\,OH^- \quad (1.2)$$

The steady state (open circuit potential) of the electrochemical cell is described by relatively intensive anodic (i_{anod}) and cathodic currents (i_{kath}) as shown in Figure 1.4. The electrochemical process leads rapidly to the precipitation of corrosion products, which are primarily iron hydroxides and iron oxyhydroxides.

$$Fe^{2+} + 2OH^- \rightleftarrows Fe(OH)_2 \downarrow \quad (1.3)$$

$$Fe^{2+} + 3OH^- \rightleftarrows FeO(OH) \downarrow + H_2O + e^- \quad (1.4)$$

These corrosion products form less dense, semi-conducting layers which inhibit further corrosion processes at the intact metal/oxide/coating interfaces. The reason for this is the depletion of donor states of the iron oxide which causes a strong inhibition of electron transfer due to enhancement of the electric double layer. Hence the steady state is characterized by much smaller anodic and cathodic currents and a high anodic overpotential with respect to the formerly described steady state of the “active” metal/electrolyte interface. Thus the transition of the corroded surface and the non-corroded area underneath the organic coating is characterized by a distinct potential step which can be characterized by means of a Scanning Kelvin Probe (SKP) (see section 4.1.6.).[53-55]

During cathodic delamination the electrolytes penetrate the intact metal/coating interface adjacent to the defect area, where oxygen reduction occurs, as illustrated in Figure 1.5. Since the anodic process leads to metal dissolution in the defect area, the kinetic nature of the electrochemical reaction can be described by overlapping both i/Δϕ curves (see Fig. 1.4). In this way, the limiting factor is the oxygen diffusion current, which is in this case a little more inhibited than in the case for bare iron surfaces due to the additional barrier properties of the polymer matrix towards oxygen diffusion. This eventually leads to a slight anodic shift of the corrosion potential with respect to the potential in the defect area.

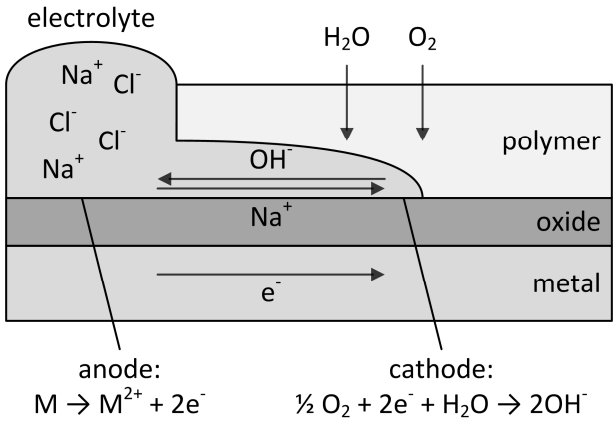

Fig. 1.5: Scheme of electrochemical and transportation processes during cathodic delamination.[56]

Since the local anode and local cathode are laterally separated, charge compensation needs to be assured by the transportation of matter. Therefore, electrons are conducted from anode to cathode through the semi-conducting oxide film while cations migrate from the electrolyte-filled defect to the delamination front, as illustrated in Figure 1.5. These cations are electrostatically attracted by the negatively charged hydroxide ions which derive from the oxygen reduction process.

The increased hydroxide concentration at the metal oxide/coating interface causes a comprehensible pH increase at the interface of up to pH 12 or in some cases (e.g. iron substrates) even higher. This leads to the passivation of the iron surface.[53-55] Thus no iron hydroxide precipitation occurs at the interface and the freshly formed hydroxide ions are transported towards the defect area for the purpose of charge compensation. It is noted that this interfacial ion transportation is the slowest process step and is thus rate-determining for the delamination process in which the size of the cations and therefore their diffusion coefficients are directly related to the delamination rates.[50,57,58]

However, the degradation of the coating matrices is not only caused by alkaline deterioration due to hydroxides, but mainly by radical oxygen species which occur as intermediates during the reduction process[55]

$$O_2 + e^- \rightleftarrows O_2^{-\cdot} \quad (1.5)$$

$$O_2^{-\cdot} + H^+ \rightleftarrows O_2H^{\cdot} \quad (1.6)$$

$$O_2H^{\cdot} + e^- \rightleftarrows O_2H^- \quad (1.7)$$

$$O_2H^- + H^+ \rightleftarrows H_2O_2 \quad (1.8)$$

$$H_2O_2 + e^- \rightleftarrows OH^{\cdot} + OH^- \quad (1.9)$$

$$OH^{\cdot} + e^- \rightleftarrows OH^{-\cdot} \quad (1.10)$$

The resulting matrix degradation can be assumed to proceed by the following reactions[59]

$$O_2^{\cdot-} + RH \rightleftarrows R^{\cdot} + O_2H^- \quad (1.11)$$

$$R^{\cdot} + O_2 \rightleftarrows ROO^{\cdot} \quad (1.12)$$

$$ROO^{\cdot} + RH \rightleftarrows ROOH + R^{\cdot} \quad (1.13)$$

This leads to de-adhesion of the polymeric matrix from the metallic substrate which eliminates the barrier against matter transportation and results therefore in an additional acceleration of the corrosion process. Finally, the cathodic delamination can destruct the entire interfacial adhesion which leads to macroscopic blister formation.

Beside studies of cathodic delamination on iron Fürbeth et al. investigated this process also on zinc substrates.[60-62] Even though the basic mechanism of cathodic delamination is equal for iron and zinc substrates an additional anodic process step was revealed due to the amphoteric properties of zinc oxide. Opponent to iron zinc is not stable in the high alkaline (pH 12) environment which characterises the conditions along the delamination frontier. Thereby zinc hydroxide forms zincate species in a dissolution/precipitation process[58]

$$Zn + OH^- \rightleftarrows ZnOH + e^- \quad (1.14)$$

$$ZnOH + 2OH^- \rightleftarrows Zn(OH)_3^- + e^- \quad (1.15)$$

$$Zn(OH)_3^- + OH^- \rightleftarrows Zn(OH)_4^{2-} \quad (1.16)$$

$$Zn(OH)_4^{2-} \rightleftarrows Zn(OH)_2 + 2OH^- \quad (1.17)$$

$$Zn + 2OH^- \rightleftarrows Zn(OH)_2 + 2e^- \quad (1.18)$$

$$Zn + 2OH^- \rightleftarrows ZnO + H_2O + 2e^- \quad (1.19)$$

This effect leads to a pH buffering in the interfacial region which is the reason for a lower alkaline environment at the interface with respect to the conditions on iron substrates. Furthermore, the ongoing delamination process on zinc leads to a significant deposition of corrosion product at the interface which is clearly visible. While steel surfaces remain shiny along the delamination frontier, white-coloured deposits cover the metal surfaces on zinc substrates.

1.2.2 Anodic undermining

Anodic undermining follows the same electrochemical mechanism as cathodic delamination but with reversed locations of the anode and cathode. Thus the anodic metal dissolution proceeds at the metal/coating interface while the oxygen reduction takes place at the defect area. In this way, the corrosion products are precipitated underneath the polymeric matrix which can, if they are voluminous, promote the delamination process by "lifting" the coating (see figure 1.6).

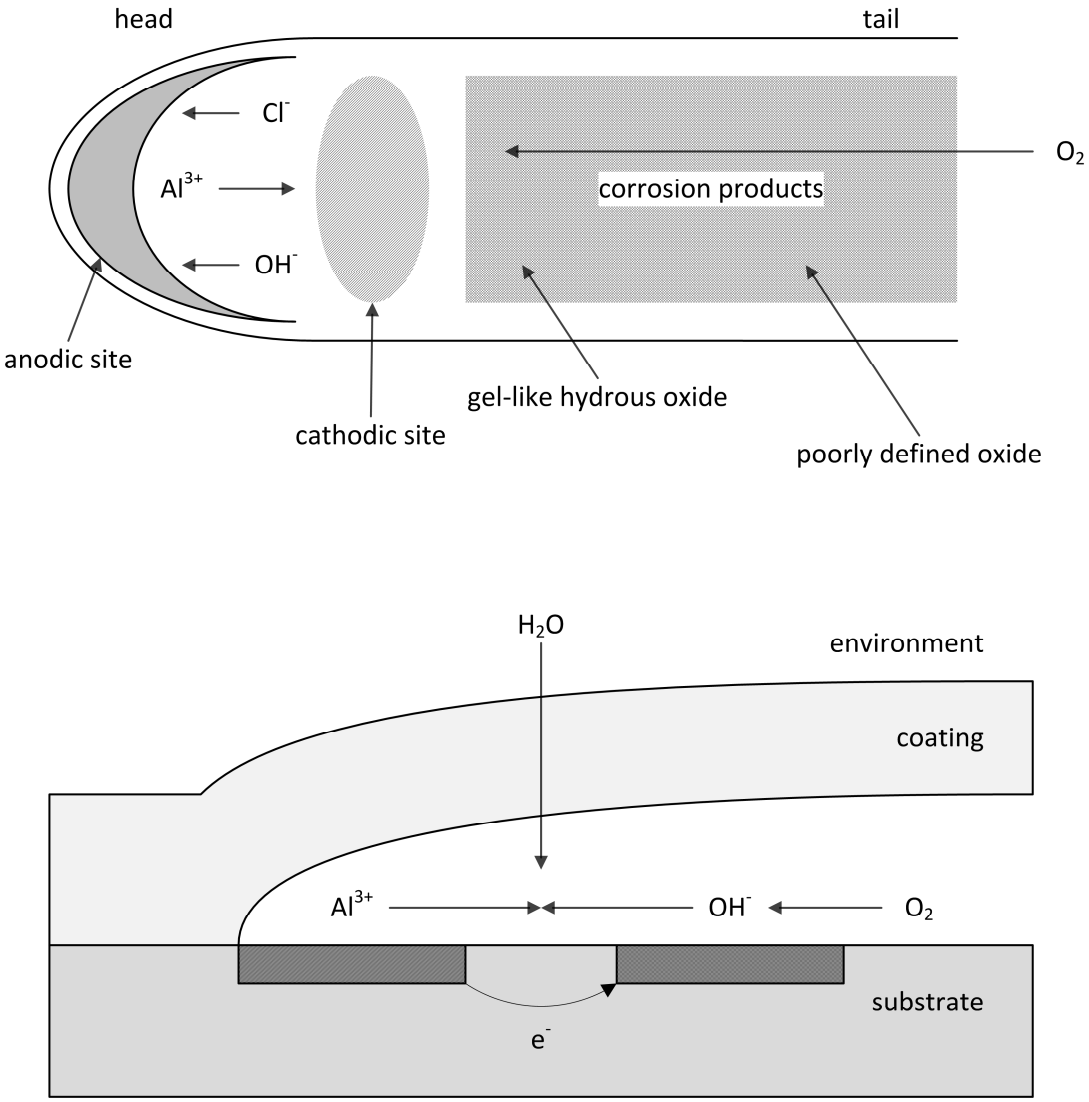

Fig.1.6: Scheme of anodic undermining on aluminium substrate during filiform corrosion.[63].

The most prominent alloy on which anodic delamination occurs is aluminium, where Al^{3+} and porous corrosion products are formed. The corrosive attack on aluminium is especially promoted by the presence of chloride which can easily dissolve the native, protective oxide film of Al_2O_3. In this case

HCl can be also formed along the delamination front caused by the transportation of matter which is formed as a result of charge compensation, as in the processes occurring in cathodic delamination.

The anodic undermining proceeds on aluminium mainly along irregularities on the surfaces (e.g. rolling or grinding marks) which lead to the formation of thread-like delamination tracks. This is called “filiform corrosion”.[64,65] Even though the mechanism of filiform corrosion is not completely understood, the generally accepted supposition is that the driving force is a differential aeration cell in the head of the corrosion filaments.[66]

However, since the cathodic delamination usually proceeds faster than anodic undermining, the inhibition of cathodic delamination is more intensively in the focus of anti-corrosion research.

1.3 Corrosion protection and adhesion promotion by thin-film systems on metallic substrates

1.3.1 Conversion layers

Conversion layers are very important for the pre-treatment of assemblies produced by the steel and automotive industries. They act as corrosion inhibitors and adhesion promoters between the native oxide-covered metal surfaces and subsequently applied organic resins. Chromate and zinc phosphate layers have been used for many decades since they were first discovered to be the best anti-corrosion primers specifically for application in the automotive industry.[67,68] Recently, the replacement of chromate-containing conversion coatings and tricathionic zinc phosphate conversion layers by new environmentally friendly systems has become the focus of research due to the carcinogenic properties of hexavalent chromium and the environmentally hazardous effects of nickel(II)-ions.

1.3.1.1 Mechanism of film formation on metal surfaces during immersion into conversion baths

Film formation in conversion baths is initiated by the acidic dissolution of the native oxide-covered metal surface which occurs simultaneously with the reduction of protons at the metal/electrolyte interface region. The pH gradient which results from the proton reduction in the Nernst Diffusion Layer causes the destabilization of the conversion bath compounds by exceeding their solubility product. These are subsequently precipitated on the metal surfaces and form the conversion layer. The film formation proceeds as long as the conversion process is not interrupted by the inhibition of the electron transfer reaction which leads to the collapse of the necessary pH gradient. This occurs when the surface is almost completely covered with the insulating conversion layer, enabling the reproducible formation of ultra-thin layers.

However, the film formation of aqueous conversion systems is strongly dependent on the bath contents and the process parameters since the adjusted pH and the concentrations in the solutions directly determine the film thickness and the degree of crosslinking inside the applied film.[69-71] Grundmeier and co-workers revealed furthermore the crucial effect of the surface pretreatment on the homogeneous film formation of ultra-thin, amorphous conversion layers on HDG[72] and identified the influence of metal ion-complexing organic additives on the surface coverage[73].

1.3.1.2 Alternative, environmentally friendly composition of conversion baths

The properties of non-toxic barrier coatings were studied with respect to the formation of ultra-thin films in order to combine high barrier properties with low material consumption and low costs. Chemical adsorption of organophosphonate[74-76] and organothiazole[77] monolayers, or amido-amine precursor,[78] was studied. Despite the auspicious results of those studies, the application of conversion layers cannot be avoided with respect to the corrosion inhibition and barrier properties of chromate and zinc phosphate layers.

1.3.1.2.1 Conversion layers based on organosilanes

Organosilane-based conversion layers are deposited from aqueous solutions containing partially hydrated functional or non-functional methoxy- or ethoxysilanes. Even though organosilanes with different functional groups like pyridine ($-NC_5H_5$), mercaptan (-SH), phenyl ($-C_6H_5$), methyl ($-CH_3$), cyano (-CN), and vinyl ($-CH=CH_2$) were revealed as proper adhesion promoters,[79,80] amino ($-NH_2$) functional organosilanes, like γ-APS, turned out to demonstrate superior corrosion resistance as well as excellent adhesion promotion.[81-83]

Thereby, the possibility of the formation of bonds between the organosilane and metallic surfaces, as well as the density of crosslinking, increases with the number of groups leaving. Thus application of organosilanes with three leaving groups is widely used for the purpose of adhesion promotion. The most prominent compounds are γ-aminopropyltrimethoxysilane (γ-APS) and 3-(glycidyloxypropyl)trimethoxysilane (GLYMO) as illustrated in Figure 1.7.

However, all commonly used organosilanes have the general formula $F\text{-}Si(R)_n(R')_{3-n}$, in which R is the leaving groups and F an alkyl chain with a functional head group. If in contact with water, the leaving groups are substituted by hydroxyl groups which form silanol functions. These initiate the bonding to hydroxyl-terminated surfaces and subsequently crosslinking of the deposited films by formation of a siloxane network. The alkyl chain F defines the hydrophobicity/hydrophilicity of the resulting film whereas its functional head group determines the bonding to the next organic coating.

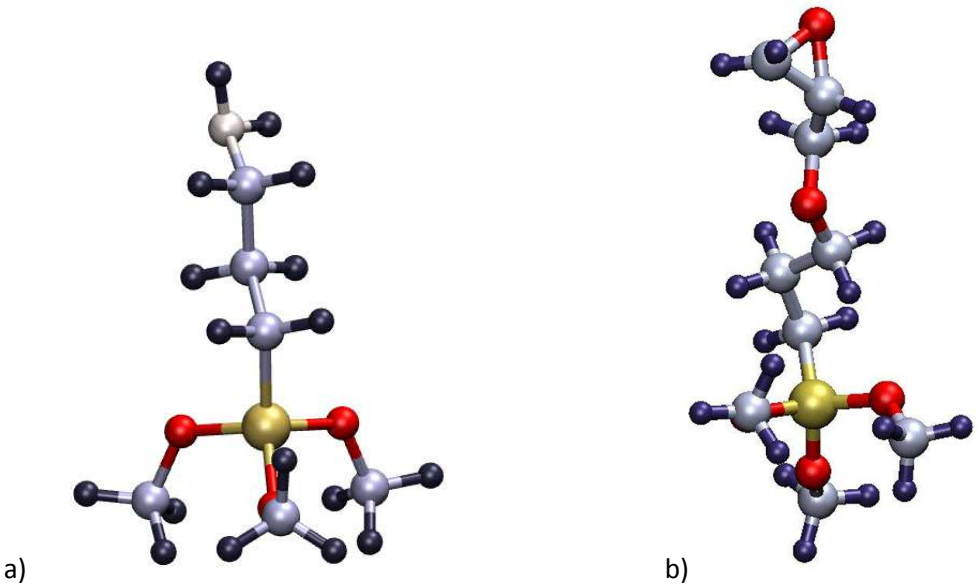

a) b)

Fig. 1.7: a) γ-aminopropyltrimethoxysilane and b) 3-(glycidyloxypropyl)trimethoxysilane.[84]

Ultra-thin organosilane-based conversion films on metal surfaces are applied by immersion of substrates into the aqueous solutions. After finishing the coating process, which does not usually take more than a few minutes, the converted metal substrates are annealed to ensure further crosslinking by condensation of the silanol functions. Even though the exact mechanism of adhesion between the organosilane matrix and the metal surface is still under discussion,[85] the widely accepted mechanism ends in the formation of covalent bonds between the silanol function of the organosilane and the hydroxide-covered metal surfaces by the following mechanism:[85-89]

1. Hydration of the organosilane

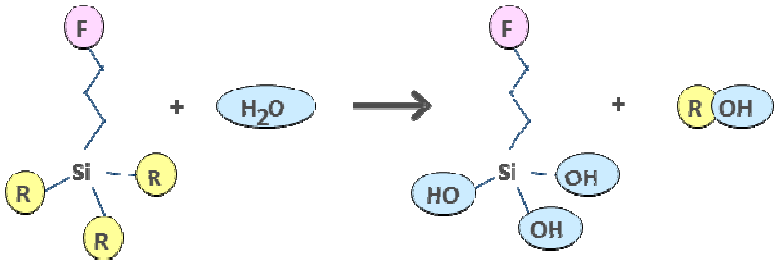

2. Simultaneous hydrogen bond between the silanol and the surface hydroxyls and among the silanols

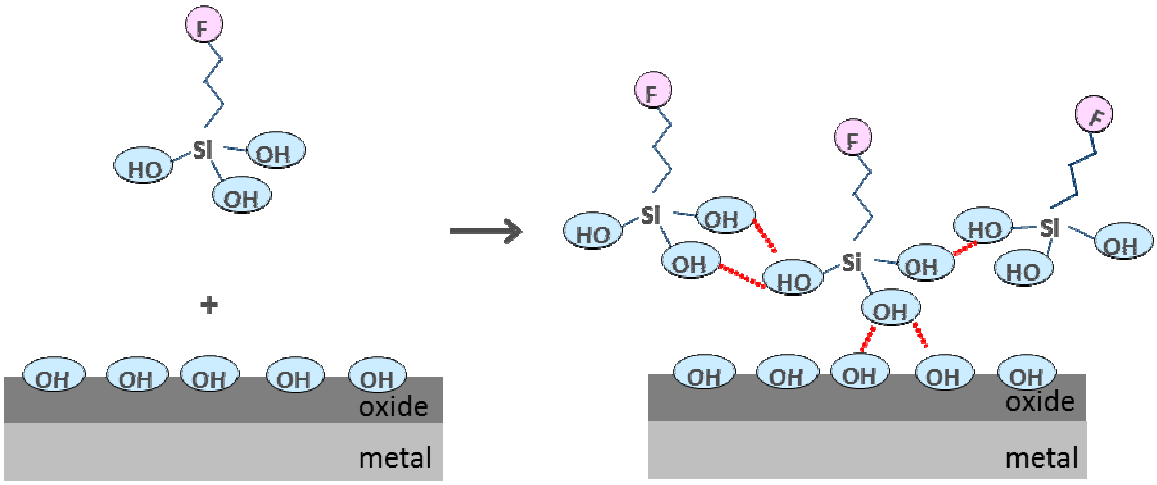

3. Condensation of the hydrogen-bonded structure to silicon-oxygen-metal and silicon-oxygen-silicon bondings

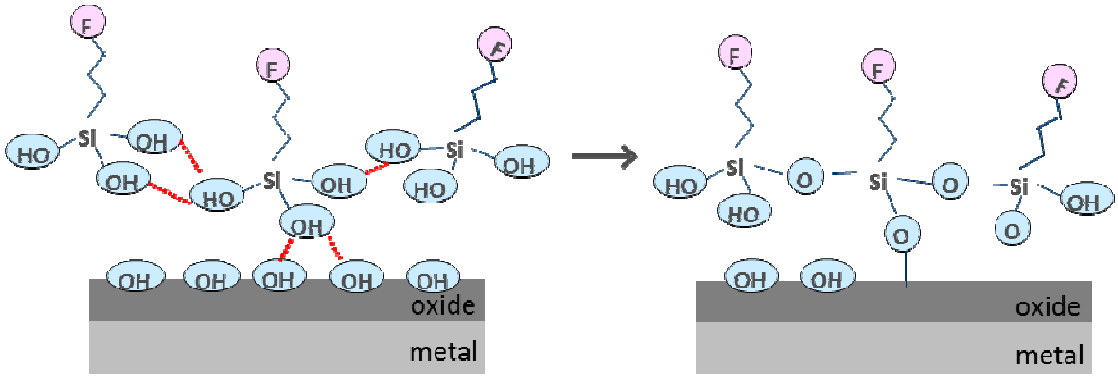

1.3.1.2.2 Conversion layers based on transition metals and lanthanides

Different transition metal and lanthanide salts have been investigated for their application as corrosion inhibitors in conversion layers. Transition metals that were studied were those which demonstrate similar physical and chemical properties to chromate, like molybdenum, vanadium, tungsten or manganese. From these, MnO_4^{2-}-, MoO_4^{2-}-, and WO_4^{2-}- containing layers illustrated promising corrosion protection on aluminium alloys in which molybdate revealed the best corrosion inhibition properties.[90-93] This means that similar corrosion protection to that caused by chromate layers was found to exist.[94-96]

For molybdenum-based conversion layers deposited on zinc substrates from aqueous, phosphoric acidic baths, Magalhaes et al. illustrated that the corrosion inhibition mechanism is also analogous to that discovered for chromate layers.[96] By these means the main reason for the corrosion protection was considered to be the effective suppression of the anodic oxidation.[97,98] Almeida et al. studied the morphology and chemical composition of molybdate-based layers and revealed that they are thick, brittle and heterogeneous layers which contain both Mo(IV) and Mo(VI)[95].

Even though molybdenum-based conversion systems revealed the best protective properties from the investigated transition metals, disadvantages were also found. Scerry et al. showed that molybdate is inferior to chromates in inhibition of the cathodic reactions on aluminum and that it is ineffective on copper-bearing alloys.[99]

Additionally, lanthanide salts have been investigated as corrosion inhibitors in conversion layers since they are known to form insoluble hydroxides.[100] For the purpose of incorporation of lanthanides into the film matrices, highly oxidized salts several orders of magnitude more soluble than their corresponding hydroxides were added to the conversion baths and subsequently co-deposited on the substrates. This is based on their reduction in corrosive environments, which subsequently leads to the formation of hydroxides in the alkaline environment, which in turn occurs simultaneously due to oxygen reduction. Based on their low solubility, these hydroxides precipitate as protective layers on the metal surfaces; thereby the formed layer inhibits the cathodic current and thus the overall corrosion rate. Moreover, lanthanides show low toxicity[101] and are also economically beneficial[102] since some of them are relatively abundant in nature.[103] For instance, cerium is as plentiful as copper.[104]

By application of different rare earth metals, well-adhering lanthanum oxide films were obtained by the oxidation process.[105-109] These layers illustrate moreover good protection against high temperature and aqueous corrosion, in which cerium showed the most promising results. Lu and Ives revealed that incorporation of cerium into AISI 316 stainless steel decreases the corrosion rate in sodium chloride solution by two orders of magnitude.[110] They assumed that the formation of CeO_2 films on the metal surface inhibits both anodic and cathodic reactions. Other lanthanides were also investigated on different metals, like zinc,[111-113] bronze,[114,115] nickel,[116] mild steel,[117,118] and stainless steel.[119-123]

However, the mechanism of the corrosion inhibition as a function of the bath concentrations was first studied on cerium trichloride-based corrosion protection layers by Hinton, Arnott and

Ryan.[124-126] They showed that the resistance against pitting corrosion on AA7075 (Al-Zn) increased slowly from 0 ppm to 100 ppm $CeCl_3$ concentration and strongly from 100 ppm up to 1000 ppm. From 1000 ppm up to 10000 ppm a steady state was detected. According uniform corrosion an optimum resistance was already able to be achieved by 100 ppm $CeCl_3$, while higher concentration only produced stabilization in the corrosion rate.

Other lanthanides were also investigated by the same authors. They studied the corrosion inhibition properties of YCl_3, $LaCl_3$ and $PrCl_3$ and showed that the dependency of barrier properties on lanthanide concentrations is similar to that detected on layers deposited from $CeCl_3$ solutions.[112,125-127] It was furthermore shown that the best degree of inhibition was derived from $CeCl_3$ which, in its optimum concentration, was as effective as chromate layers. In contrast, the protective properties of cerium layers deposited from $Ce(NO_3)_3$ and $Ce_2(SO_4)_3$ solutions revealed inferior results to cerium trichloride since the inhibitor effect of cerium was in these layers suppressed by the influence of the oxidizing nitrate and sulphate anions.[128]

Studies of the corrosion inhibition mechanism of lanthanide salts illustrated its cathodic nature.[129] Similar to the layers containing transition metals, lanthanide hydroxides, which are formed during oxygen reduction, are precipitated on the surface and suppress further cathodic reactions.

Nevertheless, the disadvantage of lanthanide salts is the slow film formation from those solutions. Hinton et al. obtained optimum protective conversion layers on AA7075 after 90 h immersion in a 0.1% $CeCl_3$ solution, with appreciable properties showing at 20h.[124,130,131] In order to accelerate the film formation process, Wilson and Hinton added oxidizing agents and organic additives to an aqueous solution of $CeCl_3$ but received a poor corrosion resistance.[132] Mansfeld et al. developed a cerium–molybdenum-based conversion system which was deposited by a two-step process.[133,134] The obtained conversion layer combined the corrosion inhibition properties of both elements and remained stable in 0.5M NaCl for 30 days. Xingwen et al. coated copper-containing Al alloys (A2014) by a two-step conversion process which was conducted in a borate solution of cerium nitrate and carbonate in the presence of an oxidant (H_2O_2).[135] The resulting layer adhered well to the alloy surface and inhibited both anodic and cathodic currents.

Recently titanium- and zirconium-based conversion layers have revealed promising corrosion protection properties. Aqueous baths containing hexafluoro complexes of titanium and zirconium were used, which proved to be the best composition on multi-metal constructions with respect to

the corrosion inhibition and the dissolution of native oxide films which occasionally hinders adequate conversion processes, e.g. on aluminium alloys.[136,137]

1.3.2 Self-assembled monolayers

Ultra-thin layers of self-assembling monolayers (SAMs) are also used as adhesion promoters[138-140] and corrosion inhibition layers[141-144] on metallic surfaces. With their use in this way, mono- or bifunctional long-alkaline chained molecules are adsorbed at the metal/solution interface during immersion of metallic substrates into SAM solutions. For the purpose of self-assembling, one of the functional groups needs to show a strong affinity to the metal matrix. The process of SAM formation is then initiated by the substitution of solvent molecules which are physically weakly bonded to the metal surfaces by SAM molecules, as illustrated in Figure 1.8. As a result, island-like formations of SAMs are initially achieved.

Even though the decrease of entropy by this molecule aggregation is inappropriate for thermodynamical reasons, two factors determine the proceeding SAM molecule adsorption and overcome the loss of entropy which finally ends in total surface coverage of highly organized SAMs. One of the factors is the bonding of the SAM head groups to the surface which is often based on the formation of covalent bonding between the head group and the hydroxyl-terminated surfaces by acid–base interaction as revealed on aluminum by Allara et. al.[145] and Maege et. al.[146] The other factor is based on the stabilization of the highly organized SAMs which is dominated by attractive van der Waals forces between the SAM tails.[145] Thus the length of the alkyl chains is significant for the stability of the adsorbed SAM molecules as illustrated by Maxisch et. al. who showed that the total VdW forces of short alkyl chains are too insignificant to stabilize SAMs against substitution by water in a humid environment.[147]

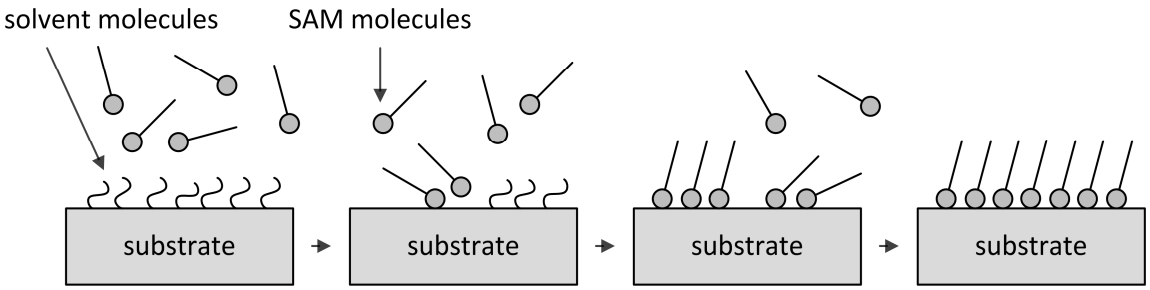

Fig. 1.8: Scheme of SAM film formation on metal surfaces.[148]

Based on these energetic considerations, it becomes clear that both the surface chemistry and the functionality of the SAM molecules are eminent parameters with respect to the formation process. While the adsorption of thiol-functional molecules like octadecylthiol (ODT) produced favourable results on Au surfaces,[149-153] their self-assembling on commonly used metals like aluminium and steel was poor. It turned out that carboxylic acid and phosphoric acid functional alkyl chains are more adequate for SAM formation on aluminium[138,154-158] while the adsorption on steel and TiO_2 surfaces perform better with usage of phosphonic acid.[159-165]

However, in order to achieve a proper SAM formation, other process parameters, like the pretreatment conditions, also need to be considered. As shown by Grundmeier and co-workers, plasma pretreatment leads to an accelerated SAM adsorption kinetic of octadecylphosphonic acid (ODPA) on aluminium.[166]

1.3.3 Biomimetic adhesion promoters

A further approach in the context of environmentally harmless chemistry, otherwise known as “green chemistry”, is the assimilation of biological mechanisms into artificial applications. Even though studies of bio-inspired adhesion promotion and corrosion protection are in the early stages, they seem to be positive in terms of efficiency. In these studies, underwater creatures as described below were the focus of the research, because although synthetic adhesives show high cohesive strength, this strength weakens in water or a wet environment.[167-169]

The caddisfly larva spends the majority of its life in the larval stage in freshwater lakes or rivers. There, it uses sticky underwater silk to explore its habitat, which is constructed of rocks, leaves or sticks adhered together.[170] Moreover, it uses underwater silk webs to capture prey from water channeled through these webs. Different mussel species also use bioadhesives to reduce the mechanical mismatch between hard rock and their soft invertebrate bodies.[171] Arcon barnacles[172] glue calcareous plates to rocks or boat bottoms while sandcastle worms form their habitats out of tubes which consist of sand and shell fragments adhered by a proteinaceous glue.[173] Conus snails[174] use bioadhesives to anchor egg capsules onto solid surfaces. Flagellated zoospores of brown algae (kelp) glue themselves to selected surfaces to enable varied placement of their habitants[175] while starfish escape on temporary adhesive footprints.[176] Areas where no macroscopic species are living are inhabited by microbes which attach themselves with biomacromolecular biofilms.[177]

Due to these natural examples, usage of biomimetic compounds as adhesives on organic or inorganic surfaces came into the focus of recent research. Even though bioadhesives under environmental conditions are used to bond to mineral surfaces, proper adhesion to synthetic surfaces which do not exist in nature was also observed. It was revealed that underwater organisms can adhere to polytetrafluoroethylene, paraffin wax,[178,179] SAMs with low surface energies,[180-181] and polydimethyl siloxanes.[182]

However, it is important to keep in mind that the above-mentioned underwater/wet environment bioadhesives are not necessarily in an inferior position to purely synthetic adhesives with respect to their mechanical properties. Wilker and co-workers showed that the tensile strength of mussel adhesive plaques (288 ± 110kPa on Al) is about 1/3 of the strength of Elmer´s White Glue, which is based on polyvinyl alcohol, and about 1/30 of that of household superglue, which is based on polyethylcyanoacrylate.[183]

In order to find the chemical compounds which are responsible for these outstanding bioadhesion properties, the mussel species Mytilus was studied with a focus on its byssus and the chemical composition at the surface/mussel plaque interface (see fig. 1.9). At least 12 proteins in the byssus were discovered.[201] Among different amino acids distributed in these proteins the catecholic amino acid 3,4-dihydroxyphenyl-L-alanine (L-DOPA) was proven to be contained in all proteins. Moreover, the dominating proteins localized at the surface/mussel plaque interface were revealed to be the Mytilus foot protein-3 (mfp-3) and the Mytilus foot protein-5 (mfp-5).[184,185] In contrast to all other proteins both have the lowest mass and the highest content of DOPA [201].[186-188] The mussel adhesive plaque protein mfp-3 contains 20 mol% DOPA and 19 mol% 4-hydroxylated arginine while mfp-5 contains 25 mol% DOPA and 10 mol% phosphorylated serine (pSer).[189] Studies of the sandcastle worm revealed around 2–3 mol% DOPA and 30 mol% pSer in its glue,[190-192] while the underwater silk of the caddisfly is made of 10 mol% of pSer.[193]

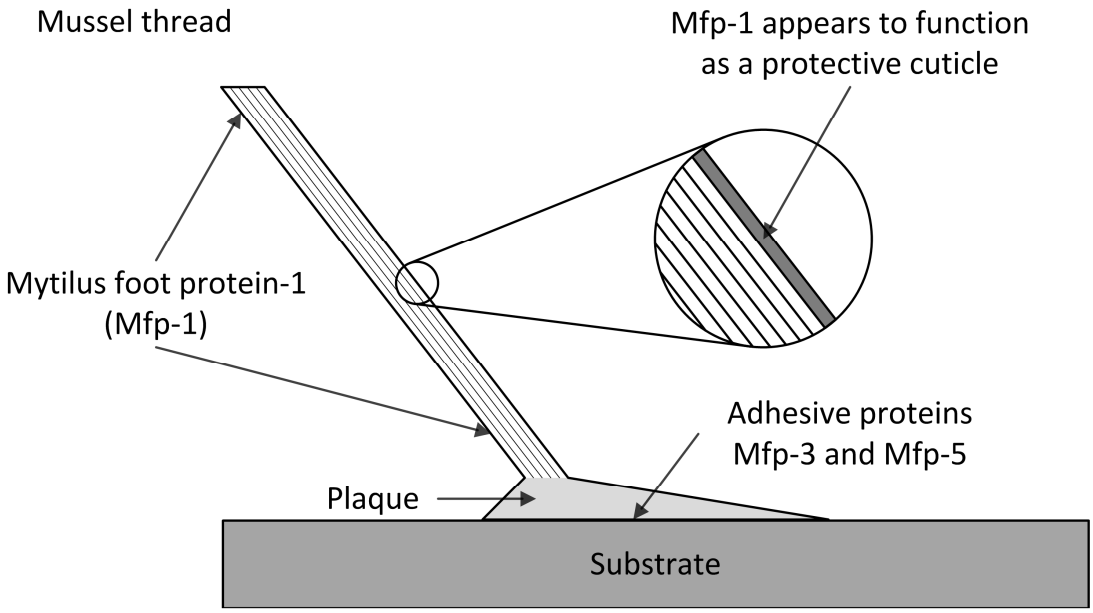

Fig. 1.9: Scheme of a byssal thread attached to a substrate. The plaque contains primarily the proteins mfp-3 (20 mol% DOPA) and mfp-5 (25 mol% DOPA) while the outer coating of the mussel thread is made of mfp-1, which has up to 15 mol% DOPA [201].

However, among these different amino acid functionalities the catechol sidechain of L-DOPA became the most prominent biomimetic adhesion promoter[194-198] since it could be shown that both natural and synthetic DOPA show strong adhesion properties.[187,199-201] Further studies into the mechanism of adhesion revealed that catechols adsorb on metal surfaces by ligand exchange of coordinated water and hydroxyl ions during formation of bidentate inner sphere complexes,[202,203] and are therefore ideal for underwater adhesion.[204] Moreover, it was shown that the ortho-dihydroxy configuration of catechol is necessary for intensive adhesion since studies of meta- and para-dihydroxybenzenes did not reveal strong adsorption, nor did L-tyrosine or L-Phenylanaline.[205,206]

The adhesion mechanism of phosphoserine (pSer) is supposed to be one of the phosphonates which also form bidentate inner-sphere complexes on oxyhydroxide-terminated metal surfaces over a broad pH range,[207-209] but is nevertheless not designated as a biomimetic adhesion promoter since the strong, water-resistant adsorption of phosphates and phosphonates is already fundamentally known in many applications, like water-bone latex paints,[210] dental materials,[211,212] corrosion inhibitors[67,68] or SAMs[150-165].

However, several biomimetic adhesives have been developed based on the catecholic sidechain of DOPA. Water-resistant adhesives were formed by incorporation of DOPA into synthetic polymers which were subsequently jellied by DOPA oxidation using either oxidation agents like $NaIO_4$ or H_2O_2, or stimuli by temperature, pH, ion concentration or UV, as well as visible light.[213-219]

Unfortunately, all these techniques had a disadvantage: it is believed that the unoxidized form of DOPA possesses stronger adhesion properties than the oxidized one, especially with respect to adhesion on metallic surfaces.[220]

Other applications mimicking DOPA were the formation of synthetic non-fouling surfaces,[191,194,221-224] the creation of PEG hydrogels for the purpose of tissue engineering,[225,226] and the formation of sticky layers on structured surfaces in order to create a wet/dry, mussel/gecko adhesive[227].

Moreover, bioadhesives based on the underwater glue of the sandcastle worm were developed as polyelectrolytes with analog functional sidechains containing either phosphonates, amines or cathechols.[228,229] These synthetic adhesives formed complex coacervates which mimicked the entire range of properties of the natural glue proteins if composited in the same sidechain molar ratio and in similar proportions, including divalent cations. Thus adequate underwater delivery, wet interfacial adhesion and triggered solidification could be achieved.

Since these adhesive coacervates are self-organized in water, stable after complete crosslinking, and can be used as containers for small molecules, they are ideal underwater adhesives with great potential in medicine. Through application to skull bones it was revealed that the coacervates do not impede new bone growth, are non-toxic, and do not induce persistent inflammation.[230] Recently the bond strengths of synthetic coacervates were increased to several times the estimated value for natural adhesives by incorporation of additional phases into the adhesive matrix.[231]

1.4 Objectives

The aim of this work was to achieve the combination of the corrosion inhibition properties of adsorbate layers based on organosilanes and conversion layers based on zirconium dioxide. Since the barrier properties and corrosion resistance of thin zirconium[232] and zirconium/organosilane[233] based conversion/adsorption systems has already been partly investigated, we focus on the examination of the inhibition of oxidative de-adhesion of conversion/adsorbate layers at the metal/oxide/coating interfaces based on an ultra-thin bilayer system of zirconium oxide and organosilane.

Moreover, a hybrid zirconia/organosilane-based conversion system was investigated with the purpose of revealing the corrosion inhibition properties dependent on application on multi-metal constructions. In this investigation, the chemical composition, the corresponding layer morphologies and its barrier properties were studied and compared to the previously investigated bilayer system.

Furthermore, the influence of physical bath parameters was investigated and modified in order to reveal potentials of enhancement of surface coverage and barrier properties. To achieve this, fluid dynamics and bath temperatures were varied during the film formation process.

Additionally, post-treatments with self-assembled molecules were investigated for the same results and finally studied with respect to the anti-corrosion performance of unmodified conversion systems and tri-cationic zinc phosphatization layers. Moreover, corrosion inhibitors were incorporated into the film matrices in order to enhance the barrier and leaching abilities of the conversion systems under conditions of oxygen reduction.

2 Fundamentals of Applied Techniques

2.1 Spectroscopy

2.1.1 Fourier-Transformed Infrared Reflection–Absorption Spectroscopy (FT-IRRAS)

FT-IRRAS is a type of infrared spectroscopy which analyzes the chemical state and chemical composition of thin adhesive layers on metallic substrates by reflection at the metal/coating interface.[234] It uses electromagnetic rays with wavelengths in the near (NIR) and middle (MIR) infrared region which excite fundamental frequency (MIR) or overtones (NIR). The energy necessary to excite a specific mode of vibration depends on the mass of the molecules involved and the strength of the chemical bonding and is therefore unique for a chemical function. The potential curve of the oscillations of the quantum vibration states can be described by an inharmonic quantum mechanical oscillator.[235]

Absorption of the IR radiation occurs if its wavelength corresponds exactly with the energy necessary to activate a vibration which causes a change in the dipole momentum of the corresponding chemical bond. In this case the electric field E of the IR ray interacts with the electric dipole μ of the functional group. The intensity I_{IR} of the detected vibration is proportional to the square of the change of the dipole moment[236]

$$I_{IR} \propto \left| \frac{\delta \vec{\mu}}{\delta Q_k} \vec{E} \right|^2 \tag{2.1}$$

(with I_{IR} as the intensity of the IR vibration band, $\vec{E}$ as the electric fieldvector, $\vec{\mu}$ as the integral of the dipole moment and Q_k as the normal coordinate (k=x,y,z)).

Hence not all vibrations are IR-active. If a vibration in a functional group is symmetrical to the center of symmetry of the molecule, no change of the dipole momentum results and therefore no IR band can be detected and the vibration is therefore IR-inactive.

Since FT-IRRAS is conducted by reflection on metallic surfaces the intensity of the signal moreover depends on the plane of incidence on the surface. If the vector of the E-field is perpendicular to the plane of incidence it inducts an additional E-field on the metallic surface which has the same orientation as the incident beam, which results in the enhancement of the detected signal. If the plane of incidence is parallel to the surface, an additional electric field is inducted on the metal surface which is directed opposite to the primary E-field and results in the extinction of the signal. Thus not only can information of the chemical composition be obtained by FT-IRRAS but also information about the orientation of the molecules adsorbed on the surface.[237]

In order to increase the signal of even ultra-thin films deposited on the metal surfaces, FT-IRRAS uses grazing angles of incidence. The reason for this is that by a low angle of incidence the path of transmission through the films under investigation is much larger than by perpendicular incidence and thereby also the achieved density interaction between the film matrix and the IR ray.[238] In contrast, the total intensity of the IR signal is also decreased by longer transmission through the layers. Thus it is necessary to find an optimal ratio between the total IR signal and the recorded information density which is achieved by using an angle of incidence of around 80°.

2.1.2 X-Ray Photoelectron Spectroscopy (XPS)

X-Ray Photoelectron Spectroscopy is used for the quantitative analysis of the element distribution and the atomic oxidation states of matter.[239] The information depth of the technique depends on the angle of incidence of the radiation between 5 and 30 A which offers the possibility of receiving information on the chemical bonding states near to the sample surface. Hence the collected XPS spectra contain element- and bonding-specific information for all elements except hydrogen and helium with a surface sensitivity between 1% and 0.1%.[240]

The basis of analysis of the outer atom layers is the photoelectric effect in which photoelectrons are emitted from matter after the adsorption of electromagnetic radiation as illustrated in Figure 2.1. Inner electrons are thereby liberated and subsequently replaced by electrons from outer core shells. Free photoelectrons are emitted, as is electromagnetic radiation, which energy directly corresponds to the difference of the energy states of both the involved inner and outer core shells.

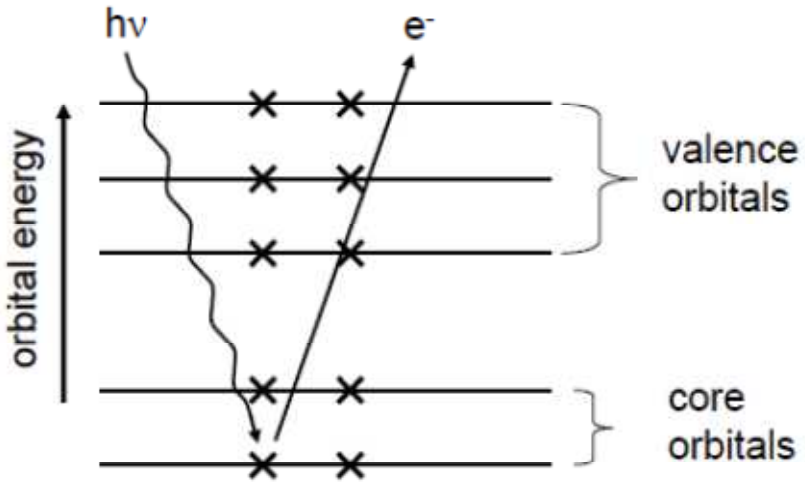

Fig. 2.1: Scheme of photoelectric effect during XPS.[241]

In order to release photoelectrons, the energy of the absorbed x-ray radiation hν (h as the Planck constant and ν as the frequency) needs to be higher than the electron work function ϕ. The kinetic energy E_{kin} of the emitted electrons is characteristic for the core shell and the bonding state of the atom and can be quantified as:[242,243]

$$E_{kin} = h\nu - \mathrm{E_{binding(sample)}} - \Phi_{\mathrm{sample}} \quad (2.2)$$

(with $E_{binding(sample)}$ as the binding energy of the emitted electron and ϕ_{sample} as the work function of the sample).

In order to receive element- and bonding-specific information it is only useful to detect core electrons since the energy level of valence electrons overlaps in metal matrices and builds electron bands which then lose their specific energy state.

The detector of the spectrometer is conductive and is connected to the analyzed sample which causes equalization of its Fermi levels. From this results a dependence on the kinetic energy and the electron work function of the analyzer.

$$E_{binding} = h\nu - \mathrm{E_{kin(analyser)}} - \Phi_{\mathrm{analyser}} \quad (2.3)$$

(with $\phi_{analyser}$ as the work function of the analyzer).

To correct the recorded data the detected kinetic energy needs to be referenced to a peak with a known position, in this case the C1s peak at 285eV. The peak areas are furthermore corrected with the sensitivity factors for ionization probabilities of the respective atom types in order to enable the quantitative comparison of the elements.[239]

X-ray sources are usually the most intensive Kα line of Mg (1254eV) or Al (1478eV). In order to receive information on deeper areas of the studied films the XPS is equipped with a sputter system.

2.2 Microscopy

2.2.1 Field-Emission Secondary Electron Microscopy (FE-SEM)

Scanning electron microscopy is established for the mapping of surfaces with an ultra-high spatial resolution which enables structures with sizes of down to a few nanometers to be revealed. An electron beam with energy ranging from 0.5keV to 40keV is focused on the surface by two condenser lenses to a spot about 0.4nm to 5nm in diameter. The focused beam is subsequently used for scanning the surface by reflection in different x and y axes.[244,245]

In order to avoid any interaction of the electron beam with the atmosphere, electron microscopy is conducted under ultra-high vacuum conditions. By the contact of the electrons and the sample surface the electrons are decelerated and transfer kinetic energy to the atom surface matrix which results in the emission of x-ray, auger-electrons and secondary electrons. In the case of secondary electron microscopy, the latter ones are detected. The recorded signal intensity depends on the position of the scanned surface to the detector and the sample material. The signal intensity is visually represented: regions with high signal intensity are illustrated brightly and areas with low signal intensity are darker. Scanning the surface results in the displaying of the surface morphology with lateral resolution in the same size as the diameter of the electron spot.

2.2.2 Atomic Force Microscopy (AFM)

Atomic force spectroscopy is a technique used for the investigation of nanoscopic surface topographies with ultra-high resolution. In contrast to scanning electron spectroscopy, it has the advantage that the studied surface does not necessarily need to be electrically conductive.

Furthermore, it also reveals information about the material phases which is obtained by mapping the sample surface with an ultra-thin cantilever tip. Topographical inhomogeneities lead to variety of electrostatic forces between the tip and the upper atom layer on the surface and thereby to attractive or repulsive forces which are detected by the effected bending of the cantilever. A laser is focused on the backside of the cantilever, the deflection of which directly corresponds with the cantilever bending. The recorded data is visually represented and shows the investigated surface structure. The reachable height resolution of AFM is thereby dependent on the investigated material but in the range of 1–2 Å.

2.3 Electrochemistry

2.3.1 Height-Regulated Scanning Kelvin Probe (HR-SKP)

The Kelvin probe is a contact-free technique for the measurement of the outer electric potentials (Volta potentials) of metals which can be conducted under various conditions. It obtains measurements under high vacuum, inert gases and corrosive or humid atmospheres.

If a charge unit e is transferred from the infinite vacuum level into a metallic phase, work needs to be expended whereby the uncharged state of the metal corresponds to the Galvani potential φ (inner electrical potential) which consists of two components, the Volta potential (outer electric potential) ψ and the dipole potential χ (surface electric potential).

$$\varphi = \psi + \chi \tag{2.4}$$

The Volta potential ψ is affected by excess electrical charge supplied from the outside and needs to be overcome to bring the charge unit from the infinite distance to a point in the vacuum adjacent to the surface of the given phase but outside the range of interfacial forces. If the charge is transferred further on in the direction of the metallic phase, the electric forces of the interfacial dipole layer need to be overcome. This dipole or surface electric potential results from an excess of negative charge outside of the phase and an excess of negative charge inside the phase, respectively.

In the case of the transportation of electrons or ions from one phase into another phase, not only does the effect of electrostatic fields need to be considered, but also the transportation of matter.

Thus not only electrical work but also chemical work is required. To transport 1 mol of species i with the charge z from infinity into the phase requires the electrochemical potential $\tilde{\mu}$

$$\tilde{\mu}_i = \mu_i + z_i F \varphi \tag{2.5}$$

(with μ as chemical potential of i in the respective phase, F as the Faraday constant).

If, furthermore, an electrochemical reaction is taking place at the interface of a metal (called the "sample" in this case) and an electrolyte, the electrochemical work necessary to transfer charged matter of the species i from the electrolyte into the metal phase can be thermodynamically described as a Galvani-potential difference between the solid phase and the electrolyte phase. In the case of thermodynamic equilibrium, the potential difference $\Delta\varphi_{electrolyte}^{sample}$ is

$$\Delta\varphi_{electrolyte}^{sample} = \frac{\mu_i^{0(electrolyte)} - \mu_i^{0(sample)}}{z_i F} + \frac{RT}{z_i F} ln\left(\frac{a_i^{(electrolyte)}}{a_i^{(sample)}}\right) \tag{2.6}$$

(with μ^0 as the chemical potential of the species i in the respective phase for standard conditions, R as the universal gas constant, T as the temperature and a as the activity of species i in the respective phase).[246-249] The absolute half-cell potential results in

$$\varepsilon_{electrolyte}^{sample} = \Delta\varphi_{electrolyte}^{sample} - \frac{\mu_e^{sample}}{F} \tag{2.7}$$

(with $\varepsilon_{electrolyte}^{sample}$ as the half cell-potential between the sample and the electrolyte and μ_e^{sample} as the chemical potential of electrons in the sample phase).

If the sample is furthermore electrically conductively connected with another metal, the Fermi levels of both metals are equalized due to thermodynamics, something which causes positive and negative exceeded charges in the respective phases. The corrosion potential E_{Corr} between both metals is then described by the Galvani-potential differences of both half-cells. In the case of Kelvin probe measurements, the second half-cell is an inert chromium nickel alloy (called "ref"), the total half-cell potential of which is described by the Galvani-potential difference between the metallic phase and its gaseous environment. The corrosion potential E_{Corr} of the sample/electrolyte/reference/environment cell is therefore[56,59,250]

$$E_{Corr} = \varepsilon^{sample}_{electrolyte} + \varepsilon^{ref}_{environment} \tag{2.8}$$

$$= \left(-\frac{\tilde{\mu}_e^{ref}}{z_e F} - \chi^{enviroment}_{electrolyte} - \Delta\varphi^{ref}_{environment} \right) + \Delta\psi^{ref}_{electrolyte} \tag{2.9}$$

(with z_e as electron charge, $\tilde{\mu}_e^{ref}$ as the electrochemical potential of electrons within the reference phase, $\chi^{environment}_{electrolyte}$ as the dipole potential at the interface electrolyte/gaseous phase, $\Delta\varphi^{ref}_{environment}$ as the Galvani-potential difference between the reference and the environment, and $\Delta\psi^{ref}_{electrolyte}$ as the Volta potential difference between the reference and the electrolyte).

In thermodynamic equilibrium the half-cell potential of the reference is, as described above, constant for the given environment and thereby the electrochemical potential $\tilde{\mu}_e^{ref}$ is constant, too. Since the electron charge $z_e = 1$ and the dipole potential $\chi^{environment}_{electrolyte}$ is assumed to be small (0.05V)[251] the term in brackets in Eq. 2.9 can be regarded as nearly constant. For the corrosion potential follows[244-246]

$$E_{Corr} \approx \Delta\psi^{ref}_{environment} \tag{2.10}$$

Thus the Volta potential difference $\Delta\psi^{ref}_{electrolyte}$ changes linearly with the corrosion potential. For the experimental approach the measured Volta potential is compared with a $Cu/CuSO_4$ half-cell with a known corrosion potential of + 320mV vs standard hydrogen electrode (SHE).[245,246] A chromium nickel needle with a diameter of around 100µm is conductively connected to the investigated sample. The needle is located planar near the sample surface so that it can work as a condenser (see Fig. 2.2).

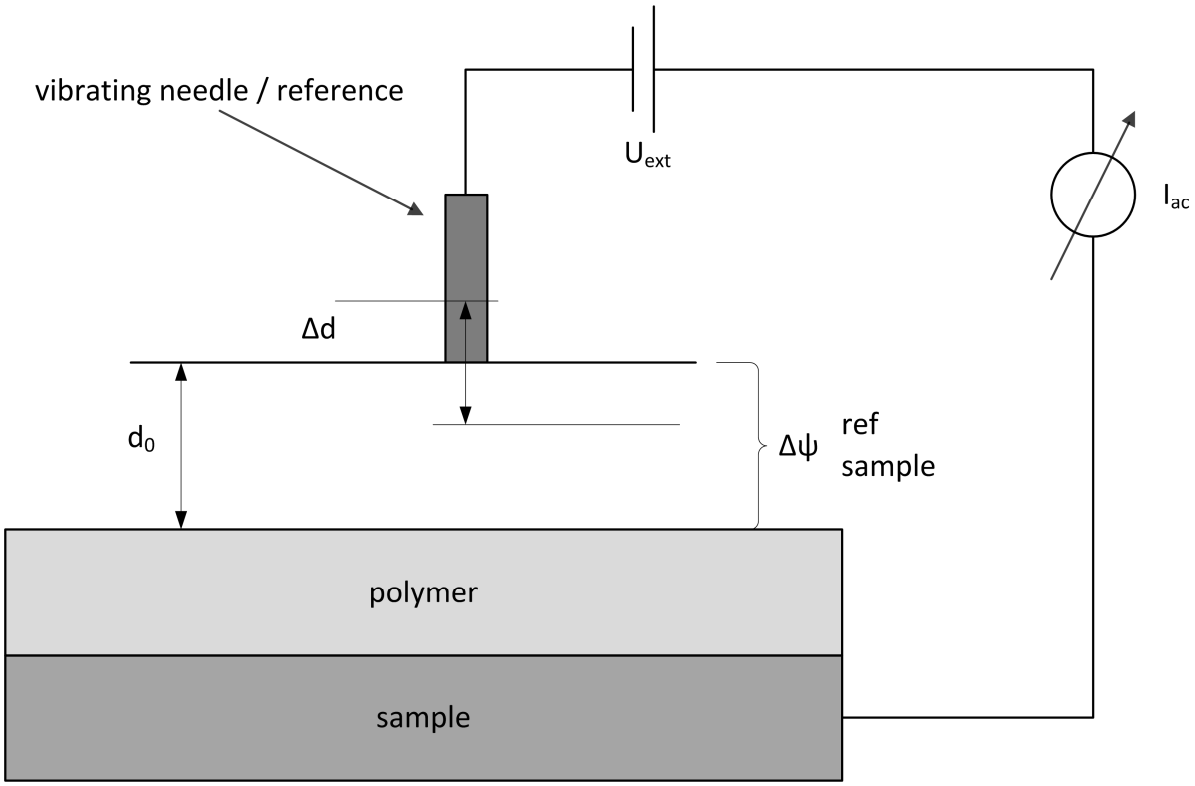

Fig. 2.2: Principles of a Kelvin Probe setup.[56]

Any process occurring at the sample/electrolyte, sample/oxide/electrolyte or sample/polymer/electrolyte interfaces results in a change of the Volta potential Δψ and thereby in a change of the charge of the condenser. This change of the condenser charge ΔQ corresponds with the change of the capacitance C

$$\Delta Q = (\Delta\psi + U_{ext})\Delta C \tag{2.11}$$

(with U_{ext} external counter voltage).

The change of charge is compensated by an external voltage U_{ext} which is equal to – Δψ. The compensation of the charge guarantees unaffected electrode kinetics and therefore an unhindered measurement of the Volta potential. In order to minimize the influence of the interfering signals and to meet metrological requirements of the electronics, the needle moves with sinusoidal oscillation.[252] In this way the distance d between the condenser plates is also oscillating

$$d(t) = d_0 + \Delta d\cos(\omega t) \tag{2.12}$$

(with t as time, ω as the angular frequency and d_0 as the mean plate/sample distance). Since the condenser capacity C is dependent on the plate distance

$$C = \frac{\varepsilon_0 \varepsilon_r A}{d} \tag{2.13}$$

(with A as the plate area, ω_0 as the dielectric constant in vacuum and ω_r as the material-dependent dielectric constant) and a periodic change of the capacitance C results in

$$C(t) = \frac{\varepsilon_0 \varepsilon_r A}{\delta t} = \frac{\varepsilon_0 \varepsilon_r A}{d_0 + \Delta d cos(\omega t)} \tag{2.14}$$

The resulting current

$$I(t) = \frac{\delta Q(t)}{\delta t} = (\Delta\psi + U_{ext}) \frac{\delta C(t)}{\delta t} \tag{2.15}$$

can again be compensated by the external current U_{ext}, the amplitude of which is displayed as the requested Volta potential difference vs. SHE after calibration to Cu/Cu^{2+} redox equilibrium.

2.3.2 Electrochemical Impedance Spectroscopy (EIS)

Since the corrosion processes at the metal/electrolyte interfaces are characterized by the transportation of charged matter from the liquid phase to the solid one or vice versa not only the fundamental thermodynamics need to be considered with respect to the velocity of the corrosion process, but also the kinetics of the transportation of charged matter. By this the overcoming of energetic barriers is the rate determined step with respect to the electron transfer reaction.

Fundamental electrochemical impedance spectroscopy is the illustration of these barriers by the equivalent electronic devices. These equivalent circuits contain in their simplest form a parallel connected ohmic charge transfer resistor R_{CT} and a double layer capacitance C_{DL} which are both connected in series to another ohmic resistor R_{el}. The first part describes the electric double layer at the metal/electrolyte interface with its charge transfer resistance and the resistance of the capacitance while the latter one characterizes the resistance of the electrolyte. The condenser illustrates the EDL either according to the Jellium model or as caused by the specific adsorption of

counter ions to charged metal surfaces. Both states form contrary charged layers which illustrates the macroscopic properties of a plate condenser.[246,249]

In order to guarantee investigation of the impedances of the different electronic barriers without distortion, an alternating current with a slight amplitude of a few mV around the open circuit potential (OCP) is applied to a three-electrode arrangement where the working electrode is the sample and the counter electrode is made of an inert material, like gold or platinum. During the EIS measurement the frequency of the AC range varies, usually between 10^{-2} Hz and 10^{6} Hz, and is given by

$$U(t) = U_0 \sin(\omega t) \tag{2.16}$$

(with U_0 as the voltage amplitude, ω as the angular rate and t as the time). The resulting current I is subsequently phase-shifted by φ depending on the influence of the capacitance

$$I(t) = I_0 \sin(\omega t + \varphi) \tag{2.17}$$

(with I_0 as the current amplitude). Thereby the angular rate is directly connected to the applied frequency f

$$\omega = 2\pi f \tag{2.18}$$

The impedance Z results from Ohm´s law as

$$Z(\omega) = \frac{U(t)}{I(t)} = \lfloor Z \rfloor \frac{\sin(\omega t)}{\sin(\omega t + \Delta\varphi)} \tag{2.19}$$

and afterwards the capacitance C as

$$C = \frac{1}{\omega \lfloor Z \rfloor} \tag{2.20}$$

The measured impedances are evaluated depending on the frequency and the phase shift. The results are often presented as a Bode plot as illustrated in Figure 2.3 which corresponds to the electrode system introduced above.[253-256]

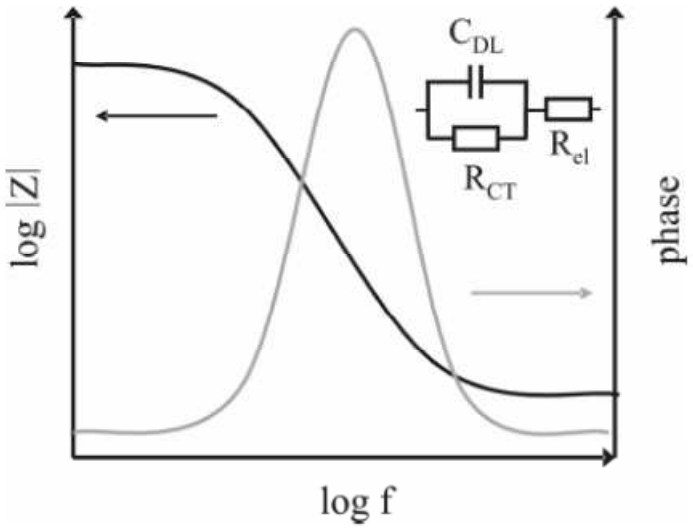

Fig. 2.3: Bode plot and equivalent circuit for a simple electrochemical electrode system.[56]

For high frequencies the double layer resistance is "short-circuited" and the complete impedance can be assigned to the electrolyte R_{el} which is confirmed by a phase shift of zero. In the case of low frequencies, the phase shift is also zero but the current flows over the layer resistance while the recorded impedance is the sum of that and the resistance of the electrolyte R_{el}. At AC frequencies between these extremes the phase shift increases up to a shift of nearly 90° which is caused by a dominating capacitor C_{DL} and enables the calculation of its value according to Eq. 2.20.

In the case of a polymer-coated substrate, at least one more capacitor for the coating C_C and in parallel connection its corresponding ohmic layer resistance R_C is effective, which usually dominates all other circuit elements in the case of a closed-porous layer matrix. Thereby the Bode plot illustrates high phase values over a wide frequency range.[245,257]

2.3.3 Cyclovoltammetry (CV)

Cyclovoltammetric measurements enable the calculation of surface coverage degrees of coated metallic substrates.[258-260] The current density peaks according to the oxidation of the corresponding metal are compared to the ones measured on bare substrates. In the case of zinc, the cyclovoltammogram is initiated at -1.2V_{SHE} for the purpose of reducing the passive films formed at uncovered surface spots or inside pores. Since the progress of polarization towards -0.7V_{SHE} is rapidly performed by 100mV/s the potential of anodic zinc dissolution at -0.943V_{SHE} (pH 8.9 in the borate buffer) is reached when the surface is still free of oxides due to thermodynamics. Hence all bare

surface spots are oxidized if the oxidation potential (-0.943V_{SHE}) is reached, which enables the calculation of the surface coverage degree γ by

$$\gamma = 1 - \frac{A_{coat}}{A_o} \tag{2.22}$$

(with A_{coat} as the area of the oxidation peak on the coated sample and A_0 as that recorded on the corresponding bare substrate). After approaching -0.7V_{SHE} the CV cycle is closed by potential reduction to -1.2V_{SHE} where the freshly formed oxide film is reduced by achievement of -0.83V_{SHE} which occurs simultaneously with hydrogen evolution. Since the detected current densities are a maximum of around 1 mA/cm^2 it can be assumed that the electrochemical processes are unaffected by the diffusion processes and thereby independent of pore geometries.

3 Experimental Procedure

3.1 Materials and chemicals

3.1.1 Substrate materials

The metallic substrates used for the conducted studies were pure iron (Good Fellow, purity 99.5%) and pure zirconium (Good Fellow, purity 99.8%) as well as commercial cold rolled steel (CRS), hot dipped galvanized steel (HDG), electro galvanized steel (ZE) and aluminium alloy 6016 (Al6016).

In order to achieve smooth and clean surfaces, the pure iron and zirconium sheets were firstly polished down to 1 µm and subsequently cleaned in ethanol (VWR, purity 99.9%) in an ultrasonic bath for 10 minutes. After cleaning in the ultrasonic bath, each substrate was rinsed with pure ethanol (VWR, purity 99.9%) and subsequently dried in a stream of nitrogen.

The commercial substrates (CRS, HDG, ZE and Al6016) were cleaned by alkaline pretreatment (Chemetall GmbH; Gardoclean S5176) for 3 min in a 60 °C warm bath under strong stirring. The bath was composed according to the directive delivered by Chemetall and subsequently set to pH 12 by adding nitric acid. All samples were rinsed with water after the cleaning procedure, dried in a nitrogen stream and immediately coated or converted in order to avoid contamination and repassivation of the bare surfaces.

3.1.2 Layer chemistry

Zirconium-based conversion layers were applied to the iron substrates by immersing them into an acidic, aqueous conversion bath containing hexafluorozirconic acid, H_2ZrF_6 (Sigma–Aldrich; 50 wt% solution in water), which was supplied as a 50 wt% solution in water. This solution was then diluted with water, leading to a H_2ZrF_6 bath with a concentration of 1 mM which was additionally adjusted to pH 4.2 by using a 3% Na_2CO_3 solution. The conversion film formation on the substrates was conducted by immersion of the iron sheets for 3 min into a moderately stirred conversion bath at

room temperature. Subsequently, samples were rinsed with deionized water and dried in a stream of nitrogen. The resulting film thickness of the ZrO_x layers was determined by means of ellipsometry to around 140 nm.

Organosilane adsorption layers onto iron were prepared by using an aqueous solution of γ-aminopropyltriethoxysilane (γ-APS) which was supplied by Sigma-Aldrich (purity ≥ 98%). The concentration of the solution was set to 1 wt% and the pH value to 4.2. The film formation was carried out by 2 min immersion of the substrates into the non-stirred γ-APS bath. Subsequently, all samples were rinsed with deionized water, dried in a nitrogen stream and tempered for 1 h at 70 °C.

Organosilane-based hybrid-layers were deposited from hybrid-systems by immersion of CRS, HDG, ZE and Al6016. These solutions were composed by adding 11.5 g/l of an alkaline solution of precondensed γ-APS to an aqueous solution containing 22.5 g/l H_2ZrF_6 and manganese nitrate. In the case of the copper containing hybrid-systems, 5 ppm copper nitrate (Copper ICP standard, Merck, Germany) was additionally added to the conversion baths. Both systems were afterwards set to pH 4.2 by using a 3% Na_2CO_3 solution and moderately stirring. Each substrate was coated by 3 min immersion, subsequently rinsed with deionized water and finally dried in a nitrogen stream.

Post-treatment of freshly applied hybrid-layers with octadecylthiol (ODT) and octadecylphosphic acid (ODPA) was conducted in order to block the submicroscopic surfaces inside nanopores in the layer matrix. The hybrid-layers were post-treated with either ODT or ODPA or a 50/50 mixture of both.

The ODT and ODPA (Alpha Aesar GmbH & Co KG, Germany) solutions were prepared under nitrogen atmosphere in water-free ethanol (VWR, purity 99.9%). The concentrations for both compounds were 1mM and the SAM adsorption was performed by 1.5 h immersion of the previously hybrid-layer-coated substrates. The entire process was conducted in a glove box under nitrogen atmosphere. Subsequently the samples were rinsed with deionized water and ethanol.

Modification of the hybrid-layers with silica clays and 2-(methylthio)benzothiazole (MTBT) encapsulated into poly(dimethylamino)ethyl methacrylate (PDMAEMA) as well as Mg-LDH-VO_3 was conducted by adding 0.5 g/l of the corrosion inhibitors to the freshly prepared γ-APS/H_2ZrF_6 solution. Subsequently, the modified baths were stirred strongly for 1 h and the substrates were finally coated following the procedure of the unmodified hybrid-layer.

3.2 Analytical methods

3.2.1 Fourier-transformed infrared reflection–absorption spectroscopy (FT-IRRAS)

The chemical composition of the conversion and adsorbate layers was analyzed by means of FT-IRRAS (Vertex 70, Bruker) or Micro-FT-IRRAS (Hyperion, Bruker). FT-IRRAS was conducted under grazing incidence (78°) using a deuterated triglycine sulfate detector (DTGS) in order to reveal the integral chemical composition of the analyzed films. Micro-FT-IRRAS studies additionally enabled the detection of microscopic heterogeneities of the film formation and its chemical composition. Therefore a grazing incidence reflection unit (angle of incidence: 80°) was used which was set to a scan region of 200µm x 200µm. The signal detection was analyzed by a cryogenic mercury cadmium tellurid detector (MCT). The limited scan area enabled the study of ex-situ the local degradation of the adsorption/conversion films as a result of cathodic delamination. For each FT-IRRAS and Micro-FT-IRRAS measurement, 512 scans were collected with an energy resolution of 4 cm^{-1}. Moreover the aperture was set to 6 mm.

3.2.2 Ellipsometry

One wavelength multi-angle ellipsometry was conducted by means of an EP^3 (Nanofilm) using a HeNe laser with 532 nm and an angle range of 42–80° in 2° steps. The refractive index n used for fitting the raw data was set to 1.46 for the y-APS layer and to 2.18 for the ZrO_x layer. For both layers the extinction coefficient was set to zero.

3.2.3 X-Ray photoelectron spectroscopy (XPS)

The chemical composition of the upper atomic layers was analyzed on coated samples by means of X-Ray photoelectron spectroscopy. The instrument used was a Quantum2000 (Physical Instruments, USA) at the MPI für Eisenforschung GmbH. Survey and element spectra were collected using a monochromatic Al Kα x-ray source with a 23.9 eV pass energy. Charge effects on the investigated layers were corrected by correlation of all recorded binding energies (BE) to the C1s peak at 285 eV.

3.2.4 Contact angle measurements (CA)

In order to reveal the coverage of zirconium surfaces with different self-assembled monolayers (SAMs), CA measurements were conducted. A DS-A10 video contact angle analyzer (Krüss, Germany) was used while on each sample three drops were analyzed. The recorded data was finally averaged.

3.2.5 Atomic Force Microscopy (AFM)

The morphology of the deposited films and bare substrates were investigated by means of Atomic Force Microscopy (AFM). AFM topography imaging was performed by means of a JPK Nanowizard II Ultra System (JPK Instruments, Berlin, Germany). The system was equipped with an anti-noise and -vibration box to minimize environmental influences during imaging. All AFM measurements were carried out in intermittent contact mode (IC) under ambient conditions in air using cantilevers of type *NSC15* (Mikromash, Estonia) with a resonance frequency of about 320 kHz and a force constant of 40 N/m. AFM imaging was carried out at constant amplitude, which was damped to 98–90% of the free amplitude for optimal sample–tip interaction. The scan speed was adjusted between 1–2 µm per second at a scan resolution of 512 x 512 pixels.

3.2.6 Field-emission secondary electron microscopy (FE-SEM)

The surface morphologies of the deposited conversion layers were studied by means of secondary electron spectroscopy. Field emission scanning electron microscopy was conducted using a 1540 XB CrossBeam (CarlZeiss SMT) under high vacuum (below $2x10^{-6}$mbar). The accelerating voltage and the working distance were varied between 2kV and 5kV and 1.9 mm and 2.2 mm, respectively. SE2- or inLense-detectors were used for imaging.

3.2.7 Height-Regulated Scanning Kelvin Probe (HR-SKP)

Electrochemical processes at the metal/metal oxide/adsorbate interfaces were studied by means of a height-regulated Scanning Kelvin Probe (HR-SKP). The HR-SKP line scans were measured using a vibrating NiCr needle with a tip diameter of 100 µm. To achieve a defined transition region between an artificial defect area and the intact surface film all investigated samples were protected by a residue-free tape on one side and then coated with the respective layer system. The defect area was filled with 0.5M sodium chloride solution stabilized with 3% Agar. The scanning was simultaneously

started at the transition border from the defect to the coated area which ensured the detection of the initial phases of the substrate/adsorbate interface reactions.

3.2.8 Linear sweep voltammetry (LSV)

The inhibition of the cathodic and anodic currents which results from the electrochemical reaction during the delamination process was studied by means of linear sweep voltammetry (LSV). An electrochemical cell with an area of 0.786 cm^2 was filled with an aerated borate buffer (0.05 M $Na_2B_4O_7*10H_2O$ + 0.05M $NaSO_4$ + 0,2M H_3BO_4; pH value 8.3) as electrolyte. The electrochemical cell was arranged with the studied sample as a working electrode and an ultra-pure gold wire (99.9999% purity) as the counter-electrode. The potential decrease in the Helmholtz layer was measured by a Ag/AgCl reference (198mV vs. SHE) electrode which was equipped to a potentiostat (Reference 600, Gamry Instruments). The potential during the measurement was varied around the open circuit with a potential sweep rate of 1 mV/s. The LSV studies were recorded after 1 min of equilibrium time.

3.2.9 Electrochemical impedance spectroscopy (EIS)

The barrier properties and pore resistances of the adhesion and conversion layers were studied by conducting EIS measurements. The same arrangements as made for the cells used for LSV were made, containing an ultra-pure gold wire (99.9999% purity) as the counter-electrode as well as a Ag/AgCl (198mV vs. SHE) reference electrode. The survey areas were adapted to the size of the investigated samples and hence varied between $3.14*10^{-2}$ cm^2 and 0.79 cm^2. Non-corrosive measurements were made in an aerated borate buffer (0.05M $Na_2B_4O_7*10H_2O$ + 0.05M $NaSO_4$ + 0.2M H_3BO_4; pH value 8.3) whereas studies in a corrosive environment were recorded by cycles of electrochemical measurements in 0.5M sodium chloride solution. The impedances were recorded by a potentiostat (Reference 600, Gamry Instruments) under frequency modulation from 100kHz to 0.1Hz. All measurements were started after 1 min of equilibrium time.

3.2.10 Cyclovoltammetry (CV)

Cyclovoltammetry was performed to enable the calculation of the degree of surface coverage on coated samples. The same electrochemical cells were used as were used for LSV and EIS. The non-corrosive experiments were performed in a borate buffer solution (0.05M $Na_2B_4O_7*10H_2O$ + 0.05M $NaSO_4$ + 0.2M H_3BO_4; pH value 8.3; T = 295K) with a scan rate of 100mV/s whereas corrosive studies

were recorded by cycles of CVs in 0.5 M sodium chloride solution. The scan rate of all measurements was set to 100mV/s and started after 1 min of equilibrium time.

4 Results and Discussion

4.1 Studies of the chemical composition, morphology and corrosion stability of ultra-thin inorganic/organic bilayer films on pure iron substrates

4.1.1 Chemical composition of γ-APS films

In order to characterize the functional groups and crosslinking of the γ-APS layers, FT-IRRAS data were measured after film deposition on polished iron substrates (Figure 4.1.1a). The corresponding peak positions and assignments are illustrated in Table 1. The γ-APS layers are mainly characterized by a TO (transverse optical) and an LO (longitudinal optical) mode of an asymmetric Si-O-Si stretching vibration, which appear at 1060cm^{-1} and 1130cm^{-1}.[286-289] This functional group is a result of the condensation of Si-OH functions of γ-APS inside the aqueous solution and of subsequent crosslinking during the annealing step of the deposited γ-APS films for 1 h at 70 °C.[290] The influence of the annealing of freshly applied γ-APS films on the IRRAS peak intensities and positions is shown in Figure 4.1.1b. The remaining Si-OH functions are characterized by a symmetric stretching mode at 930cm^{-1}.[286,287]

In the region between 1000cm^{-1} and 1200cm^{-1}, C-O-Si vibrations also appear beside the asymmetric Si-O-Si stretching modes.[291] Since the Si-O-Si bands are much more intense than the C-O-Si bands the latter ones are overlapped by the Si-O-Si vibrations and thus not marked in the spectrum. Another siloxane peak appears at 815cm^{-1} which can be assigned to the deformation vibration of the Si-O-Si function.[286]

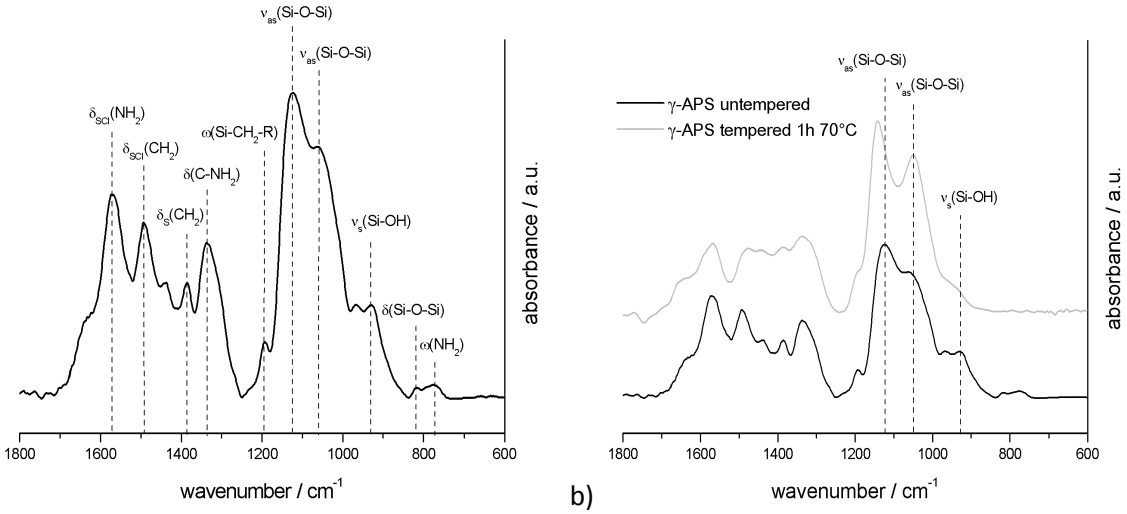

Fig. 4.1.1: FT-IRRAS spectra of γ-APS films on iron (background: alkaline-cleaned iron surface): a) untempered layer; b) comparison of an untempered γ-APS film and a γ-APS film tempered at 70 °C for 1 h

Table 4.1.1: Peak positions and assignments of FT-IRRAS data of γ-APS-based adsorbate layers on iron

wavenumber / cm^{-1}	assignment [286-291]
775	$\omega(NH_2)$
815	δ(Si-O-Si)
930	ν_s(Si-OH)
1060	ν_{as}(Si-O-Si)
1130	ν_{as}(Si-O-Si)
1190	ω(Si-CH$_2$-R)
1330	δ(C-NH$_2$)
1390	δ_s(CH$_2$)
1490	δ_{SCI}(CH$_2$)
1570	δ_{SCI}(NH$_2$)

After curing the organosilane film for 1 h at 70 °C, the collected spectrum showed a decrease in the symmetric stretching peak which is attributed to the silanol function, indicating the further crosslinking of the organosilane matrix via Si-O-Si bonds.[290] Additionally, the LO mode of the Si-O-Si peaks is blue shifted by 20cm^{-1} which reveals a denser network of the polymer matrix.

4.1.2 Surface morphology of γ-APS films

In Figures 4.1.2a–d the AFM images and corresponding line profiles of the just-polished and the additionally film-coated iron surfaces are compared. It becomes obvious that the applied and cured γ-APS film only partially imitates the surface roughness, and that the film thickness is higher for the valleys of the substrate, leading to a smoothening of the apparent surface. Ellipsometric measurements conducted on the γ-APS-coated iron samples revealed a film thickness of around 10nm which evidences the adsorption of an ultra-thin film. Moreover, the AFM image of the film-coated surface (see Fig. 4.1.2b) shows globular structures with diameters of less than 10nm.

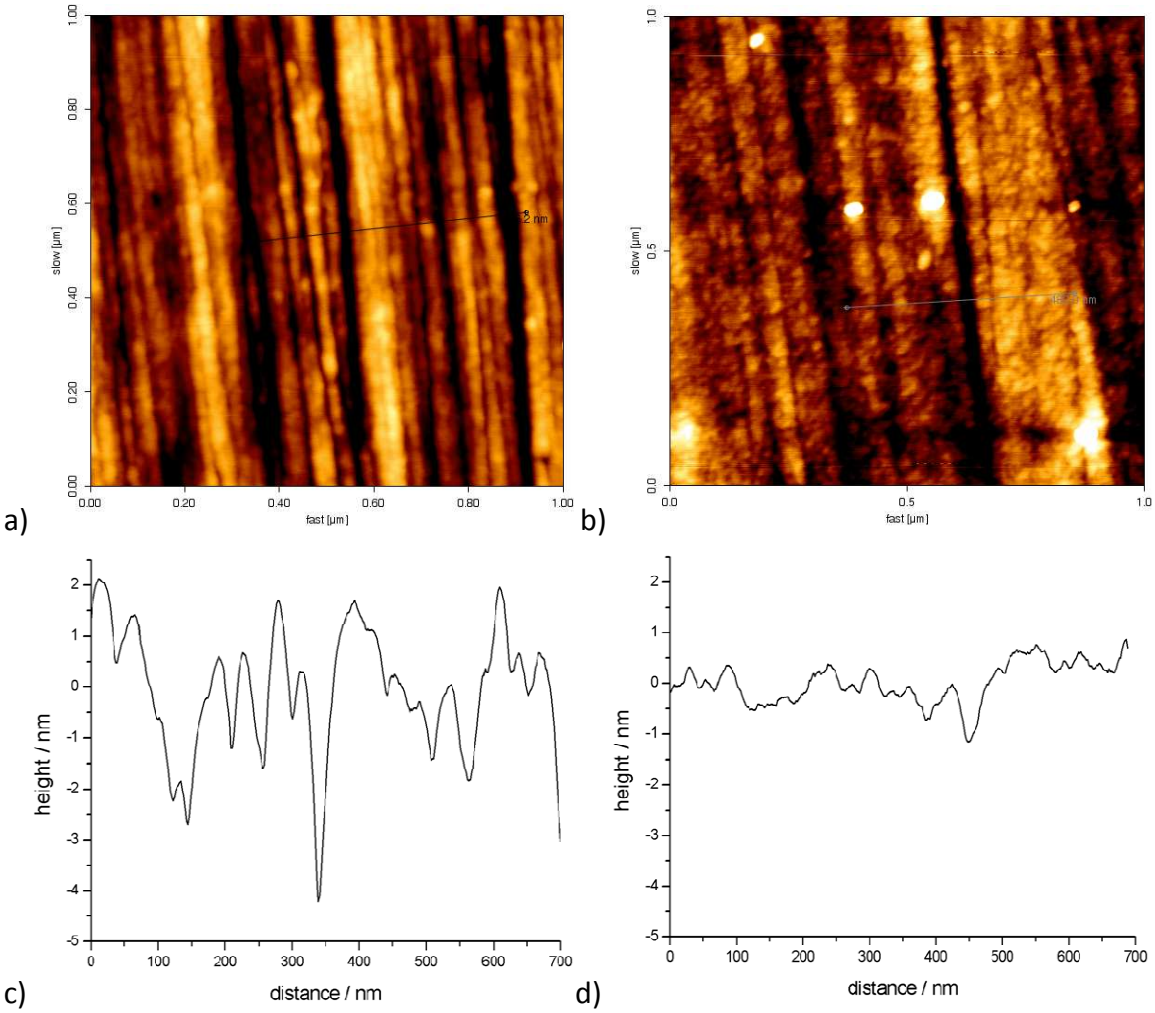

Fig. 4.1.2: Images and corresponding height traces from AFM on a bare iron surface and an iron-coated layer with a γ-APS-based adsorbate: (a, c) alkaline-cleaned iron surface without adsorbate layer; (b, d) γ-APS adsorbate layer-coated iron.

4.1.3 Chemical composition of zirconia/ γ-APS bilayer films

The spectrum of the ZrO_x-film precipitated from a H_2ZrF_6 conversion bath is illustrated in Figure 4.1.3a. Characteristic of the inorganic layer are two broad peaks at 690cm^{-1} and 560cm^{-1}. Both are assigned to asymmetric Zr-O-stretching modes. The detailed assignments of both bands were reported for different polymorph zirconia samples.[292-295] It was concluded that both peaks are skeletal vibrations of a Zr-O network which is either dominated by asymmetric Zr-O-Zr vibrations or by O-Zr-O vibrations. However, the half-band-width (HBW) of the bands suggests a dispersion of vibration states, which is characteristic for an amorphous network.

Furthermore, the spectrum in Figure 4.1.3 shows a large amount of surface water which is characterized by the water deformation vibration around 1650cm^{-1} and the stretching vibration around 3450cm^{-1}. The peak at 3450cm^{-1} illustrates moreover that water is incorporated in a hydroxyl-rich film.

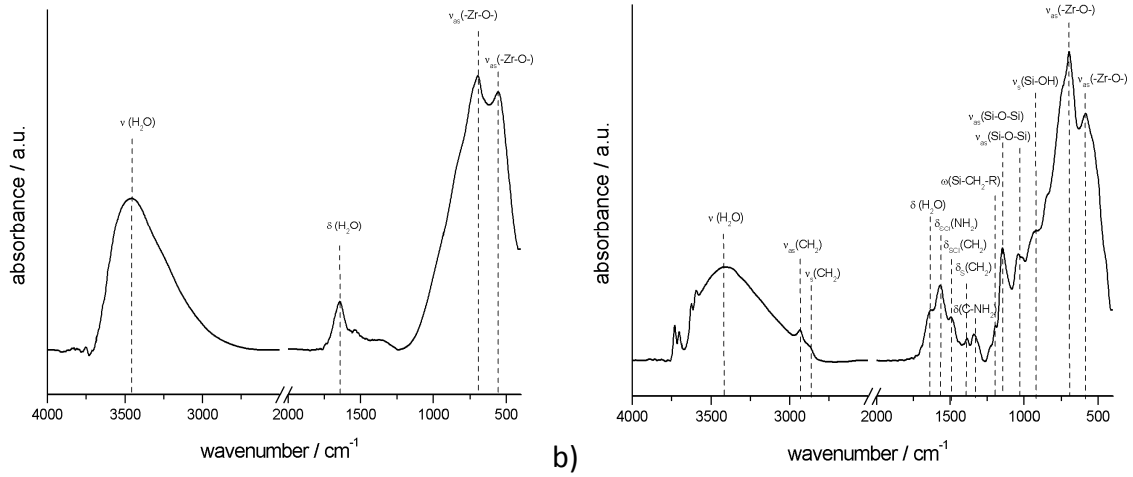

Fig. 4.1.3: FT-IRRAS spectra of inorganic-organic bilayer system based on zirconia conversion and γ-APS adsorbate films on iron (background: alkaline-cleaned iron surface): a) spectrum of zirconia layer b) spectrum of zirconia/γ-APS bilayer.

The inorganic film as characterized in Figure 4.1.3a was afterwards coated with a γ-APS layer as mentioned above. The deposited layer was annealed for 1 h at 70 °C and subsequently examined by means of ellipsometry and FT-IRRAS. The collected infrared absorption spectrum is illustrated in Figure 4.1.3b. It shows the same peaks as the pure γ-APS layer (Table 4.1.1) which evidences that γ-APS adsorbs not only on bare passive iron but also on zirconia-covered iron. Therefore, it is assumed that the adsorption of γ-APS on zirconia follows the same process as the film formation on iron.

Additionally, it was observed that the water which was primarily included in the ZrO_x matrix was not removed from the inorganic matrix by annealing for 1 h at 70 °C (see Fig. 4.1.3). This shows that the water is obviously strongly bound within the ZrO_x network via hydrogen bonds.

4.1.4 Surface morphology of zirconia/γ-APS bilayer films

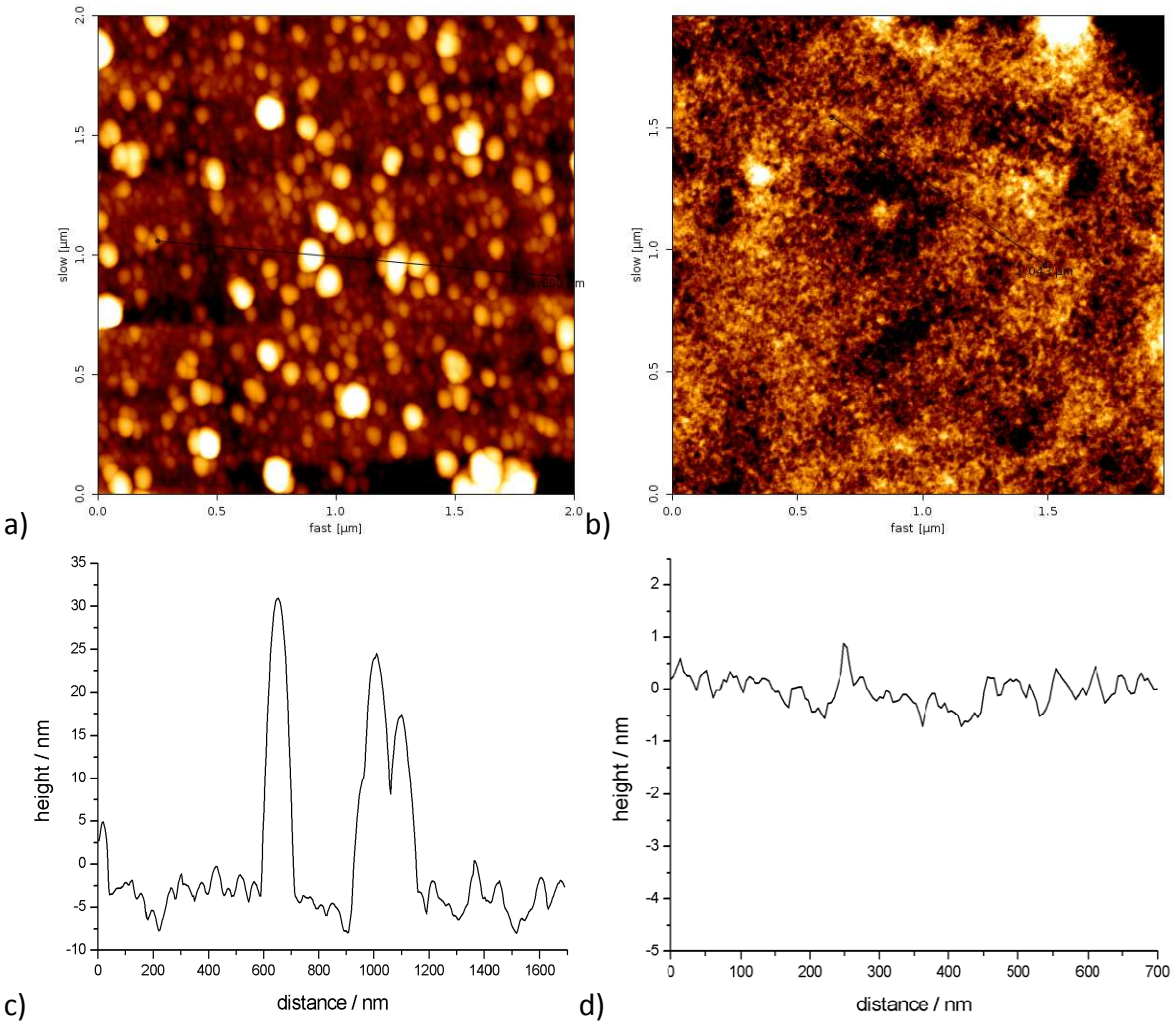

Fig. 4.1.4: AFM topographic images of iron coated with (a, c) ZrO_x conversion layer and (b, d) ZrO_x/γ-APS bilayer.

In Figures 4.1.4a–d the AFM images and corresponding line profiles of iron coated with a zirconia single layer system and a zirconia/γ-APS bilayer system are compared. The applied zirconia conversion layer shows the growth of globular zirconia particles, which reach diameters of up to tens of nanometers. Subsequent applied and cured γ-APS films led to a decrease of the surface roughness which was also observed on the pure organosilane-coated iron surfaces.

Ellipsometry measurements of the bilayer system revealed a film thickness of around 40 nm for the γ-APS layer and around 140 nm for the zirconia layer.

4.1.5 Potential/current density studies on zirconia/ γ-APS bilayer films

Potentiodynamic polarization curves were recorded by means of linear sweep voltammetry on a pure iron surface and on iron surfaces covered with zirconia and organosilane single layers as well as one sample coated with a zirconia/organosilane bilayer. The applied potential was anodically and cathodically shifted starting from the open circuit potential. The monitored anodic and cathodic current densities are illustrated as Tafel plots in Figure 4.1.5 and reveal an inhibition of both the cathodic and the anodic current densities by all applied films. Comparing both single layer systems with the alkaline-cleaned bare iron surface, the LSV results revealed an even stronger inhibition of the cathodic current densities by the ZrO_x-film than by the γ-APS-film. It can be concluded that this result is caused by the insulating properties of zirconia due to its wide band gap as well as a result of a high crosslink density of the purely inorganic film.

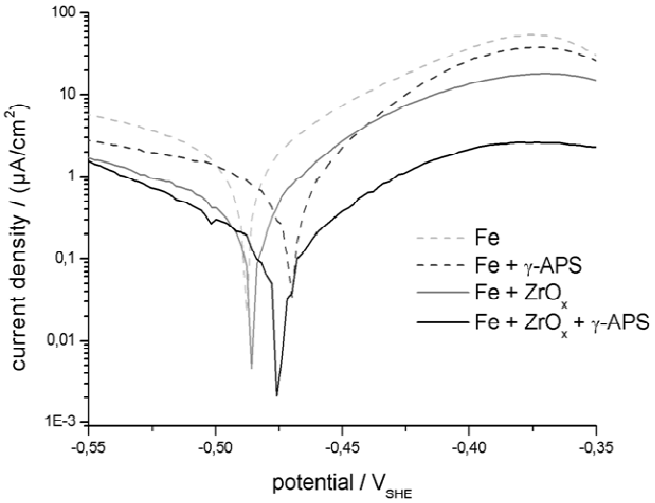

Fig. 4.1.5: Linear sweep voltammetry on iron coated with conversion layers based on mono- and bilayer systems of zirconia and γ-APS.

The LSV-Tafel curve for zirconia/γ-APS bilayer films revealed an even higher inhibition of both the cathodic and the anodic processes as compared to the single zirconia layer and single γ-APS layer. It can be assumed that the existing pores in the zirconia film are covered with the additional γ-APS film so that both the cathodic and anodic processes which are likely to occur in nanoscopic defects are further inhibited.

4.1.6 Cathodic delamination and film degradation along the iron/coating interfaces

The inhibition of the cathodic current densities is directly connected to the inhibition of cathodic de-adhesion or electrowetting processes. To prove this correlation HR-SKP measurements were performed on film-covered iron substrates.

4.1.6.1 Cathodic delamination on γ-APS films

HR-SKP electrowetting studies were performed starting from an artificial defect area in order to study the migration of hydrated ions along the metal/oxide/polymer interfaces and the simultaneously occurring cathodic delamination.[53-55,60-62] The progress of cathodic electrowetting leads to a steep increase in the measured local interfacial corrosion potential which directly characterizes the delamination front. Therefore, electrowetting studies on the bare oxide-covered iron surface and the organosilane film-covered iron were conducted (see Fig. 6). Posner et al. illustrated that the basic mechanism of ion transport from an electrolyte-filled defect area along the oxide-covered iron surface is independent of the presence or absence of a coating since the cation migration is mainly affected by the electric field between the defect area and the intact metal surface.[296,297]

The process started from a defect filled with a 0.5 M NaCl electrolyte and reached a progress of migration of nearly 5.5 mm after 8 hours for an uncoated iron oxide/iron interface (see Fig. 4.1.6a). For the γ-APS-coated iron the front of cathodic oxygen reduction proceeded by only around 3 mm along the iron/iron oxide/organosilane interface for the same length of time (see Fig. 4.1.6b).

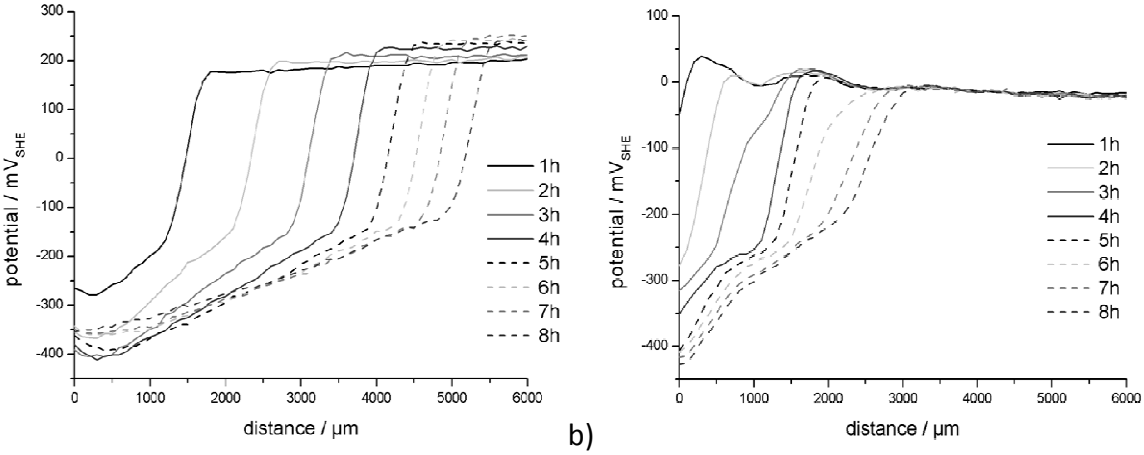

Fig. 4.1.6: SKP line scans of γ-APS film-coated iron during the cathodic electrowetting process and micro-FT-IRRAS spectra along the front after SKP measurement: a) alkaline-cleaned iron surface without adsorbate layer; b) γ-APS layer-coated iron;

4.1.6.2 Cathodic delamination on zirconia/γ-APS bilayer films

The electrowetting studies of the zirconia/organosilane bilayer-coated iron substrates were conducted in comparison to the SKP studies which were carried out on samples covered with the organosilane adsorbate single layer (see Fig. 4.1.6).

It can be assumed that the corrosion-induced ion migration on the zirconia-covered iron occurs mainly on the zirconia/organosilane surface and not at the iron oxide/zirconia interface since the zirconia matrix is stable under conditions of oxygen reduction.

However, for the purely ZrO_x film-covered iron substrates the kinetics of electrowetting were even slower than for the purely γ-APS-covered iron surface. As can be deduced from Figure 4.1.7a, within 8 hours a progress of the delamination front of only 2.5 mm was observed which is in agreement with the smaller oxygen reduction current densities as measured by LSV.

The SKP studies of the bilayer-coated iron substrates (see Fig. 4.1.7b) showed the slowest progress of electrowetting leading to a progress of only 2 mm in 8 hours which also agrees with the results of the linear sweep voltammetry (see Fig. 4.1.5) since the bilayer coating revealed the smallest cathodic current densities in comparison to both single-layer systems.

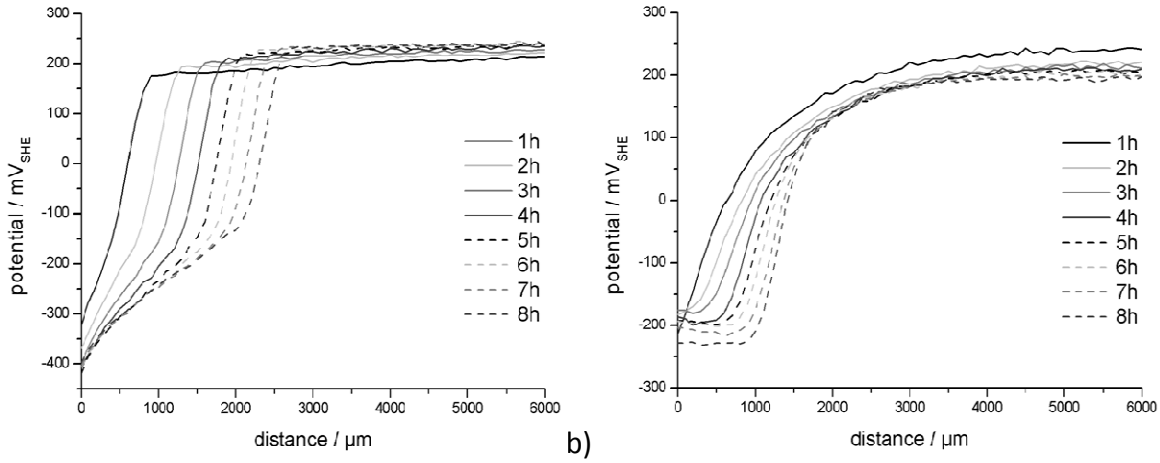

Fig. 4.1.7: SKP line scans of zirconia/γ-APS bilayer-coated iron during the cathodic electrowetting process and micro-FT-IRRAS spectra along the delamination front after SKP measurement: a) zirconia conversion layer-coated iron; b) zirconia/γ-APS bilayer-coated iron.

4.1.7 Conclusions

It has been shown by FT-IRRAS analysis that thin γ-APS adsorbate layers can be deposited on conducting metal surfaces, which were studied on pure iron samples, as well as semi-conducting metal surfaces, which were conversion layers of zirconium mixed oxides. Further crosslinking of the organosilane adsorbate films was achieved by annealing for 1 h at 70 °C. Moreover, free silanol groups led to further condensation reactions during the curing process.

Ultra-thin amorphous zirconia layers were deposited on the iron samples prior to γ-APS adsorption in order to increase the barrier properties of the resulting bilayer system. It was shown that zirconia conversion layers result in the coverage of the iron surface by a nano-rough layer.

With regard to the corrosion protection properties of the different films, we have shown that the organosilane and zirconia single layers as well as the zirconia/γ-APS bilayer system inhibit the cathodic and anodic processes. Moreover, the inhibition of the oxygen reduction process at the electrolyte/electrode interface was able to be directly correlated with the kinetics of electrowetting under atmospheric conditions.

However, the stronger inhibition of cathodic currents by the zirconia single layer than by the γ-APS single layer was assumed to be caused by the higher ZrO_x film thickness and the large band gap of the zirconia matrix which causes high insulating properties of the inorganic film. Additionally, it can be assumed that the zirconia film is highly crosslinked. The promotion of the barrier properties of the

insulating zirconia film by an additional γ-APS film is assumed to be caused by the covering of the pores inside the primary zirconia film.

As shown by the HR-SKP studies, the progress of cathodic oxygen reduction along the iron surface is inhibited for both single-layer systems, based on γ-APS and zirconia. The fact that the progress of cathodic electrowetting is even more strongly inhibited by the zirconia than by the organosilane layer is assumed to be a result of the high stability of zirconia under the conditions of oxygen reduction. Moreover, we conclude that the oxygen reduction at the γ-APS single layer system occurs at the whole substrate/γ-APS interfacial region but only in pores of the undamaged inorganic matrix at the zirconia single layer system. This is additionally the reason why we assumed that the cathodic delamination on the γ-APS/zirconia-bilayer system proceeds at the γ-APS/zirconia interface and not at the iron/zirconia interface area.

4.2 Comparative studies of the chemical composition of ultra-thin zirconia/ γ-APS bilayer and organosilane-based hybrid-films on pure iron substrates

Hybrid-layers were deposited on pure iron in order to reveal a comparison to the ZrO_x/γ-APS bilayer system which was studied in section 4.1. FT-IRRAS studies were conducted to evaluate differences in the film matrices of both systems.

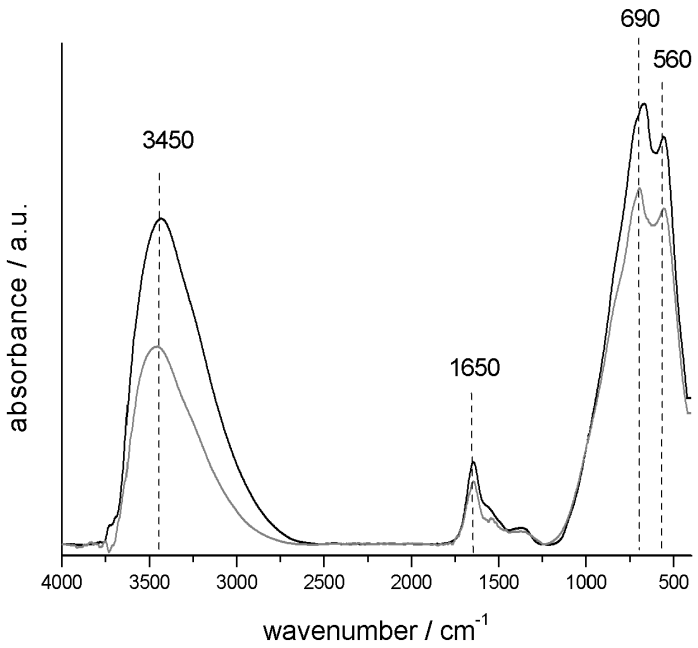

Fig. 4.2.1: FT-IRRAS spectra of pure iron after 3 min immersion into aqueous solutions containing 1 mM H_2ZrF_6 (gray graph) and 1 mM H_2ZrF_6-Additive (black graph).

Hybrid-systems were prepared by adding the precondensed γ-APS to the H_2ZrF_6-Additive containing aqueous solution. The hybrid-films were deposited by immersion of iron for 3 min into the prepared baths and subsequently also studied by FT-IRRAS (see Fig. 4.2.2). The detected spectrum was compared to the ZrO_x/γ-APS bilayer systems with respect to the revelation of differences in film thicknesses, chemical compositions or structures of the inorganic or organic matrices.

In the region between 400cm^{-1} and 1800cm^{-1}, several peak shifts appeared in the spectrum of the hybrid-layers compared to those detected in spectra of the ZrO_x /γ-APS bilayer (see Figs. 4.2.2 and 4.2.3), which concludes that the layer chemistry is not just simply a superimposition of both components. In order to simplify the evaluation of the exact peak shifts caused by the hybrid-film in contrast to the ZrO_x/γ-APS bilayer, both spectra are shown in two figures. Figure 4.2.2 illustrates the whole spectra including the hydroxyl and carbon-stretching vibrations at wavenumbers higher than 2500 cm^{-1} while Figure 4.2.3 illustrates an enlarged spectra region between 400 cm^{-1} and 2000 cm^{-1} in which significant peak shifts are observable.

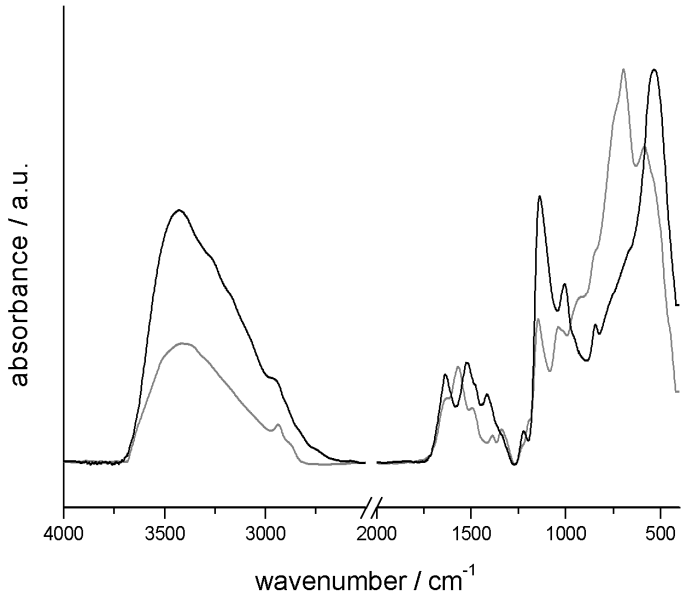

Fig. 4.2.2: FT-IRRAS spectra of pure iron after 3 min coating with 1 mM H_2ZrF_6 /1%wt γ-APS bilayer (gray graph) and the γ-APS/H_2ZrF_6 hybrid-system (black graph).

It becomes obvious from the spectrum of the hybrid-layer in Figure 4.2.2 – in agreement with the H_2ZrF_6-Additive spectrum in Figure 4.2.1 – that a large amount of water is incorporated into the hybrid-layer. It is assumed that the water, which is embedded into the matrix, was co-deposited during the conversion process. Furthermore, it can be suggested that the water molecules were formerly part of the hydrate sheath of the bath compounds.

In Figure 4.2.3 all shifted IR bands in the hybrid-layer spectrum are marked with their corresponding wavenumbers. All peaks of the ZrO_x/γ-APS bilayer spectrum are assigned as illustrated in Table 4.1.1. Comparison of the peaks assigned to the organosilane matrix spectra shows both TO and LO modes of the asymmetric stretching vibration of the Si-O-Si function as well as a scissoring vibration of the amine which appeared for the ZrO_x /γ-APS bilayer system at 1570 cm^{-1}. This peak disappeared in the spectrum of the hybrid-layer but two new ones, which are attributed to the asymmetric and symmetric scissoring mode of -NH_3^+, appeared at 1635 cm^{-1} and 1520 cm^{-1}.[298,299] The LO mode of the Si-O-Si vibration appears at around 1135 cm^{-1} and is characteristic for both the hybrid and ZrO_x /γ-APS layers. In contrast to this, the TO mode of the hybrid layer is shifted by about 60 cm^{-1} to lower wavenumbers and appears at 1000 cm^{-1}. This fact and the observation that both peaks are much broader for hybrid-layer than for the ZrO_x /γ-APS films evidences that the organosilane matrix of the hybrid-layer is chemically less densely networked via Si-O-Si links and contains more different local chemical environments in contrast to the ZrO_x /γ-APS bilayer system.

Moreover, it is obvious from the spectrum of the hybrid-layer that both bands, the TO and LO mode of the Si-O-Si vibrations, are more intense in comparison to the bands in the region between 400 cm^{-1} and 800 cm^{-1} which are assigned to the ZrO_x network. This indicates that the ratio of organosilane to zirconia is larger in hybrid-films than in the ZrO_x /γ-APS bilayer system.

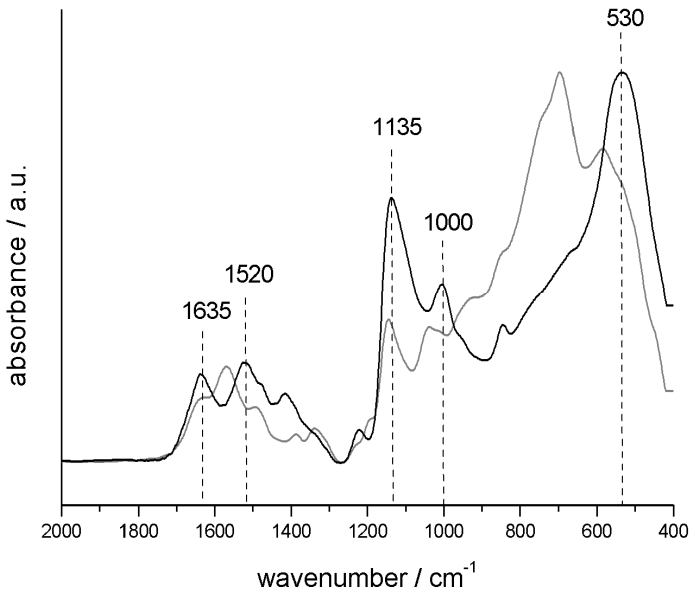

Fig. 4.2.3: FT-IRRAS spectra from 400 cm^{-1} to 2000 cm^{-1} of pure iron after 3 min coating in a 1 mM H_2ZrF_6 and 1% γ-APS and in the hybrid-system.

In order to investigate the reason for these results, film thicknesses of hybrid-layers and the ZrO_x/γ-APS films were investigated. The layer thicknesses of the hybrid-films on different commercial alloys were studied by means of FE-SEM which showed that these layers are at least 50 nm thick, independent of the substrate's nature (see section 4.3.2).

In contrast, ellipsometry measurements revealed for the ZrO_x/γ-APS bilayer system thicknesses of a few nanometers for the γ-APS film and several tens of nanometers for the zirconia film (see section 4.1.4). Thus it can be concluded that the film formation at a ZrO_x/γ-APS interface is thermodynamically superior to the aggregation at the γ-APS/γ-APS interface and that thereby the inner structure of the hybrid-layers is characterized by ZrO_x embedded into a matrix of poly-γ-APS.

This conclusion can moreover be supported by the evaluation of further FT-IRRAS peak shifts in the spectrum of the hybrid-layer with respect to the ZrO_x/poly-γ-APS bilayer. As known from SiO_2 networks, the peak shape and position strongly depend on the layer morphology.[300] Thus the disappearance of the LO and TO modes of the asymmetric ZrO_x stretching vibration at 690 cm^{-1} and 560 cm^{-1} in the spectrum of the hybrid-layer and the simultaneous appearance of a peak at 530 cm^{-1}

can also be concluded to be caused by a changed layer morphology. Both evidence a less dense inorganic lattice and different local chemical environments which are caused by the mixed, amorphous ZrO_x/γ-APS film matrix. This conclusion confirms the assumption which was drawn by the peak shifts representing the siloxane vibrations.

4.2.1 Conclusions

Overall it can be summarized that hybrid-layers are in contrast to the ZrO_x/γ-APS bilayer system mixed hybrid-films of γ-APS and ZrO_x which forms amorphous, less densely linked matrices in which water is chemically embedded.

4.3 Studies of chemical composition, morphology and corrosion stability of organosilane-based hybrid-layers on commercial CRS, HDG, ZE and Al6016

4.3.1 Substrate morphologies after precleaning

For these studies, the commercial metal alloys CRS, HDG, ZE and Al6016 were coated with the hybrid-layers. All substrates were cleaned with Gardoclean S5176 directly before application of the conversion layers. The alkaline solution was always set to pH 12 which also caused, besides the removal of all lubricants, the etching of the surfaces, especially in the case of Al6016. Figure 4.3.1 shows FE-SEM images of the surfaces of HDG, CRS, Al6016 and ZE after the cleaning process which revealed that no surface contaminations were left on any surfaces, independent of their chemical nature. In contrast to the other substrates, the Al6016 surface illustrates many small pits which are caused by intensive surface etching.

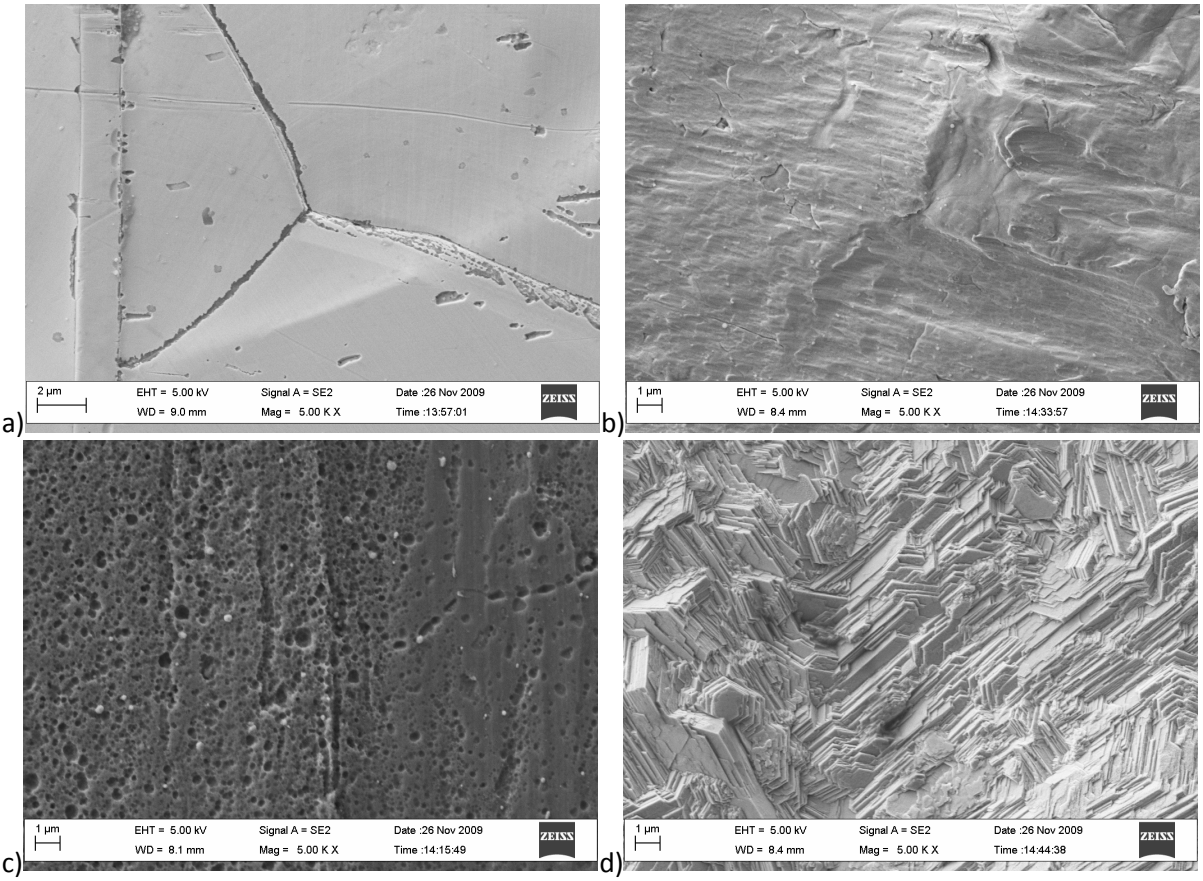

Fig. 4.3.1: FE-SEM images on alkaline precleaned with Gardoclean S5176, for 3 min, at pH 12. a) HDG b) CRS c) Al6016 d) ZE.

4.3.2 Morphologies and film thicknesses of hybrid-layers

Directly after precleaning, all samples were coated with hybrid-layers in order to avoid repassivation or recontamination of the bare surfaces. FE-SEM imaging revealed spongy layer structures on Al6016, HDG and CRS as illustrated in Figure 4.3.2. In contrast, hybrid-layers on ZE are less covering as shown in Figure 4.3.2d.

However, further studies on the hybrid-layers exposed a variety of layer structures which are assumed to be caused by small fluctuations in the conditions in the Nernst diffusion layer (NDL) during film formation. Even though the layer morphologies on different alloys can be inconsistent the formation of the hybrid-layers was always detected, which is the crucial issue with respect to the adhesion promotion and corrosion inhibition properties of those layers.

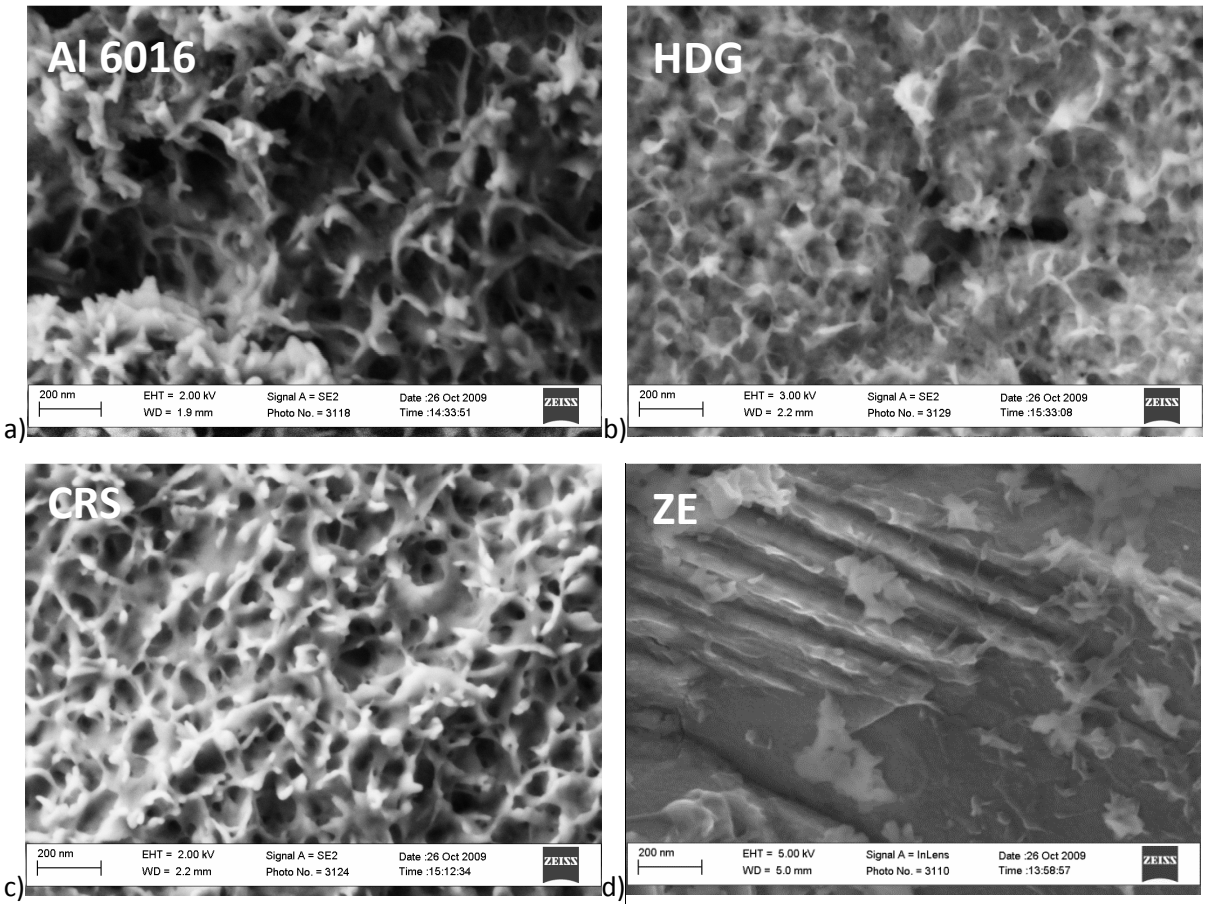

Fig. 4.3.2: FE-SEM images of Al6016, HDG, CRS and ZE coated with organosilane-based hybrid-layers. Precleaning with Gardoclean S5176 (pH 12). a) Al6016 b) HDG c) CRS d) ZE.

For the purpose of revealing the layer thicknesses, hybrid-layer-covered substrates were additionally investigated by FE-SEM after cryogenic breaking which was performed to enable the study of the breaking edge as presented in Figure 4.3.3 as an example of coated HDG. For this, a 1 mm-broad line was milled into the backside of the metal alloy sheets before immersing them into the conversion bath in order to subsequently arrange a clear side of fracture. After layer formation all samples were broken in the liquid nitrogen towards the backside in order to avoid any deformation of the hybrid-layer.

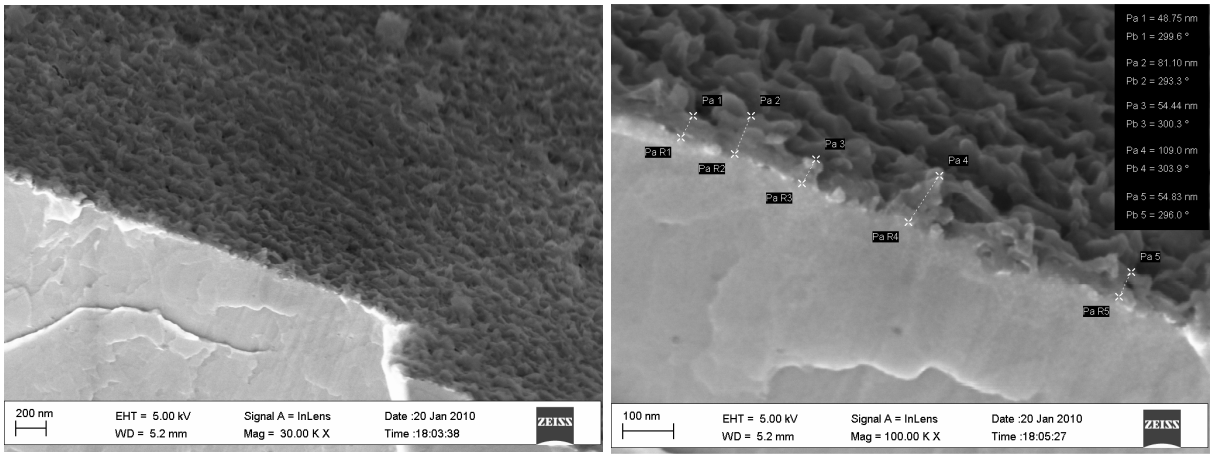

Fig. 4.3.3: FE-SEM images at breaking edges of a hybrid-layer on HDG after cryogenic breaking in liquid nitrogen.

Several FE-SEM images were collected on different spots on hybrid-layers applied to Al6016, CRS, HDG and ZE. As previously shown in Figures 4.3.2 and 4.3.3, these films are heterogeneous in their morphology and thicknesses. Therefore different spots were studied and the corresponding values were collected and subsequently averaged in order to reveal adequate results with respect to the film formation on different alloys as illustrated in Table 4.3.1

It turned out that the average hybrid-layer thickness on Al6016, CRS, and HDG is between 60 nm and 70 nm. Focusing on the single values it becomes obvious that the layer thickness varies, usually between 50 nm and 90 nm due to the spongy and nanoporous matrix. In comparison to these results the average layer thickness on ZE is around 95 nm.

Moreover, it was observed that the coverage of the ZE surface with the hybrid-layer was much lower than on Al6016, CRS and HDG, as illustrated by two examples in Figure 4.3.4. Thus it can be concluded that the homogeneous deposition of the hybrid-layer on the ZE surface is obviously hindered in comparison to the film formation on the other alloys. In contrast to the images obtained

from Al6016, CRS and HDG, on the ZE surface only a few local independent but thicker aggregates of adsorbed particles deriving from the hybrid-system were present.

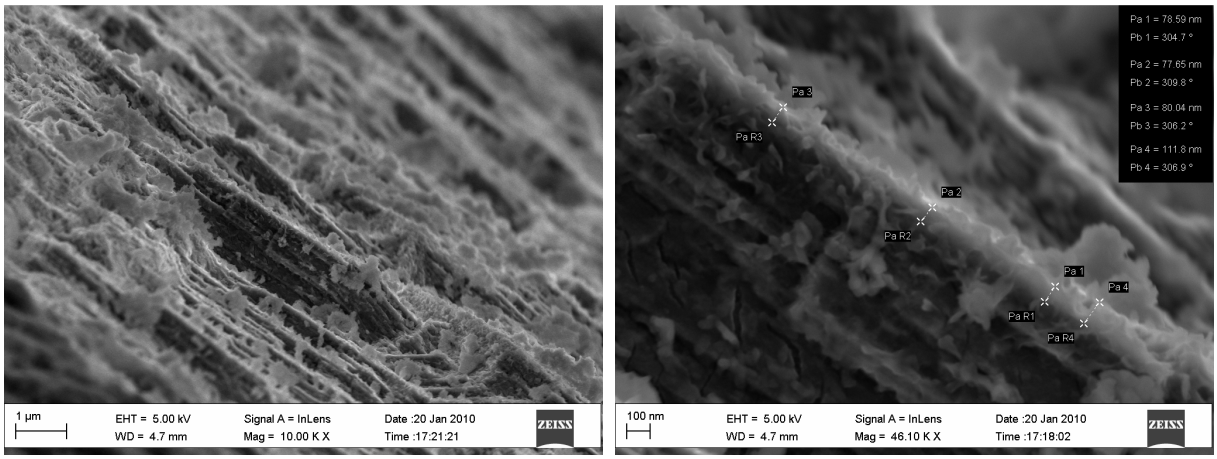

Fig. 4.3.4: FE-SEM images at breaking edges of a *hybrid-layer on ZE after cryogenic breaking in liquid nitrogen.*

Table 4.3.1: Thickness of the hybrid-layers as determined by FE-SEM analysis on Al6016, CRS, HDG and ZE.

Layer thickness / nm	Al6016	CRS	HDG	ZE
	78	66	52	79
	63	90	79	78
	99	51	76	80
	50	68	49	111
	67	82	81	133
	89	50	54	99
	35	82	109	126
	38	65	55	108
	71	68	95	85
	115	33	59	66
	54	104	70	67
	77	53	64	72
	51	47	79	83
	67	51		145
	107	51		
		70		
		66		
		32		
		58		
average	**71 +/- 19**	**62 +/- 14**	**71 +/- 14**	**95 +/- 22**

However, it should be noticed from the FE-SEM images that the hybrid-layers on different alloys are between 60 nm and 90 nm thick and that the chemical nature of the alloy surfaces has an influence on the film formation which includes both the layer thickness and the degree of surface coverage.

4.3.3 Binding states of the inorganic matrices in hybrid-layers

In order to evaluate the exact amount of substitution between F^- and HO^- at the Zr central atom of hexafluorozirconic acid during deposition of the hybrid-layers, the Zr3d peaks received by XPS element analysis on the hybrid-films were analyzed. Measurements were conducted on 180 s hybrid-layer-coated CRS, ZE, HDG and Al6016 samples and the received Zr3d peaks are illustrated in Figures 4.3.5 to 4.3.8.

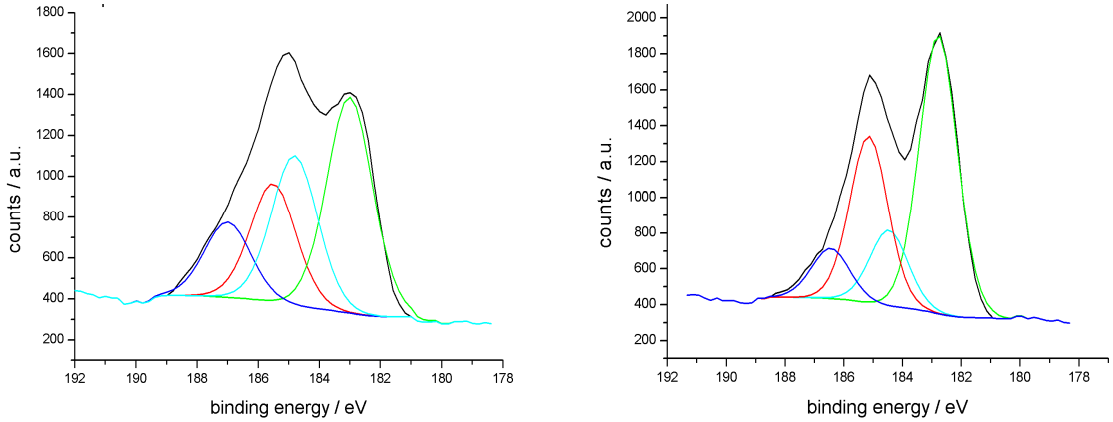

Fig. 4.3.5: Zr3d peaks of two XPS element spectra on hybrid-layer-coated CRS. Fittings show the $Zr3d_{3/2}$- and $Zr3d_{5/2}$-peaks of the Zr-O bonds (red and green curves) and Zr-F bonds (blue and cyan-blue curves).

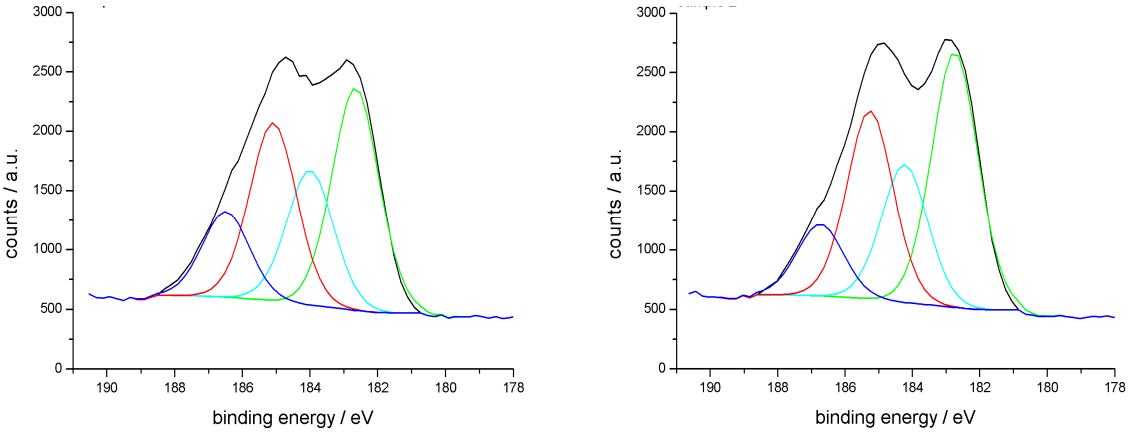

Fig. 4.3.6: Zr3d peaks of two XPS element spectra on hybrid-layer-coated ZE. Fittings show the $Zr3d_{3/2}$- and $Zr3d_{5/2}$-peaks of the Zr-O bonds (red and green curves) and Zr-F bonds (blue and cyan-blue curves).

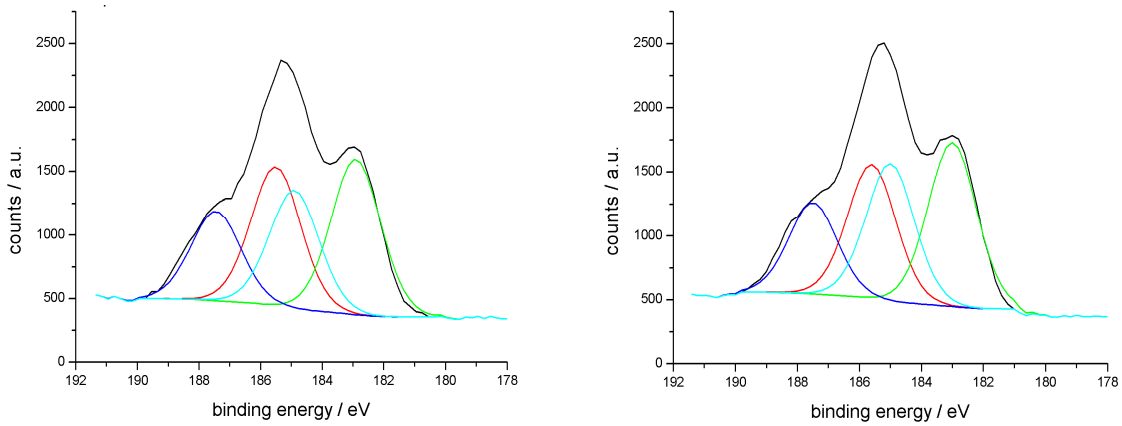

Fig. 4.3.7: Zr3d peaks of two XPS element spectra on hybrid-layer-coated Al6016. Fittings show the $Zr3d_{3/2}$- and $Zr3d_{5/2}$- peaks of the Zr-O bonds (red and green curves) and Zr-F bonds (blue and cyan-blue curves).

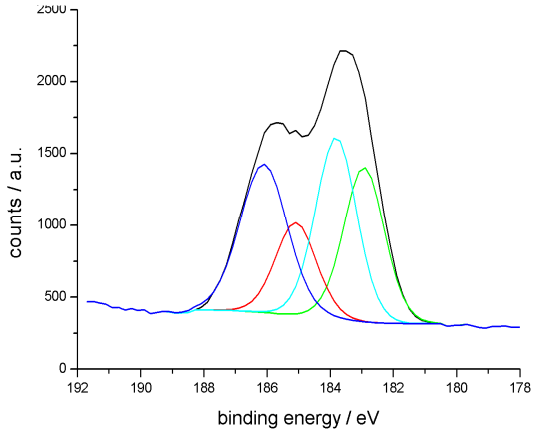

Fig. 4.3.8: Zr3d peaks of two XPS element spectra on hybrid-layer-coated HDG. Fittings show the $Zr3d_{3/2}$- and $Zr3d_{5/2}$-peaks of the Zr-O bonds (red and green curves) and Zr-F bonds (blue and cyan-blue curves).

In all spectra, the peaks of ZrO_x and ZrF_y assigned to the $3d_{5/2}$ and $3d_{3/2}$ peak-splitting due to the spin-orbit coupling were fitted. The ratios of the integrals belonging to a Zr-F bond and to a Zr-O bond for each measurement are presented in Table 4.3.2.

Table 4.3.2: Peak Areas of zirconium XPS element analysis on hybrid-layer-coated Al6016, CRS, ZE and HDG.

sample	Peak area / %				ratio O/F		
	ZrO_x		ZrF_y				
	$3d_{5/2}$	$3d_{3/2}$	$3d_{5/2}$	$3d_{3/2}$	$3d_{5/2}$	$3d_{3/2}$	average
Al6016	33	22	27	18			
	33	22	27	18			
average Al6016	33	22	27	18	**1.2**	**1.2**	**1.2**
CRS	36	24	24	16			
	48	32	12	8			
average CRS	42	28	18	12	**2.3**	**2.3**	**2.3**
ZE	37	25	23	15			
	39	26	21	14			
average ZE	38	26	22	15	**1.7**	**1.8**	**1.7**
HDG	27	18	33	22	**0.8**	**0.8**	**0.8**

From the recorded data, both average values, one for the $3d_{5/2}$ peak and one for the $3d_{3/2}$ peak, were calculated and finally averaged again. Thereby the following averaged compositions of the fluorooxozirconates were obtained dependently of the substrate:

Al6016	$\mathbf{ZrF_{2,7}O_{3,3}}$
CRS	$\mathbf{ZrF_{1,8}O_{4,2}}$
ZE	$\mathbf{ZrF_{2,2}O_{3,8}}$
HDG	$\mathbf{ZrF_{3,3}O_{2,7}}$

Obviously hybrid-layers are fluorine-rich phases where the Zr-F vibrations could not be distinguished from the Zr-O vibrations in FT-IRRAS spectra. Since the matrix densities are dependent on oxygen bonds, as are Zr-O-Zr or maybe also Zr-O-Si, the high amount of fluorine incorporated into the film leads finally to a less dense crosslinked inorganic matrix.

However, the results received by Zr3d element spectra revealed different ratios of fluorine and oxygen bonds to zirconium depending on the different chemical natures of the applied substrates.

On Al6016, CRS and ZE, oxygen ligands dominate at the zirconium central atom, and on HDG, vice versa. However, it is assumed that the oxygen bond to zirconium in the hybrid-layers is a mixture state of O^{2-} and HO^{-} since the layer matrix could not be completely oxidized without additional tempering. Thus the substitution process is assumed to end in the formation of $ZrF_yO_z(OH)_{x-z}$.-like complexes.

4.3.4 Cathodic delamination along the substrate/coating interfaces

SKP measurements were performed in-situ on hybrid-layer-coated HDG and ZE during cathodic delamination at the metal/film interface starting from a defect area which was filled with a 0.5 M NaCl/agar-electrolyte. Firstly the migration of ions along the bare, alkaline-cleaned surfaces of HDG and ZE was studied by SKP line scans in order to receive a reference for further studies on coated samples. As the electrolyte spreads from the defect area over the surface, corrosion processes start in the wetted area which results in the decrease of the Volta-potential as described for previous studies (see section 4.1.6).

The results of SKP line scans are presented in Figure 4.3.9, where the Volta-potential profiles are characterized by a sharp potential step which reflects the corrosion front. The progress of the corrosion front was studied for both samples over 8 hours. The SKP line scan revealed on ZE (Figure 4.1.9a) a corrosion front of around 6.5 mm distance from the defect transition while the one detected on HDG proceeded to around a 7 mm distance.

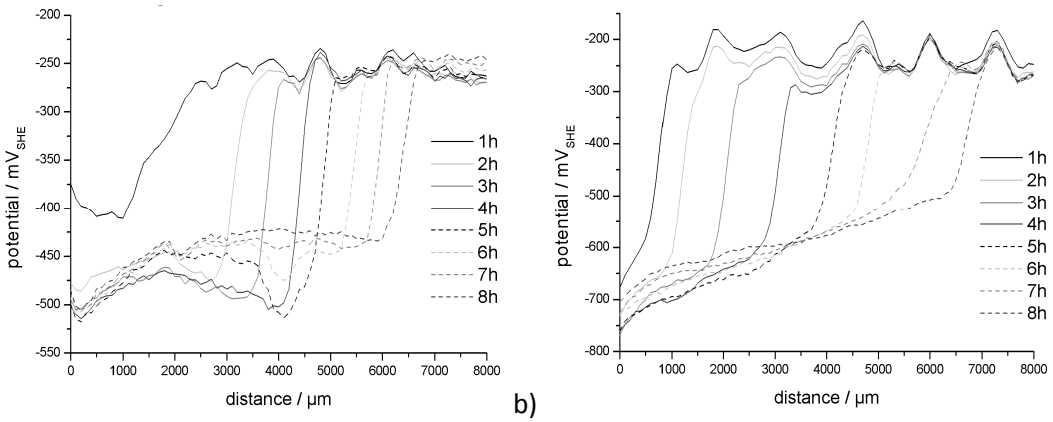

Fig. 4.3.9: In-situ SKP line scans on bare, alkaline-cleaned a) ZE and b) HDG under an oxygen-containing atmosphere during corrosion along the alloy surface starting from a defect area filled with a 0.5 M NaCl solution.

Afterwards the cathodic delamination on ZE and HDG coated with the hybrid-layers was studied. Three different coating times (30 s, 60 s and 180 s) were chosen in order to evaluate the evolution of the corrosion inhibition properties of the hybrid-layers versus the coating time. The results for ZE and HDG are presented in Figure 4.3.10 and Figure 4.3.11, respectively.

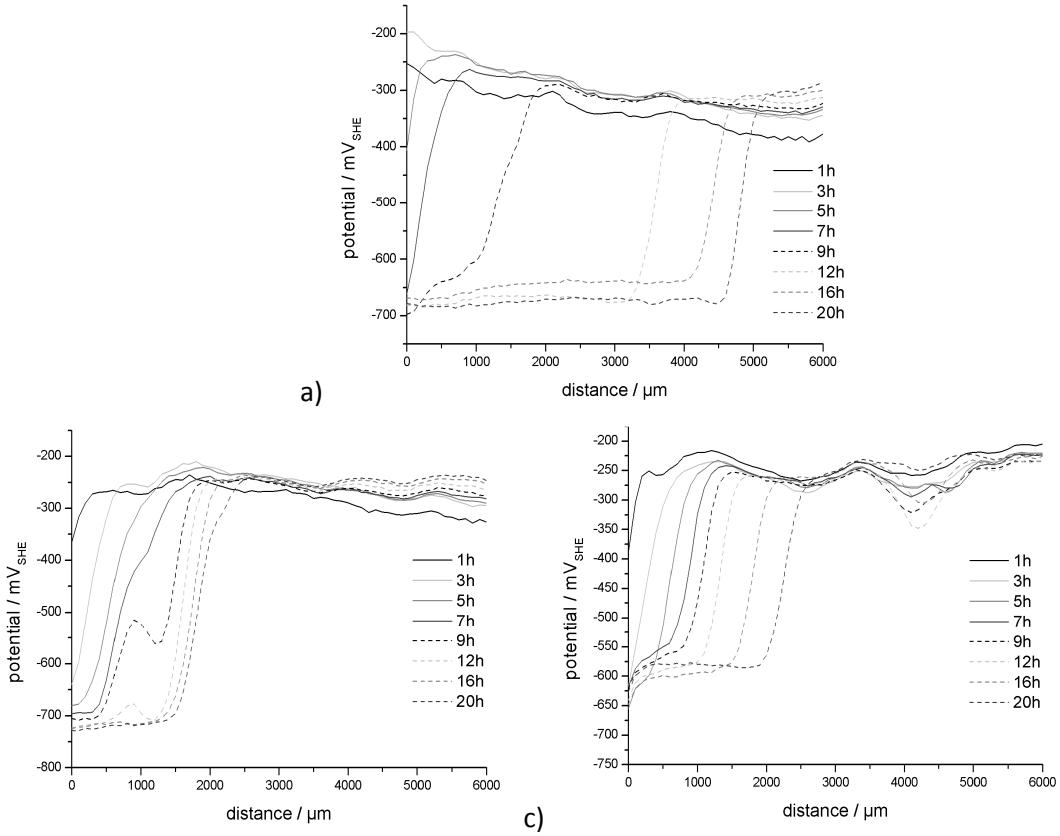

Fig. 4.3.10: In-situ SKP line scans on a) 30 s, b) 60 s and c) 180 s hybrid-layer-coated ZE during cathodic delamination of 0.5 M NaCl solution starting from a defect area.

The line scans on ZE coated with the hybrid-layer showed a good correlation between the progress of cathodic delamination and the film deposition time. A coating time of 30 s, which is shown in Figure 4.3.10a, illustrated after 20 hours of electrolyte exposure a progress of cathodic delamination of nearly 5 mm distance from the defect transition. In contrast, the results for ZE coated for 60 s (Fig. 4.3.10b) and 180 s (Fig. 4.3.10c) illustrate after 20 hours of measurement a progress of only 2.5 mm and 2 mm distance from the defect transition. Since the differences between the 60 s and 180 s coated samples are very small it can be concluded that a surface coverage with sufficient corrosion inhibition performance is mainly achieved after 60 s of coating time.

Comparing these results with the uncoated samples (Fig. 4.3.9), it is obvious that even 30 s of coating time causes a strong improvement of surface protection. After 8 hours of electrolyte exposure the corrosion front has progressed less than 1 mm in contrast to 6.5 mm on the bare ZE surface.

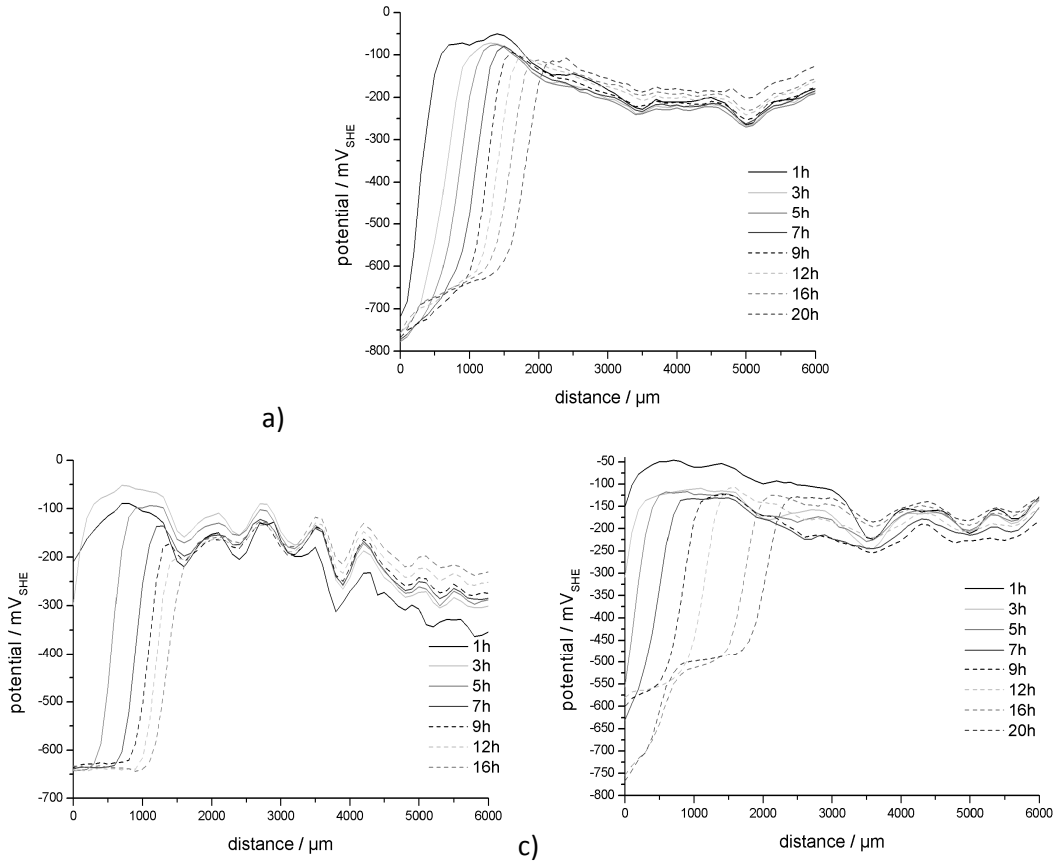

Fig. 4.3.11: In-situ SKP line scans on a) 30 s, b) 60 s and c) 180 s hybrid-layer-coated HDG during cathodic delamination of 0.5 M NaCl solution starting from a defect area.

In contrast to the SKP studies on ZE, no significant coating-time-dependent corrosion inhibition properties of hybrid-layers could be shown on HDG as illustrated in Figure 4.3.11. This result was probably caused by the different chemical nature of the HDG surface in contrast to ZE which is mainly characterized by the insulating aluminium oxide film which inhibits electric conductivity between the zinc bulk and the environment.

However, most important are the corrosion inhibition properties of the hybrid-films in contrast to the bare surface after finishing the conversion process. Focusing on the 180 s coated sample, the SKP line scans revealed after 16 hours of electrolyte impact a delamination front of less than 1.5 mm distance from the defect area. This result confirms strong anti-corrosion properties of hybrid-layers deposited on HDG which is in good agreement with the previous SKP studies on the ZE.

4.3.5 Conclusions

It was revealed by means of FE-SEM imaging that the hybrid-layers on different alloys show thicknesses between 60 nm and 90 nm which were influenced by the chemical nature of the coated alloys.

Furthermore, XPS Zr3d element analysis of the inorganic compounds illustrated that H_2ZrF_6 was partly substituted by hydroxyl groups which forms different ratios of fluorine and oxygen bonds to zirconium dependent on the different chemical natures of the applied substrates. On Al6016, CRS and ZE oxygen ligands dominate at the zirconium central atom, and on HDG, vice versa. Thereby it is assumed that the oxygen bond to zirconium in the hybrid-layers is a mixture state of O^{2-} and HO^- since the layer matrix is assumed to be partly oxidized due to thermodynamics which finally leads to the formation of $ZrF_yO_z(OH)_{x-z}$.-like complexes.

It was illustrated that the inhibition of cathodic delamination at the metal/polymer interface is significantly higher for hybrid-layer-coated metal surfaces than for γ-APS/ZrO_x bilayer-coated ones. Since it was furthermore revealed by ellipsometry and FE-SEM studies that the organosilane film in the γ-APS/ZrO_x bilayer system is around 10 nm, but in the hybrid-layers it is at least 50 nm, the latter system has a higher buffer capacitance with respect to the layer stability.

4.4 Comparative studies of the stabilities of organosilane-based hybrid-layers and zinc phosphate layers during oxygen reduction.

The conditions during oxygen reduction were simulated by periodic cathodic polarization. In order to evaluate the results achieved for hybrid-layers, they were compared to the ones received from tri-cationic zinc phosphate layers. These were chosen as a reference since this system is known for its excellent inhibition of cathodic delamination at the metal/phosphate layer interface.

Therefore a potential of -1V versus standard hydrogen electrode (SHE) was chosen to enable the simulation of conditions during oxygen reduction at the metal/polymer interface. Every cycle was run in the following sequence: firstly two measurements of CV and EIS in order to detect the initial state of the studied systems; subsequently 15 s polarization of $-1V_{SHE}$; and finally a 300 s delay to reach steady-state conditions at the interface area for thermodynamical reasons.

4.4.1 Evolution of the barrier properties on zinc phosphate layers

The results of CV and EIS on tri-cationic zinc phosphate layers deposited on HDG are illustrated in Figures 4.4.1 and 4.4.2. The results of CV measurements in Figure 4.4.1 are divided into two graphics to show the easing of the evolution of degradation within the first cycles. It was easily able to be shown that the tri-cationic zinc phosphate layers are very unstable under conditions of cathodic polarization which is revealed by the rapid increase of cathodic and anodic current densities even after 2 cycles of polarization as shown in Figure 4.4.1b.

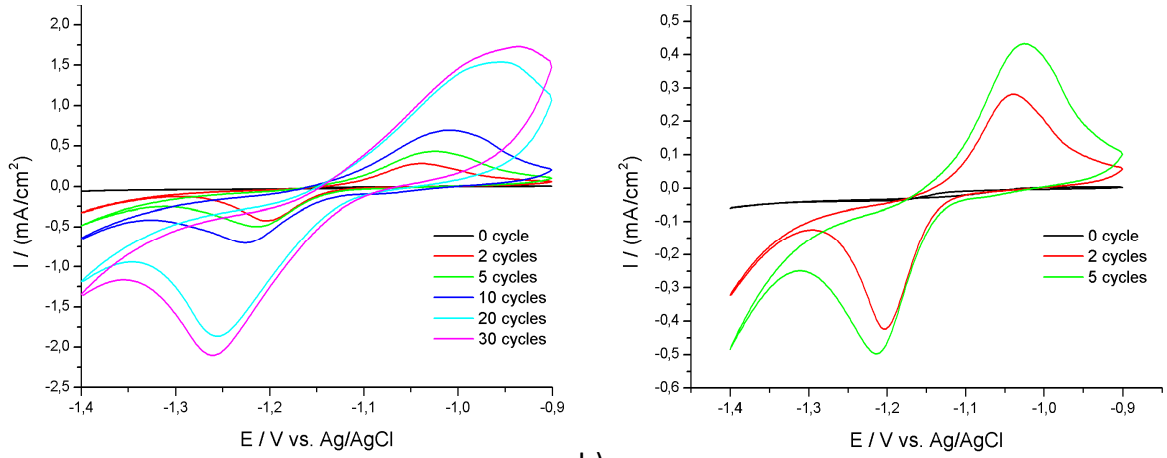

Fig. 4.4.1: Cyclovoltammetry on HDG coated with a tri-cationic zinc phosphate layer under cyclic cathodic polarization in a chloride-free borate buffer; polarization per cycle: 15 s -1V vs. SHE; a) 30 cycles; b) 5 cycles.

In order to reveal the simultaneously occurring decrease of the barrier properties, EIS measurements were also conducted during the polarization cycles, the results of which are illustrated in Figure 4.5.2, whereas the impedances are shown in Figure 4.5.2a and the corresponding phases in Figure 4.5.2b.

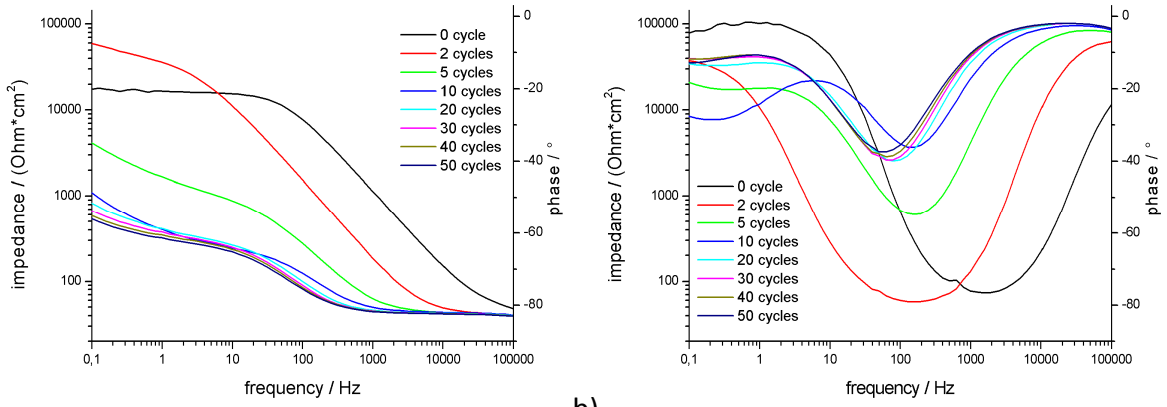

Fig. 4.4.2: Electrochemical impedance spectroscopy in a chloride-free borate buffer on HDG coated with a tri-cationic zinc phosphate layer under cyclic cathodic polarization; polarization per cycle: 15 s -1V vs. SHE; a) impedances; b) phases.

In good agreement with the CV data the barrier properties of the tri-cationic zinc phosphate layer decrease rapidly and completely disappear after 10 cycles of polarization. The remaining impedances between 0.5 and 1 kOhm cm^2 are mainly affected by the partly Al_2O_3-covered HDG surface and not by residues of the zinc phosphate layer which can be concluded by the reduced phase shifts shown in Figure 4.4.2b.

Moreover, it is obvious that the pore resistance after 2 cycles of polarization is significantly increased under simultaneous decrease of the resistance of the layer capacitance. This phenomenon might be caused by the primary dissolution of the zinc phosphate at spots of oxygen reduction and the subsequent re-deposition of these zinc phosphates inside the layer pores which is known as the "leaching effect" (see section 4.4.3). The driving force of this process is the pH gradient between the strong alkaline spots of oxygen reduction and lower alkaline areas of anodic metal dissolution which occurs inside pores at the metal/electrolyte interface.

After 5 cycles of polarization the degradation of the layer matrix is progressed so far that the leaching effect is not able to compensate it. It can be concluded that after 5 cycles of polarization the zinc phosphate layer is already widely removed from the HDG surface.

4.4.2 Evolution of the barrier properties on hybrid-layers

The results achieved by CV and EIS on tri-cationic zinc phosphate layers were moreover compared to electrochemical measurements on hybrid-layers on HDG performed by the same settings as for the previous studies. Hence equal cycles of 15 s -1V_{SHE} polarization including CV- and EIS-measurements as well as a 300 s time delay were performed. The corresponding results of CV and EIS are shown in Figures 4.4.3 and 4.4.4.

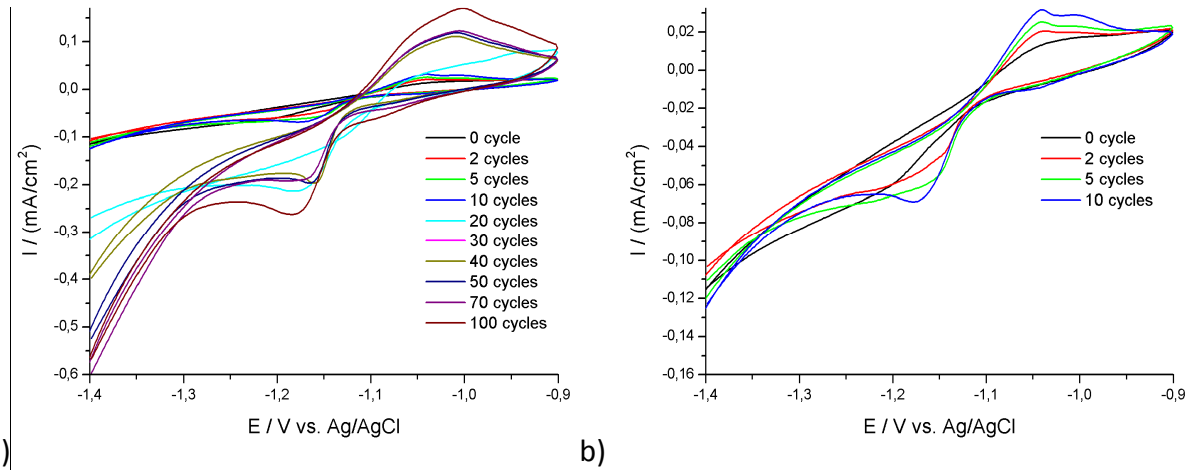

Fig. 4.4.3: Cyclovoltammetry on HDG coated with hybrid-layers under cyclic cathodic polarization in a chloride-free borate buffer; polarization per cycle: 15 s -1V vs. SHE; a) 100 cycles; b) 10 cycles.

Cyclovoltammetric studies revealed an increase of cathodic and anodic current densities with the progression of polarization time. As illustrated in Figures 4.4.3a and 4.4.3b, it is revealed that a slow

but continuous acceleration of anodic and cathodic reactions occurs which seems to stop after 40 cycles with an exception for the measurement after 100 cycles.

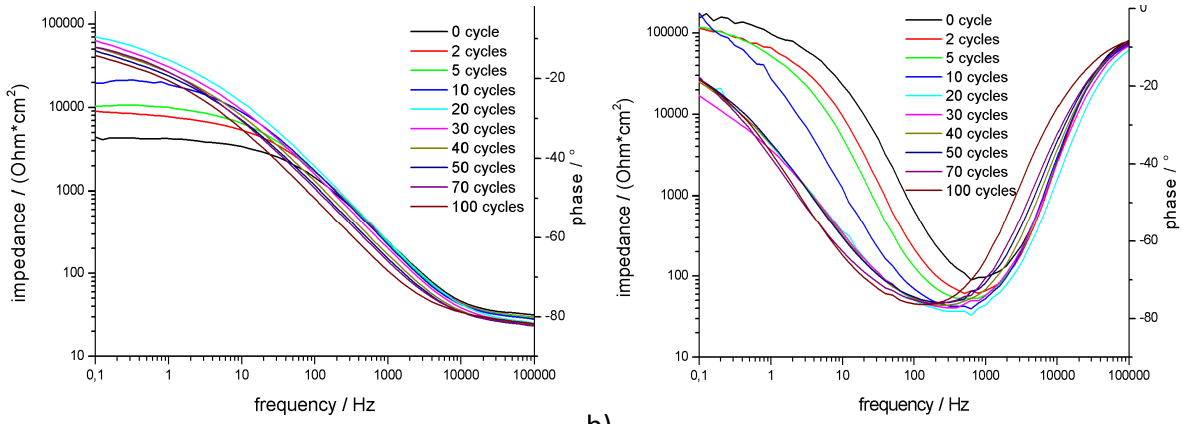

a) b)

Fig. 4.4.4: Electrochemical impedance spectroscopy in a chloride-free borate buffer on HDG coated with the hybrid-layer under cyclic cathodic polarization; polarization per cycle: 15 s -1V vs. SHE; a) impedances; b) phases.

In contrast to the results achieved for the zinc phosphate layers, hybrid-films seem to be much more stable under conditions of cathodic polarization.

Electrochemical impedance measurements illustrated that the barrier properties of the hybrid-layer are slightly reduced with the progress of polarization. Simultaneously an increase in the pore resistance could be revealed which is concluded to be caused by coverage of the metal/electrolyte interface inside the pores with corrosion products like zinc oxyhydroxides.

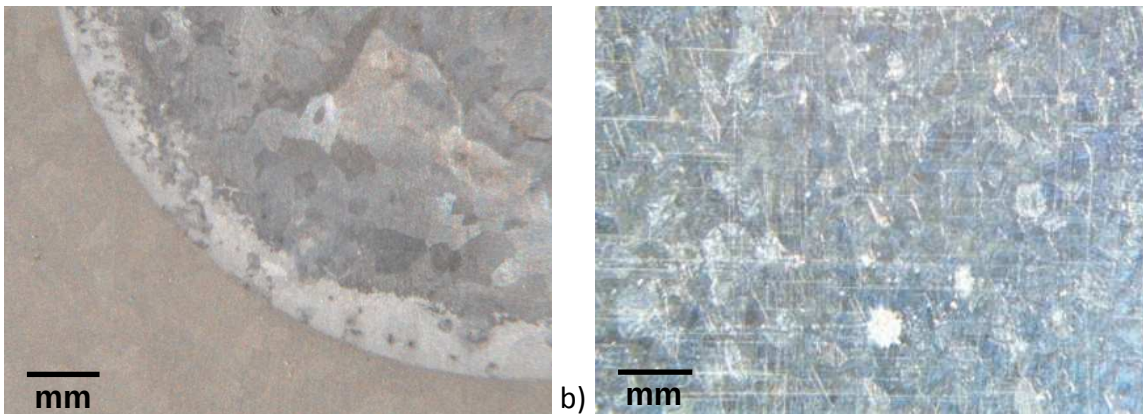

a) b)

Fig. 4.4.5: Images of HDG coated with a tri-cationic zinc phosphate layer and a hybrid-layer after 100 cycles of cathodic polarization; polarization per cycle: 15 s -1V vs. SHE; a) zinc phosphatization b) hybrid-layer.

The conclusions drawn by electrochemical measurements are furthermore confirmed by the appearances of the samples after finishing 100 polarization cycles which are illustrated in Figure

4.4.5. Both images show areas of intact coatings on the left side and areas after polarization on the right side. The zinc phosphatization is presented in Figure 4.4.5a and the hybrid-layer in Figure 4.4.5b.

It is clearly shown that the visible morphology of the hybrid-layer-coated sample remains largely unaffected at the end of the polarization studies while the tri-cationic zinc phosphate layer was completely removed from the surface.

4.4.3 Leaching effect on zinc phosphate layers

Even though no long-term stability under conditions of cathodic polarization was revealed for $Zn_3(PO_4)_2$-layers in contrast to the results received for hybrid-layers, an increase of pore resistance was detected at the beginning of polarization which was caused by a leaching effect. This phenomenon, already mentioned above, will be described in detail below with respect to its buffering and repassivation abilities.

As illustrated in Figure 4.4.6, leaching of the $Zn_3(PO_4)_2$ is mainly effected by the low-alkaline stability of the crystalline layer matrix, which dissolution is especially accelerated at spots of high pH with respect to oxygen reduction. Hence it can be kept in mind that the zinc phosphate leaching is caused by cathodic processes whereas the dissolution of the galvanized zinc is a pure anodic process.

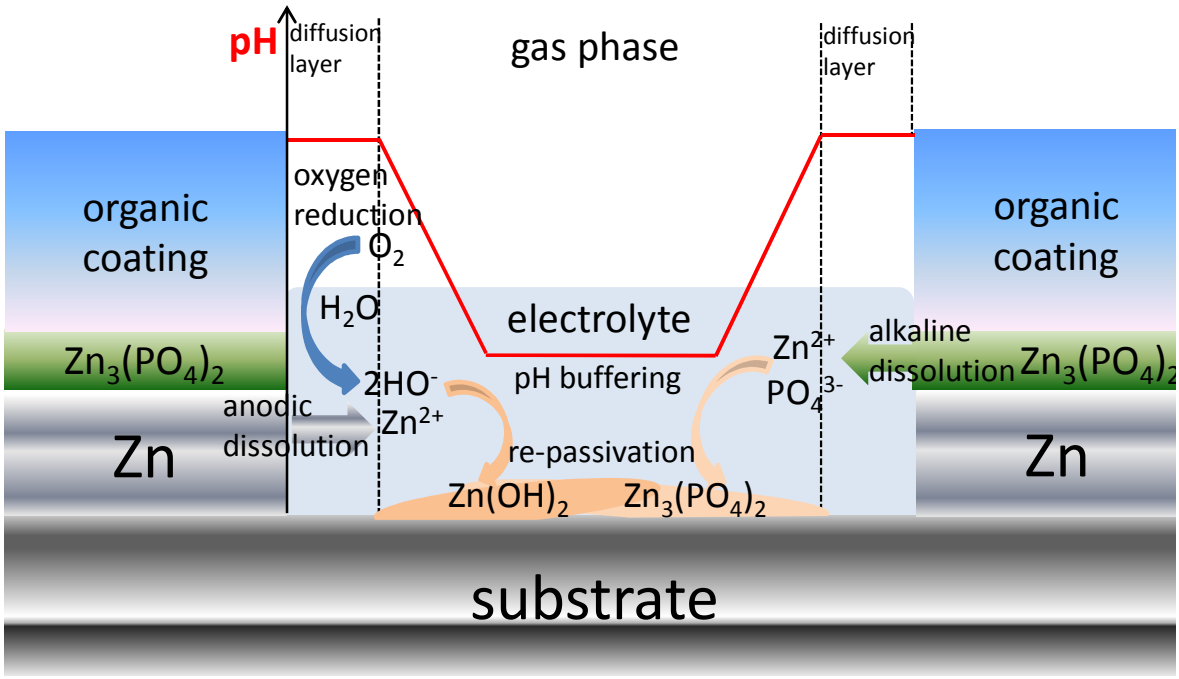

Fig. 4.4.6: Scheme of leaching effect inside an electrolyte-filled defect of a zinc phosphatized and galvanized metallic substrate covered with organic top coating.

In Figure 4.4.6 the cathodic oxygen reduction is restricted to the Nernst diffusion layers at the electrolyte/coating interfaces in order to ease the illustration of the re-deposition of the released zinc(II) cations by diffusion to areas of lower pH. In this way Zn^{2+} can be re-deposited with $PO4^{3-}$ as $Zn_2(PO_4)_3$ or with HO^- as $Zn(OH)_2$. Both processes form insulation layers at the substrate/electrolyte interface while the second one additionally causes a pH buffering.

Thereby the cathodic delamination of a multi-layer system, as illustrated in Figure 4.4.6, can be more strongly inhibited by a less stable anti-corrosion primer, like $Zn_3(PO_4)_2$, than by an inert hybrid-layer, since the latter has no repassivation or pH-buffering properties.

4.4.4 Conclusions

It was revealed by means of electrochemical studies that tri-cationic zinc phosphate layers are not very stable under conditions of cathodic polarization which was used to simulate the effect of oxygen reduction on the stability of anti-corrosion primers. Even though these layers are rapidly alkaline-dissolved, re-deposition of zinc phosphate and precipitation of zinc hydroxide is possible in lower alkaline areas. This effect leads to pH buffering at spots of oxygen reduction as well as repassivation at the metal/electrolyte interface.

In contrast, hybrid-films are much more stable under conditions of cathodic polarization. This is effected by the high alkaline stability of the siloxane matrix and the zirconiumoxyhydroyde matrix.

4.5 Studies of the chemical compositions, morphologies and thicknesses of copper-containing, organosilane-based hybrid-layers on commercial CRS, HDG, ZE and Al6016

After studying hybrid-systems, ones containing additional copper were also investigated. The latter system is a developed version of the first one in which copper nitrate was added to the conversion bath. All other compounds remained unchanged with respect to the composition of the copper-free hybrid-system.

4.5.1 Chemical composition of copper-containing hybrid-layers

Copper-containing hybrid-layers were studied firstly by FT-IRRAS. The collected spectra are illustrated in Figure 4.5.1. According to the FT-IRRAS spectra, which were recorded from measurements on hybrid-layers (see section 4.2), the copper-containing one is mainly characterized by vibrations of the organosilane matrix and the inorganic compounds. The organosilanes are mainly characterized by TO (transverse optical) and LO (longitudinal optical) modes of an asymmetric Si-O-Si stretching vibration which appear at around 1000 cm^{-1} and 1130 cm^{-1} as well as the vibration of the remaining non-condensed Si-OH functions at 930 cm^{-1}. Additionally, two peaks, assigned to the asymmetric and symmetric scissoring mode of $-NH_3^+$, appeared at 1635 cm^{-1} and 1520 cm^{-1}. The inorganic compounds are characterized by intense LO and TO modes of the asymmetric Zr-O-Zr stretching vibration at 690 cm^{-1} and 560 cm^{-1}.

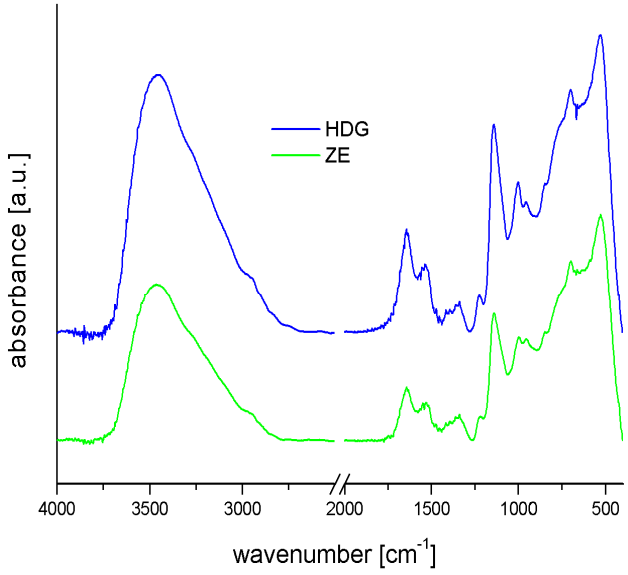

Fig. 4.5.1: FT-IRRAS spectra of copper-containing hybrid-layers on HDG and ZE.

Peaks which can be assigned to copper in the layer matrix would also appear at wavenumbers lower than 1200 cm^{-1} which are thus superimposed by the vibrations of zirconia. Therefore it was only shown by the FT-IRRAS spectra that the film formation of copper-containing hybrid-layers on ZE and HDG occurred and that the peak positions illustrate no significant differences with respect to the chemical composition of copper-free hybrid-layers.

4.5.2 Element distribution in copper-containing hybrid-layers

In order to reveal information on the amount of copper which is embedded in the copper-containing hybrid-layers, XPS measurements were additionally conducted on the same samples previously studied by IR spectroscopy. The recorded XPS survey spectra of copper-containing hybrid-layers deposited on HDG and ZE are illustrated in Figures 4.5.2 and 4.5.3. Moreover, XPS Cu 2p element spectra were collected on both samples and are presented in Figure 4.5.4.

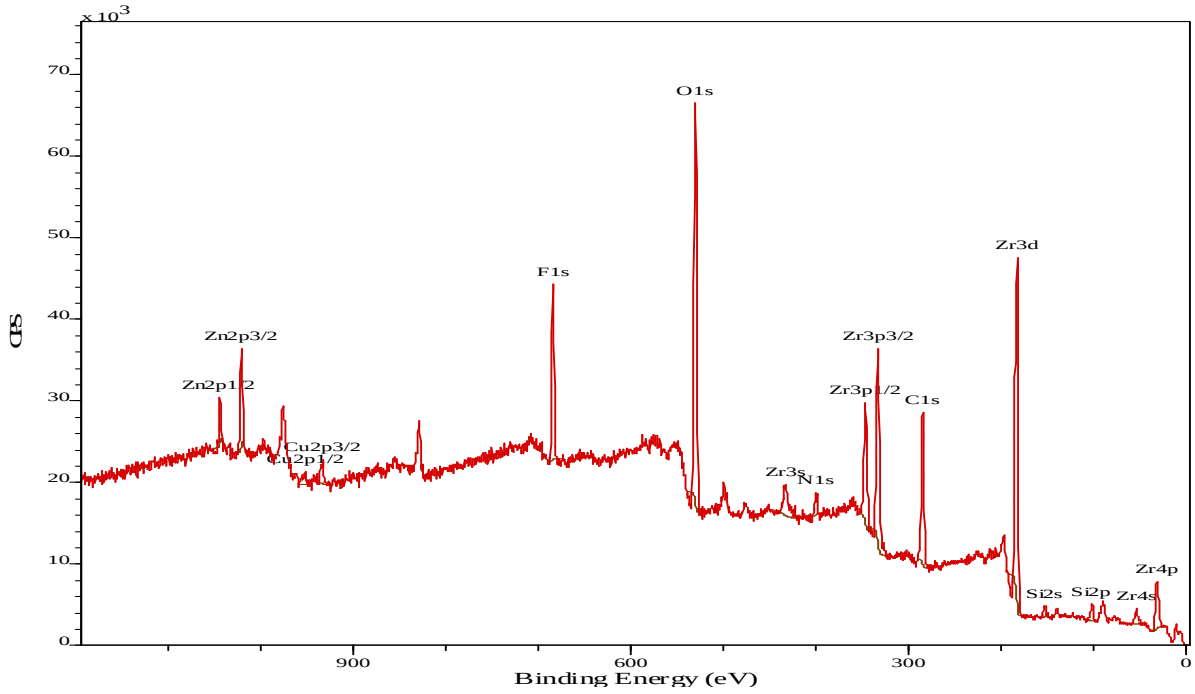

Fig. 4.5.2: XPS survey spectrum of a copper-containing hybrid-layer on HDG.

Both XPS survey spectra are in good agreement with the FT-IRRAS results (see section 4.5.1) and confirm thereby all elements assigned to the organosilane and zirconia-based compounds which were found by means of FT-IR spectroscopy. Additionally, weak peaks assigned to copper appeared in both spectra. Since XPS survey spectra show a limited noise-to-signal ratio, the two most intense

Cu peaks were fitted. These were the Cu $2p_{1/2}$ and Cu $2p_{3/2}$ peaks at binding energies of 953 eV and 933 eV. The collected element distribution for both samples is presented in Table 4.5.1.

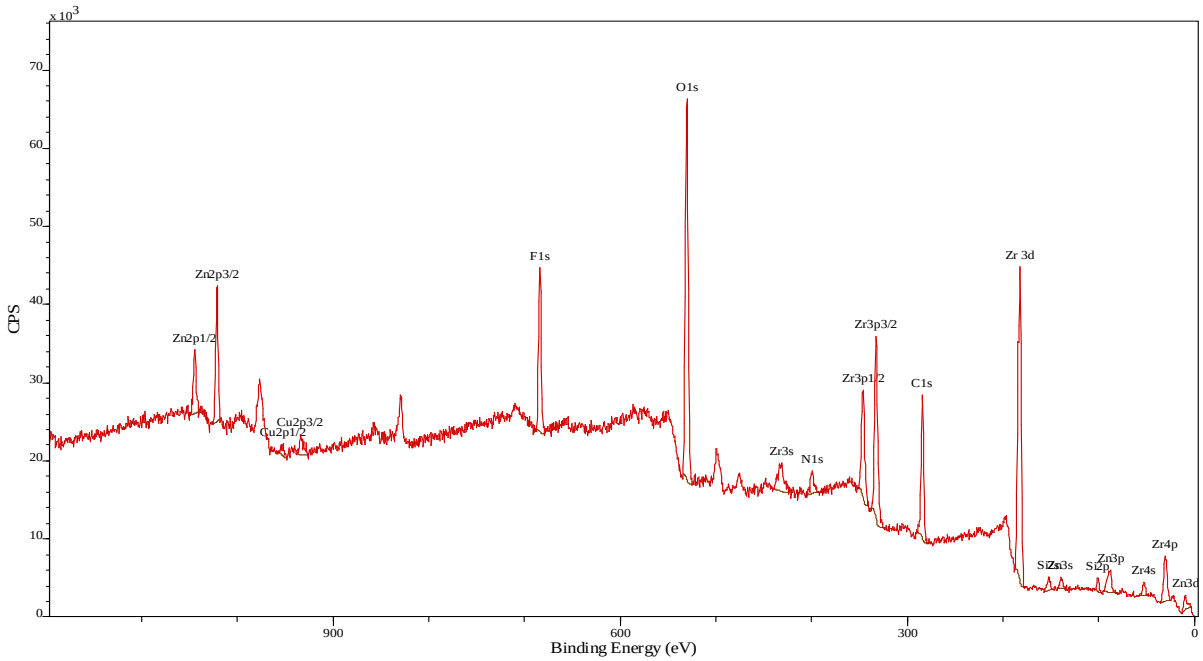

Fig.4.5.3: XPS survey spectrum of a copper-containing hybrid-layer on ZE.

In order to reveal the copper binding states, Cu 2p element spectroscopy was also conducted, the detected element spectra of which are shown in Figures 4.5.4a and b. The Cu 2p peak positions at 952.4 eV and 932.5 eV evidence the presence of elementary copper in the copper-containing hybrid-layers. It is assumed that this derives from reduced copper nitrate: the reduction occurs at the counter-reaction to the anodic metal dissolution at the metal/solution interface. Since the supply of copper is limited by migration from the bulk solution through the NDL to the metal surface, the process of copper reduction causes a depletion of copper near to the interface area. This affects a copper gradient in the deposited copper-containing hybrid-layer, in which the copper concentration is high at the substrate surface and decreases up to the layer surface. This assumption explains the small Cu concentrations of 0.3–0.4 at% which were detected in the upper 2–3 nm of the copper-containing hybrid-films.

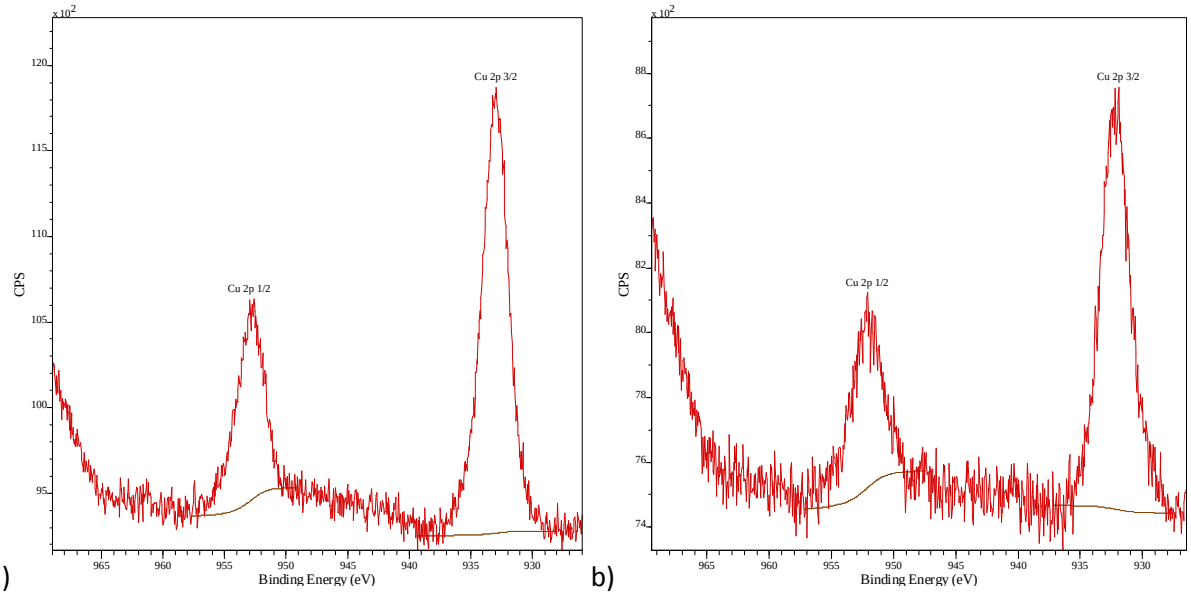

Fig. 4.5.4: XPS Cu 2p element spectra of copper-containing hybrid-layers on a) HDG and b) ZE.

The Si/Zr ratio on the surfaces of these layers was found to vary between 0.4 and 0.6 whereas the ratios on the surfaces of copper-containing hybrid-layers were detected to be around 0.2–0.3 (see Table 4.5.1).

Table 4.5.1: Element distribution from XPS measurements on copper-containing hybrid-layers on HDG and ZE.

element	at%	
	HDG	ZE
C	36.6	35.2
Cu	**0.3**	**0.4**
F	7.6	7.7
N	3.6	4.3
O	31.8	33.2
Si	**4.5**	**3.5**
Zn	1.1	1.4
Zr	**14.5**	**14.3**
Cu/Zr	**0.021**	**0.028**

4.5.3 Layer morphology and film thicknesses of copper-containing hybrid-layers

In order to characterize the surface morphologies of copper-containing hybrid-layers with respect to copper-free ones, FE-SEM images were collected on the HDG and ZE samples. Examples of these images are shown in Figures 4.5.5 and 4.5.6.

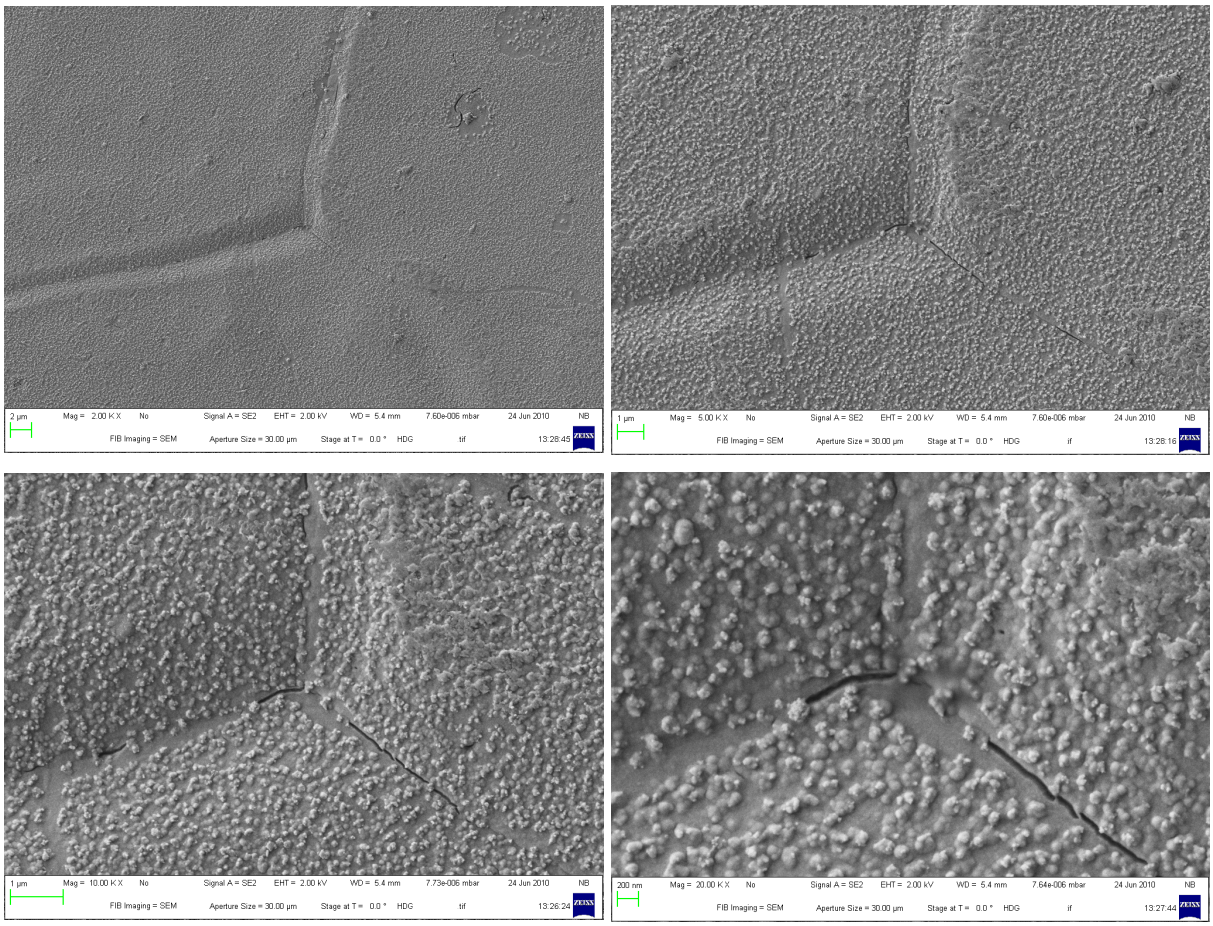

Fig. 4.5.5: FE-SEM images on copper-containing hybrid-layer-coated HDG. Images illustrate the same spot with different magnifications.

Images of the HDG samples reveal that both grains and grain boundaries are well covered by the copper-containing hybrid-film. Additionally, the surface is characterized by particles with diameters even more than 100 nm. These are widely dispersed over the surface and did not appear copper-free hybrid-layers. Due to the much higher zirconium/silicon ratio on copper-containing hybrid-layers with respect to the copper-free ones (as shown by XPS) it can be assumed that these particles consist mainly of zirconium and are embedded into an amorphous matrix which can be assumed to consist mainly of the organosilane.

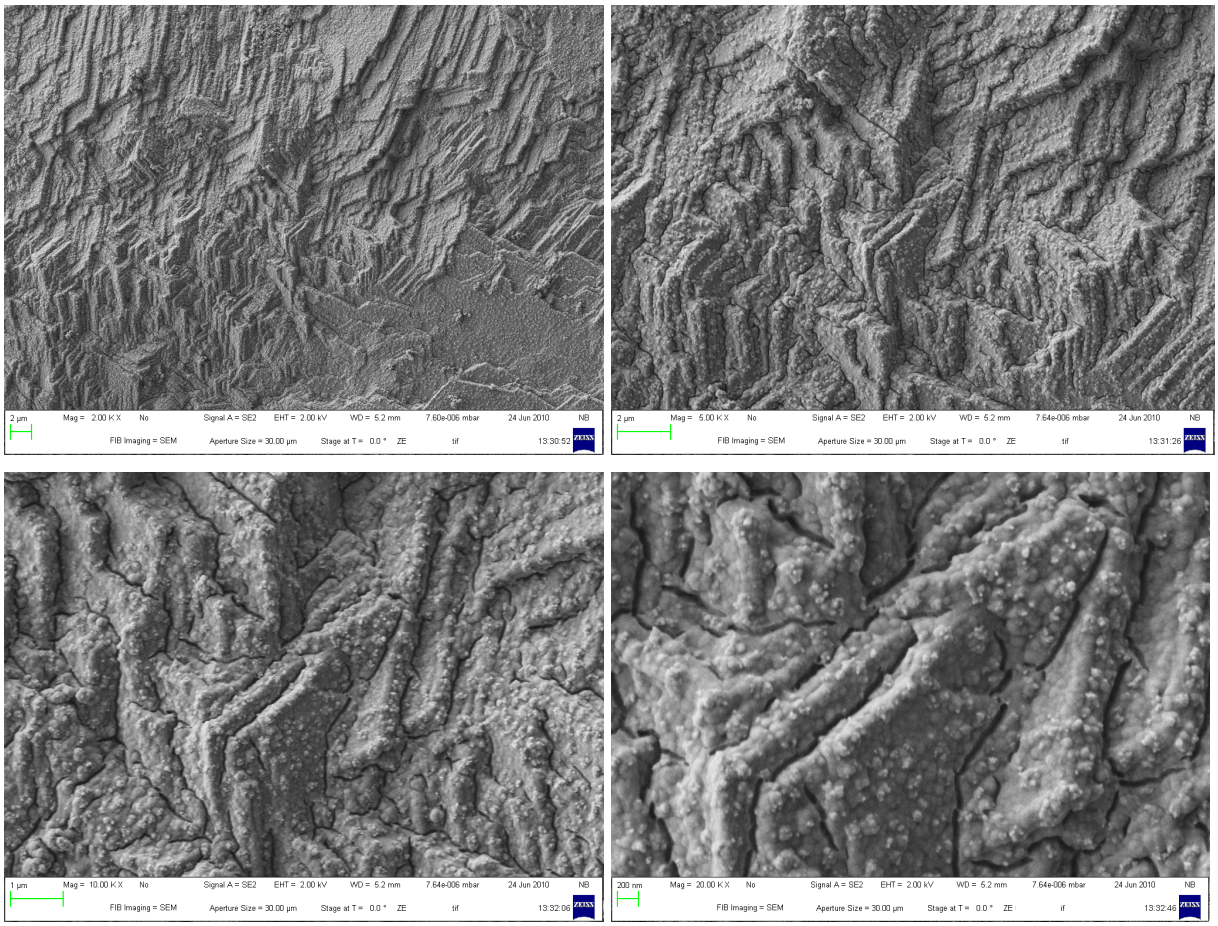

Fig. 4.5.6: FE-SEM images on copper-containing hybrid-layer-coated ZE. Images illustrate the same spot with different magnifications.

The FE-SEM images of copper-containing hybrid-layers on ZE reveal a complete coverage of terraces and edges. As observed on copper-containing hybrid-layer-coated HDG samples, the main characteristic of the morphologies are zirconium-based particles which are embedded into the film matrices.

In describing the layer structure it becomes obvious that the underneath morphologies of terraces and edges are more strongly hidden by the copper-containing hybrid-layer than can be observed in FE-SEM images of copper-free hybrid-layers (see section 4.3.2). Hence it can be concluded that the layer thicknesses of copper-containing hybrid-layers are significantly higher than those of the copper-free ones. This assumption is supported by the fact that several cracks are present at the surfaces which are assumed to be a result of film shrinking during the drying processes. The condition for the appearance of these cracks is a level of stress which is high enough to exceed the limit of elasticity of the layer matrix. Thus cracks can only appear on relatively thick layers (like copper-containing hybrid-layer) but not on very thin ones (like copper-free hybrid-layers).

However, in order to verify the previous assumptions, FE-SEM imaging was additionally conducted on hybrid-layer-coated substrates after cryogenic breaking in liquid nitrogen. Copper-containing hybrid-layers were deposited on ZE, HDG, CRS and Al6016 by 3 min immersion into the copper-containing hybrid-system set to pH 4.2. Samples were subsequently cryogenically broken towards the backside as described earlier for hybrid-layers (see section 4.3.2) and studied by FE-SEM. Examples of the recorded images are presented in Figure 4.5.7 and the recorded film thicknesses in all images are shown in Table 4.5.2.

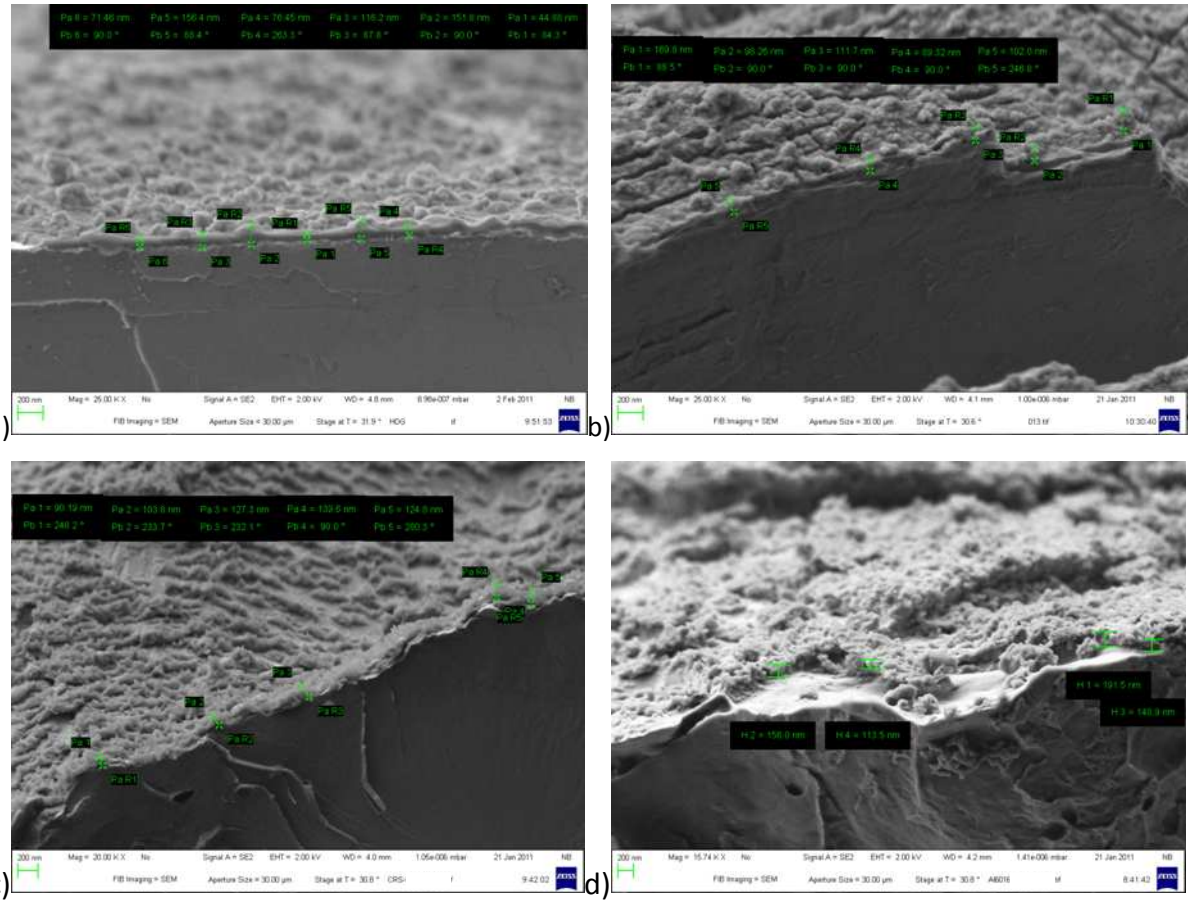

Fig. 4.5.7: Examples of FE-SEM images of copper-containing hybrid-layers applied on a) HDG, b) ZE, c) CRS and d) Al6016 after cryogenic breaking.

Copper-containing hybrid-layers on HDG and CRS showed average film thicknesses of around 110 nm while the results on CRS and Al6016 revealed thicknesses of around 120 nm and 130 nm. From this, two conclusions can be drawn. Firstly, the assumption that copper-containing hybrid-layers are much thicker than the copper-free ones can be confirmed; and secondly, it was shown that the thicknesses of copper-containing hybrid-films depend only a little on the type of coated alloy.

Table 4.5.2: Layer thicknesses of copper-containing hybrid-layers on Al6016, CRS, HDG and ZE.

Layer thickness / nm	Al6016	CRS	HDG	ZE
	156	125	129	171
	114	96	118	101
	192	96	230	112
	149	126	72	100
	134	101	90	199
	177	90	192	90
	159	104	127	81
	159	127	58	117
	102	140	44	103
	104	125	124	170
	91	107	92	98
	135	94	71	112
	110	98	156	89
	95	123	76	102
		124	116	
		99	152	
		94	45	
Average	**134** ± 32	**109** ± 16	**111** ± 51	**118** ± 36

4.5.4 Conclusion

The thicknesses and morphologies of copper-containing hybrid-layers are significantly influenced by the addition of copper nitrate to the hybrid-system. The resulting layer thicknesses of copper-containing hybrid-layer, deposited within the same immersion time, were found to be around twice as high as the copper-free ones. Moreover, the morphologies of copper-containing hybrid-layers are characterized by globular particles which are embedded into the film matrices. Due to the twice-as-high zirconium/silicon ratio on the surfaces of the copper-containing hybrid-layer, in contrast to the copper-free layers, it can be concluded that these particles mainly consist of zirconium. Their appearance is doubtless caused by the copper nitrate in the solutions since the type of all other components as well as their concentrations remained unaffected with respect to the copper-free hybrid-system.

In order to explain the observed results, the electrochemical properties of copper need to be considered. If the film formation processes start by the anodic dissolution of the substrate surfaces, the copper reduction at the metal/NDL interface is assumed to be thermodynamically superior to the hydrogen reduction due to the relatively higher cathodic electrochemical potential of copper than hydrogen.

Thus copper is initially deposited on the substrate surfaces, which can subsequently act as a local electrochemical cell and accelerate both the anodic and cathodic electrochemical processes. The anodic metal dissolution is unlimited whereas the copper deposition is limited by the supply from the bulk solution. Thus the migration of copper nitrate through the NDL is rate-determining for this process and leads to a depletion of copper nitrate near the interfacial area. As a result of this, proton reduction appears mainly as the counter-reaction to the metal dissolution which leads to a stronger pH gradient inside the NDL. In turn, the destabilization and co-aggregation of the bath compounds also accelerates which finally ends in higher film thicknesses as observed by means of FE-SEM. Moreover, the depletion of copper nitrate in the NDL after the initial copper deposition was confirmed by XPS measurements, which results illustrated only small amounts of copper on the surfaces of the copper-containing hybrid-layers. However, the postulated copper gradient inside these layers, which is characterized by a high copper concentration at the metal/layer interface and a low one in the upper layer structures, should additionally be confirmed by XPS sputtering.

Since a stronger pH gradient in the NDL during film formation explains the increased layer thicknesses but not the appearance of the globular particles inside the copper-containing hybrid-layers, another process needs to be considered. Thereby it is assumed that the initially deposited copper on the substrate surfaces not only causes an increased pH gradient but also initiates heterogeneous nucleation of the zirconia-based pre-colloids. Thereby zirconia particles grow up from copper islands on the metal surfaces while they are embedded into the simultaneously deposited organosilane matrix. This assumption explains the high amount of zirconium which was revealed on the copper-containing hybrid-layer surfaces by means of XPS. However, the basis of this hypothesis, which is a particle composition of zirconium, oxygen and fluorine but not of the organosilane, could not be directly confirmed by XPS. Therefore, the single particle compositions should be further investigated by means of high-resolution Auger-spectroscopy.

The revelation of a dependency between the higher layer thicknesses of copper-containing hybrid-systems and the corresponding anti-corrosion properties was discussed in section 4.7.2.

4.6 Studies of the improvement of properties of organosilane-based hybrid-layers by modification of the process parameters

4.6.1 Influence of fluid dynamics on the formation and properties of copper-free and copper-containing hybrid-layers

Copper-free and copper-containing hybrid-layers were deposited on HDG under various flow rates in order to study any dependence between film properties and fluid dynamics during film formation. Furthermore, the coating times were varied between 30 s and 3 min to enable adequate investigation of the film formation process even though the measurements were conducted ex-situ.

As a reference for the influence of fluid dynamics on the hybrid-film-building, the Reynolds number (Re) as illustrated in Eq. 4.6.1 was chosen since it is a useful tool for the evaluation of laminar- or turbulent-dominated flow rates. The Reynolds number describes the ratio of inertial and viscous forces and is defined as

$$Re = \frac{\nu \rho d_{tube}}{\eta} \qquad (4.6.1)$$

(with η as dynamic viscosity (Pas), ρ as the fluid density (kg/m^3) and d_{tube} as the tube diameter (m)). As the transition between a laminar and laminar/turbulent mixed flow is, for aqueous tube flows, determined by a Reynolds number of around 2400, two flow rates below (Re = 500, 2000) and two above (Re = 4000, 10000) this transition state were chosen for the experiments performed. Thereby Re = 4000 characterizes a partly laminar and partly turbulent flow whereas Re = 10000 describes a flow rate which is purely turbulent.

In order to ensure independency of the results from other process parameters than the fluid dynamics all studies were conducted on the same substrate using the same solution in a self-made plug-flow cell which is illustrated in Figure 4.6.1. During the coating time all plugs were flowed through by both hybrid-systems while the flow rates were controlled by a peristaltic pump.

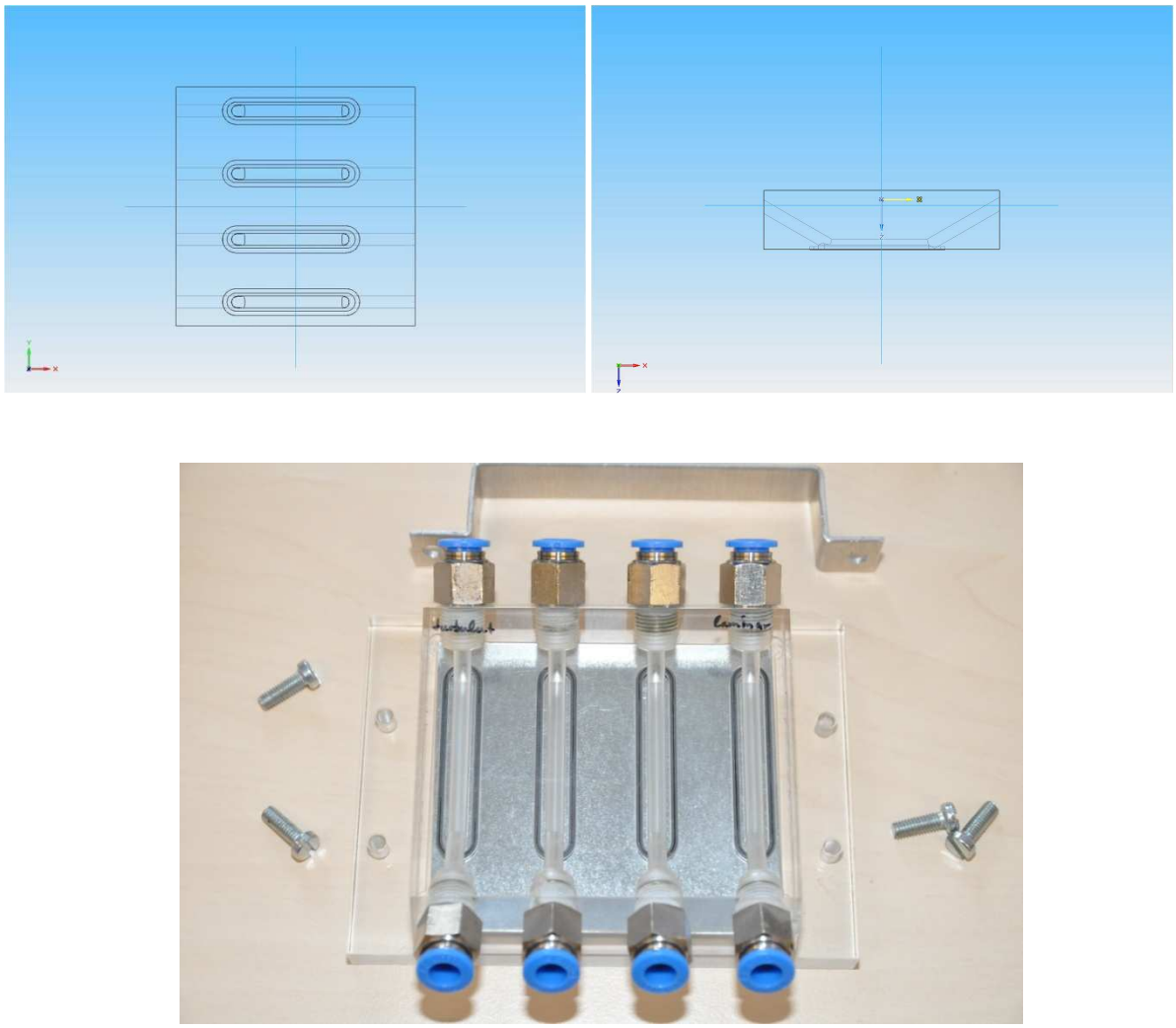

Fig. 4.6.1: Self-made plug flow cell with engineering drawing (top) and picture of the used cell (bottom).

4.6.1.1 Chemical compositions and element distributions in hybrid-layers as a function of the flow-rates

All coated samples were studied by µ-FT-IRRAS in order to reveal any local chemical heterogeneity in the deposited films. As an example of µ-FT-IRRAS results, the spectra of a hybrid-layer deposited on HDG after 3 min immersion time are illustrated in Figure 4.6.2. Three spectra of different spots on each surface were analyzed to ensure comparability of the local chemical film compositions.

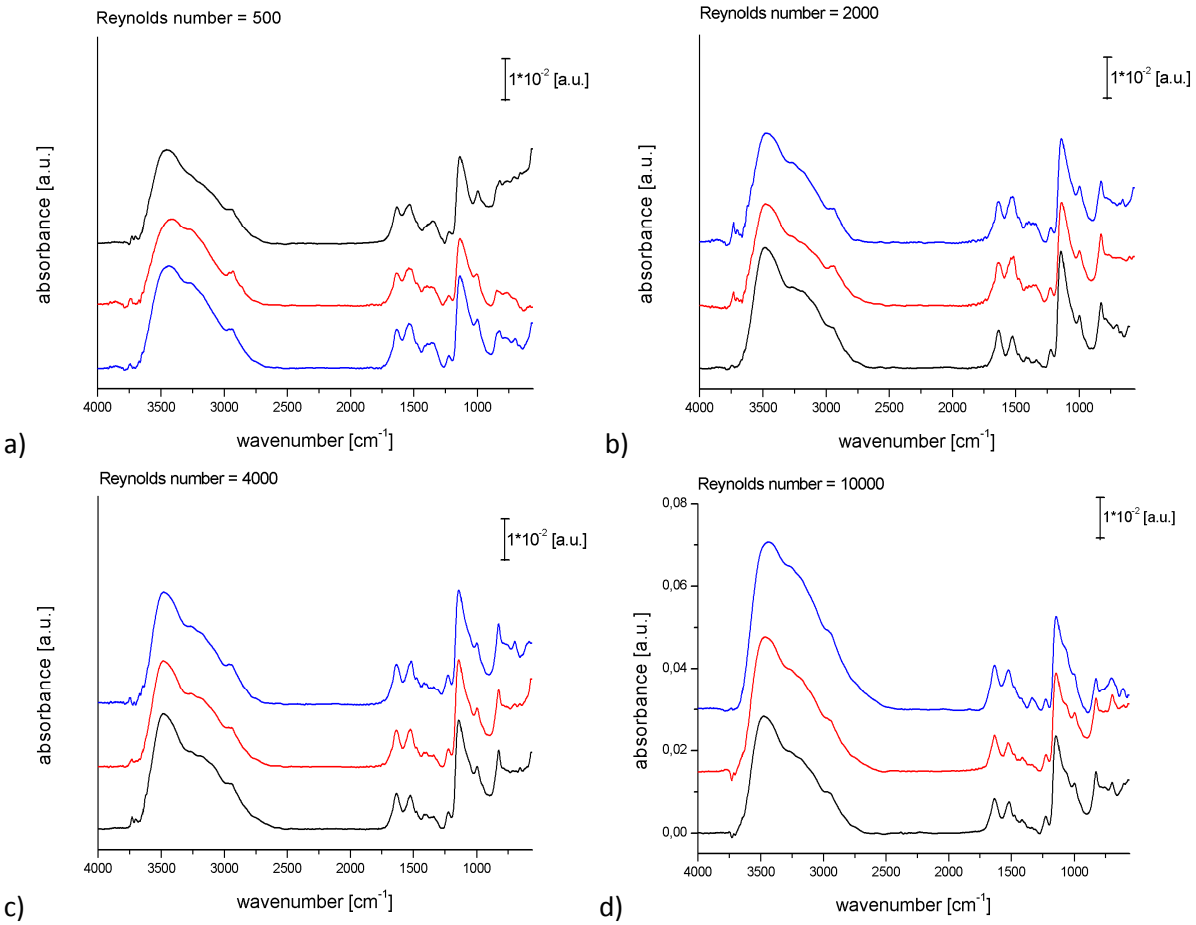

Fig. 4.6.2: µ-FT-IRRAS spectra (different spots with scan areas of 200 µm x 200 µm) on HDG coated with a hybrid-layer for various flow rates; background: alkaline-cleaned bare HDG; a) Re = 500; b) Re = 2000; c) Re = 4000; d) Re = 10000.

However, all µ-FT-IRRAS spectra reveal hybrid-films on the investigated surfaces which are mainly characterized by the LO and TO modes of the asymmetric stretching vibration of the siloxane matrix which appear at 1130 cm^{-1} and 1060 cm^{-1} as well as additional peaks assigned to the zirconia matrix which appear at wavenumbers lower than 1000 cm^{-1}. No change in peak positions and the according peak width at half height were observed but the peak heights varied with respect to the coating times and flow rates.

These results prove that the start of hybrid-film formation and its chemical composition is more or less independent of the fluid dynamics which leads to the conclusion that the flow rates are not a crucial factor for the film formation.

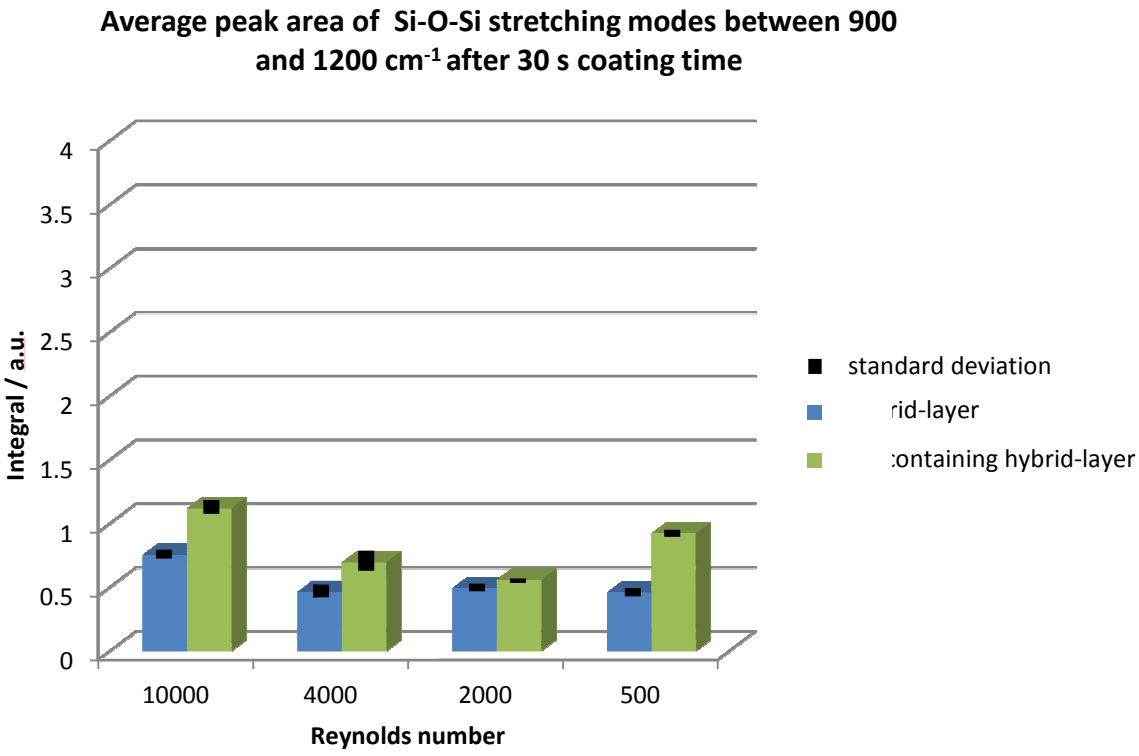

a)

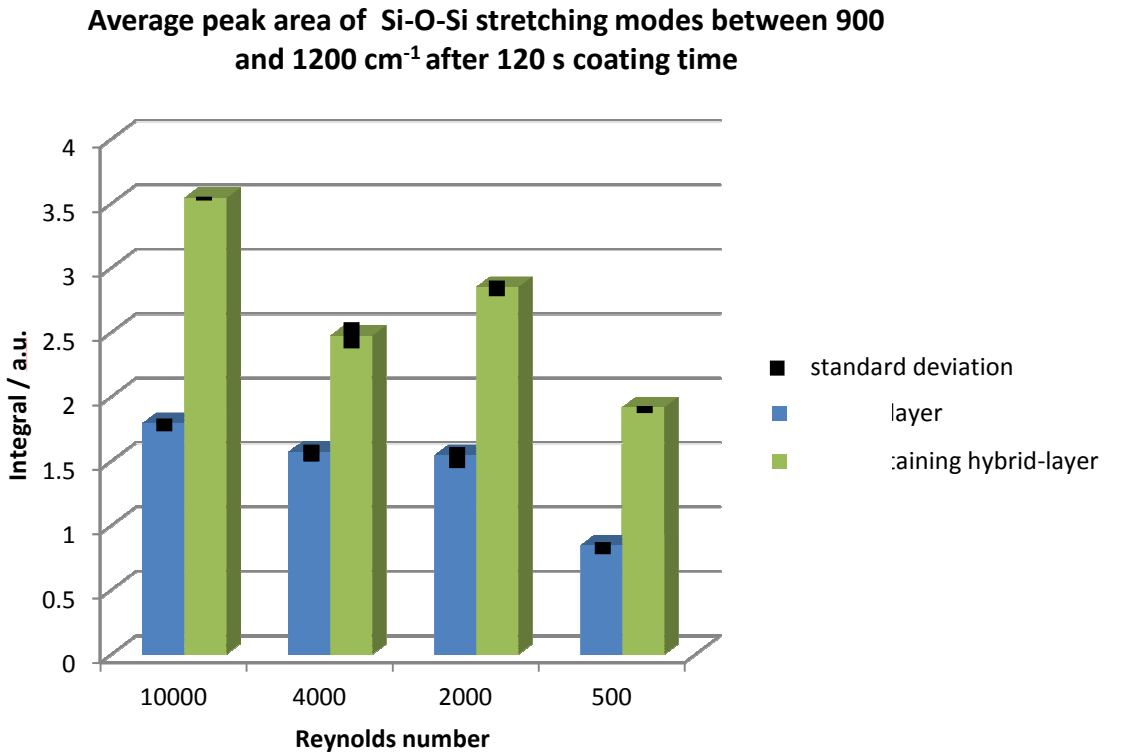

b)

Fig. 4.6.3: Average peak areas of the integrals of Si-O-Si stretching modes at wavenumbers between 900 cm-1 and 1200 cm-1. a) 30 s coating time; b) 120 s coating time.

Regarding the peak heights, one should keep in mind that the rate of film growth is not only influenced by the adsorption kinetics but also by the transport of reactive species to the interface.

Thus it could be supposed that the diffusion-controlled transport through the Nernst diffusion layer, whose thickness depends on the flow rate, is a rate-determined factor for the film formation. In order to verify this assumption, the asymmetric stretching vibrations of the siloxane matrix between 900 cm^{-1} and 1200 cm^{-1} were integrated for both hybrid-layers after 30 s and 120 s coating time. For the auxiliary condition of constant chemical film composition the integral areas would directly correspond to the film thicknesses. The results of integration are shown in Figure 4.6.3.

The integrated peak areas of the asymmetric Si-O-Si stretching vibration of both hybrid-films revealed higher film thicknesses for the copper-containing hybrid-layers than for the copper-free ones independent of the flow rates. Furthermore it became obvious that the film thicknesses after 2 min coating time were much larger than after 30 s coating time, as expected based on the conversion process.

Evaluating the dependency of film formation and fluid dynamics integrals did not show any constant evolution of film thicknesses with the flow rates. Even though the increase of the flow rate seems to cause higher film thicknesses, which could be explained by the accelerated matter transport caused by diminishing of the laminar layer, it could not be clearly confirmed due to the inconsistency of the results obtained for Re = 500.

Furthermore, X-ray photoelectron spectroscopy (XPS) data were collected to enable the evaluation of element distribution in the copper-free hybrid-films. Therefore, as an example, the survey spectrum of HDG coated for 3 min with the hybrid-system under turbulent flow rate set to Re = 10000 is shown in Figure 4.6.4.

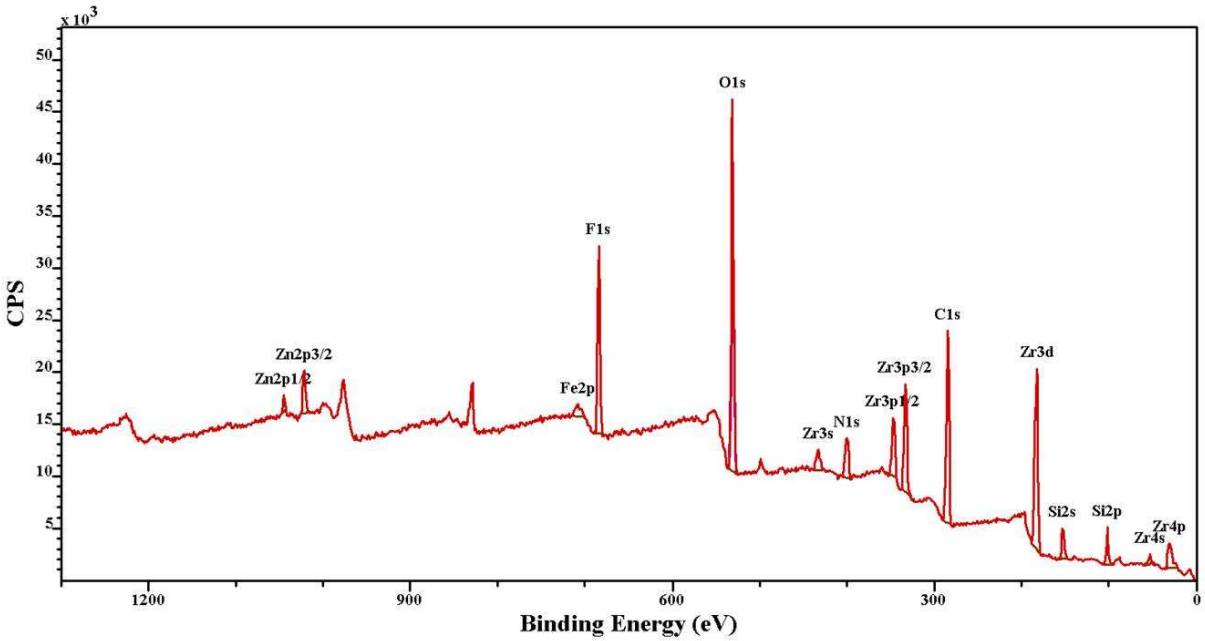

Fig 4.6.4: XPS survey spectrum on HDG coated with the hybrid-system (Re = 10000) and peak assignments.

All XPS peaks were fitted, while the total atomic distribution of all elements is presented in Table 4.6.1, where the fitting results are illustrated dependent on the flow rates during the film formation. The most significant peaks are accorded to the organosilane and Zr-fluoroxyhydroxide within the hybrid-layers which consist of Si and N (siloxane matrix) as well as Zr, O and F (inorganic matrix). What is clear by comparison of the total atomic percentages of these elements is that no dependency between the element distribution and the different flow rates during film formation could be revealed, which is in good agreement with the previous FT-IRRAS results. Hence only small variations in the element distributions occurred due to statistical reasons.

Table 4.6.1: Atomic distribution of elements in hybrid-layers on HDG by XPS.

Element	Atom%			
	Re = 500	Re = 2000	Re = 4000	Re = 10000
C	35.5	36.3	37.7	32.7
O	18.1	16.9	16.1	17.7
Zr	13.8	12.3	12.1	12.3
F	4.6	4.8	5.0	5.3
N	4.5	4.9	4.9	5.5
Si	18.1	16.9	16.1	17.7
Zn	0.1	0.2	0.1	0.2

4.6.1.2 Barrier properties and surface coverage of hybrid-layers as a function of the flow-rates

Since no significant differences in the dependency between fluid dynamics and film formation of either of the hybrid-layers could be revealed by μ-FT-IRRAS, further electrochemical investigations (see Figure 4.6.5) were focused on one series of HDG coated with the copper-free hybrid-system while the coating time was constantly 3 min and the flow rates were varied between Re 500 and 10000.

The electrochemical impedance measurements (EIS) shown in Figure 4.6.5 were conducted for the purpose of the investigation of barrier properties of deposited hybrid-layers. EIS measurements revealed, for all samples, impedances between 10 kOhm cm^2 and 100 kOhm cm^2 but no direct dependency between barrier properties and flow rates during film formation. The large variation of measured impedance values could also be assigned to the additional isolating properties of Al_2O_3 at the hybrid-layer/HDG interface.

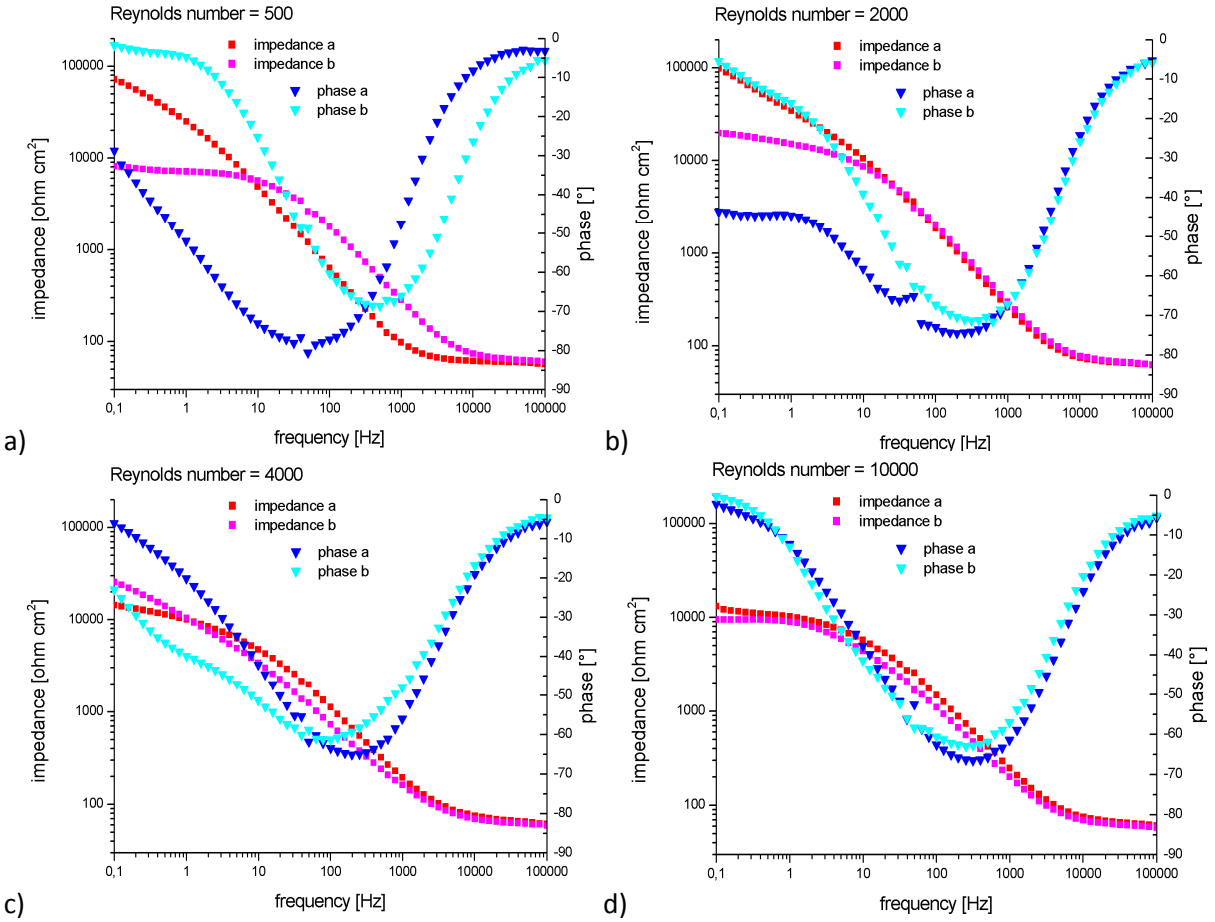

Fig. 4.6.5: Electrochemical impedance spectroscopy on HDG coated with the hybrid-layer at various flow rates. a) Re = 500; b) Re = 2000; c) Re = 4000; d) Re = 10000.

In order to verify this assumption cyclovoltammetry (CV) was additionally conducted on the hybrid-layer since CV analysis can reveal differences in the surface film coverage. To simplify the comparison of all samples, the maximal anodic current densities measured by CV are summarized in Table 4.6.2 whereas the spectra are collected in Figure 4.6.6.

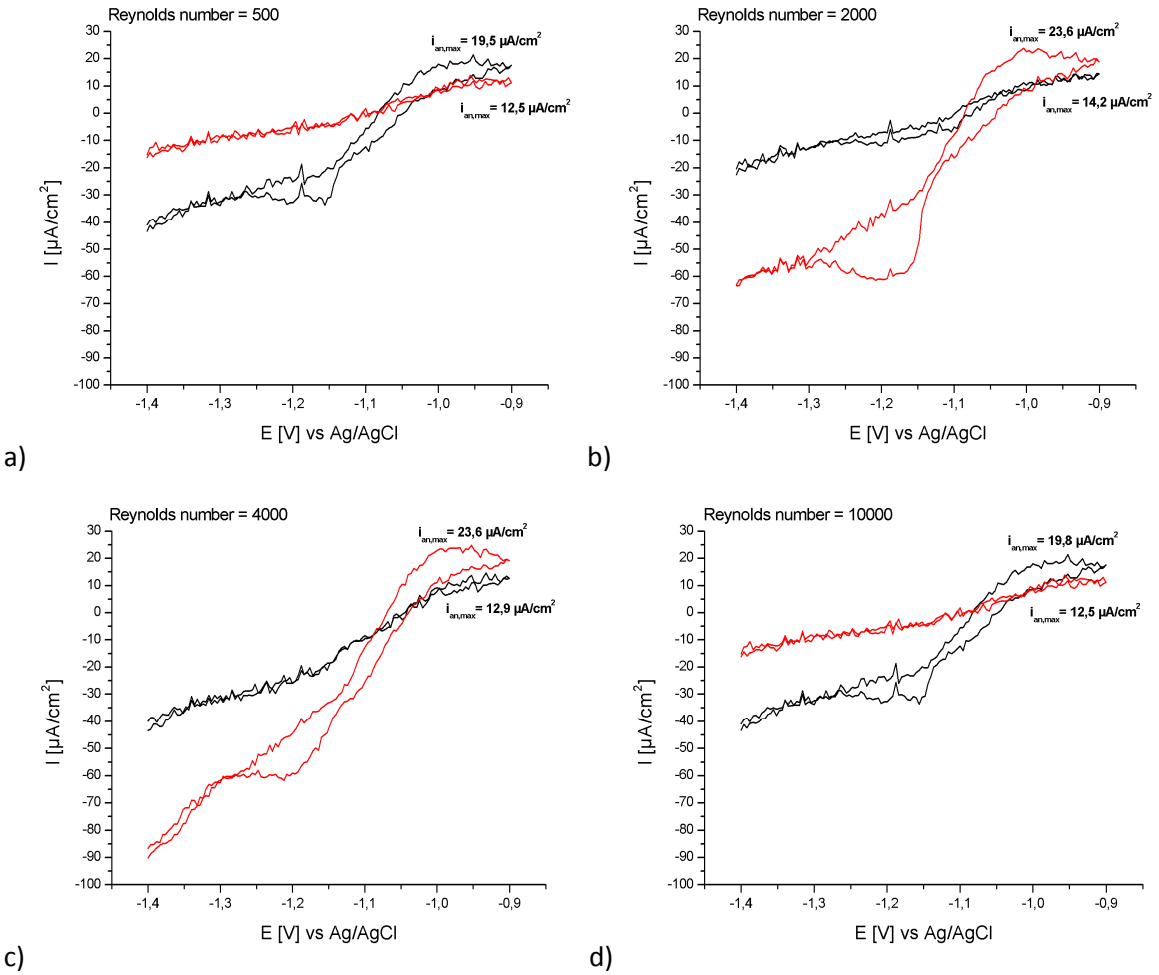

Fig. 4.6.6: Cyclic voltammograms on HDG coated with the hybrid-system at various flow rates. a) Re = 500; b) Re = 2000; c) Re = 4000; d) Re = 10000.

Table 4.6.2: Cyclovoltammetry on HDG coated with the hybrid-system under various flow rates.

Flow rate	**$I_{An,max}$ /(µA/cm²)**		**Ø $I_{An,max}$ /(µA/cm²)**	**degree of surface coverage**
Re = 500	19.5	12.5	16	**97,2%**
Re = 2000	23.6	14.2	18.9	**96,7%**
Re = 4000	23.6	12.9	18.25	**96,8%**
Re = 10000	19.8	12.5	16.15	**97,2%**

reference	**$I_{An,max}$ /(µA/cm²)**		**Ø $I_{An,max}$ /(µA/cm²)**
alkaline cleaned HDG	586.9	567.2	**577.05**

However, the results of cyclovoltammetry are in good agreement with former µ-FT-IRRAS measurements and support the conclusions drawn from EIS since no significant differences of the degree of surface coverage could be revealed. All samples showed a high degree of surface coverage with the hybrid-layer which varied between 96% and 97%.

4.6.1.3 Morphologies of hybrid-layers as a function of the flow-rates

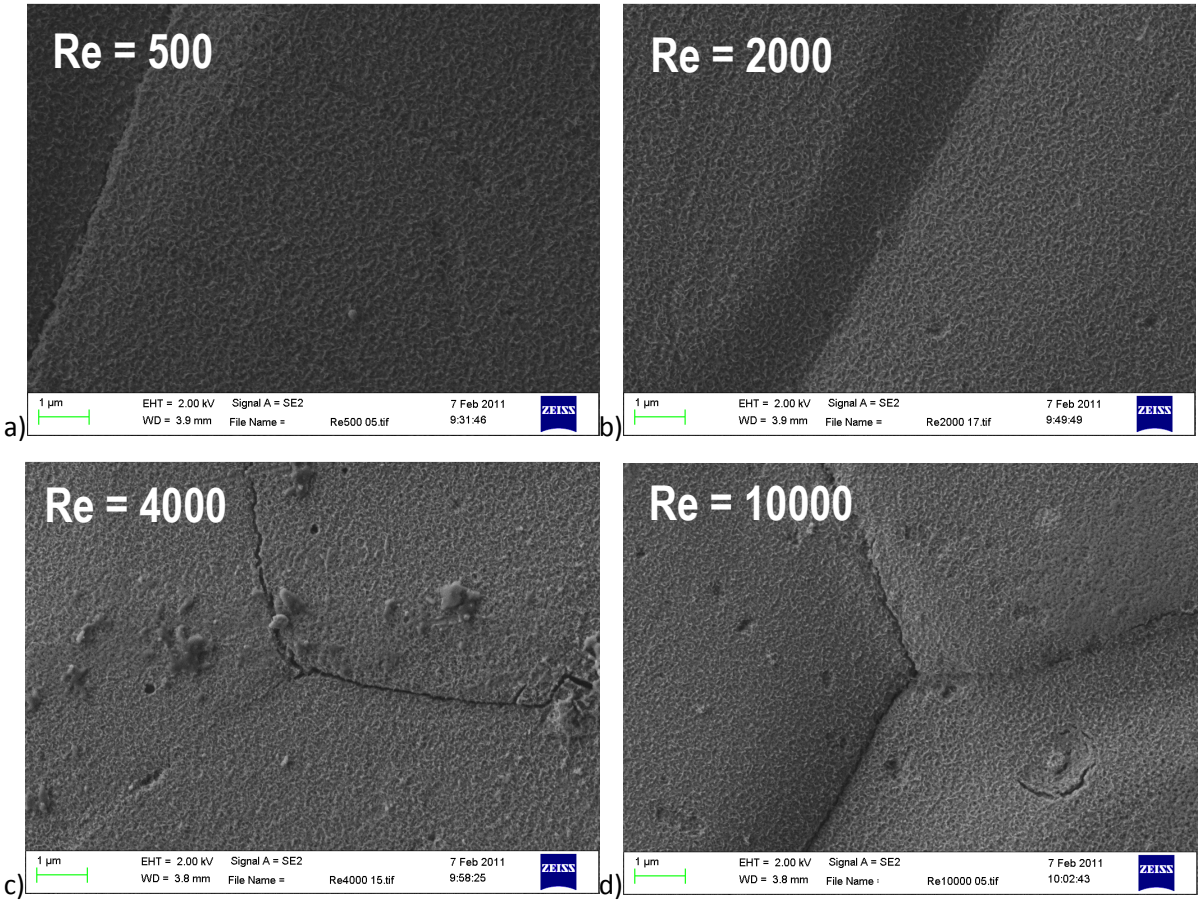

Fig. 4.6.7: FE-SEM images on HDG coated with the hybrid-system under various flow rates a) Re = 500 b) Re = 2000 c) Re = 4000 d) Re = 10000.

Finally, secondary electron microscopy (FE-SEM) images of all samples were taken in order to confirm the results of former measurements and compare the morphology of the hybrid-films dependent on the fluid dynamics during film formation. Examples of SEM images are shown in Figure 4.6.7. In agreement with former studies, the appearance and structure of all hybrid-layers are very similar and characterized by a typical morphology and wide surface coverage on grains and grain boundaries. Thus no interdependency of film morphology and fluid dynamics could be revealed, which was expected with respect to the former analysis.

4.6.2 Influence of bath temperatures on the formation and properties of hybrid-layers

The temperature of the hybrid-system was increased from 20 °C to 40 °C in order to simulate the conditions in the automotive industry where large constructions cause an increase in the conversion bath temperatures due to energy transfer from hot alkaline pretreatment baths. HDG and ZE were coated with the hybrid-system first set to 20 °C and afterwards to 40 °C, the corresponding FT-IRRAS spectra of which are illustrated in Figure 4.6.8.

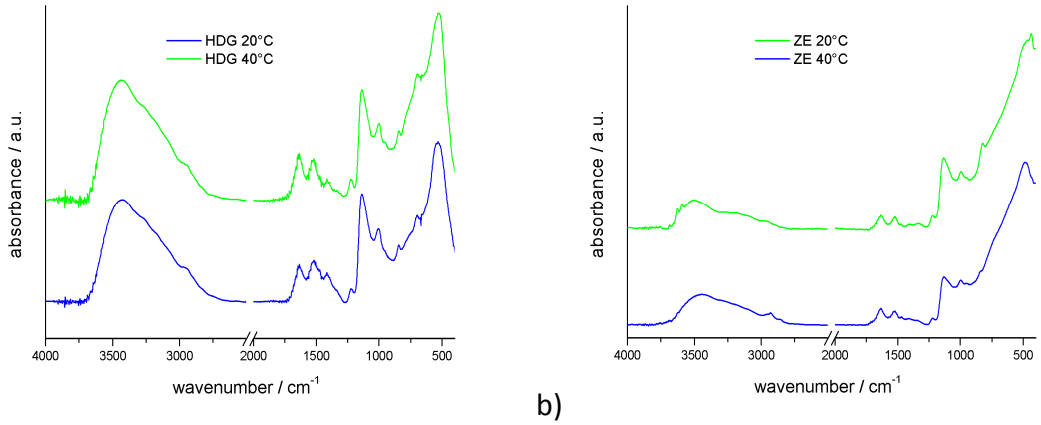

Fig. 4.6.8: FT-IRRAS spectra on hybrid-layers deposited on a) HDG and b) ZE as a function of the bath temperatures.

As shown by the FT-IRRAS spectra, no differences in either system could be revealed, which was expected since an increase of 20 °C can only affect the velocity of the film formation and not the layer chemistry. Thus no peak shifts were detected while also no significant increases of the peak areas could be revealed.

In order to analyze the influence of the bath temperature on the surface coverage and barrier properties of the applied layers, CV and EIS measurements were conducted, which results are presented in Figures. 4.6.9 and 4.6.10. Only layers coated on ZE were studied since previous investigations illustrated that electrochemical studies on HDG lead to controversial results with respect to the insulating native aluminium oxide which partly covers HDG surfaces.

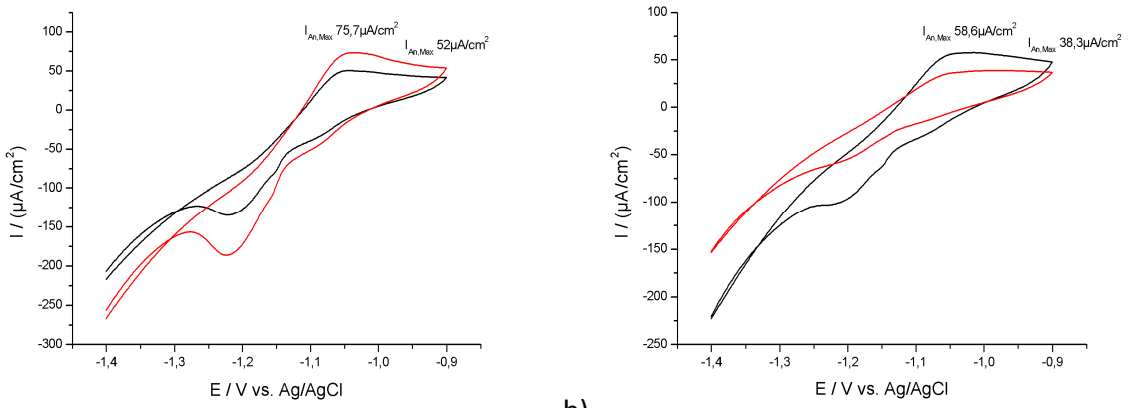

a) b)

Fig. 4.6.9: Cyclic voltammograms of hybrid-layers on ZE deposited from a) 20 °C and b) 40 °C warm hybrid-systems.

Table 4.6.3: Maximum anodic current densities from cyclovoltammetry on ZE coated either in 20 °C or 40 °C warm hybrid-systems.

bath temperature / °C	$i_{an,max}$ / (µA/cm²)		Ø $i_{an,max}$ / (µA/cm²)	degree of surface coverage
20	75.7	52	**63.9**	**90%**
40	58.6	38.3	**48.5**	**93%**

Reference	$i_{an,max}$ / (µA/cm²)
alkaline cleaned ZE	653

From the results obtained from CV measurements, the collected spectra are illustrated in Figure 4.6.9 while the maximum anodic current densities are shown in Table 4.6.3. It was shown that increasing the bath temperature from 20 °C to 40 °C also causes a small increase in the surface coverage from 90% to 93%.

In order to simplify the comparison of the impedances achieved from EIS measurements in Figure 4.6.10, both impedance plots are shown in Figure 4.6.11. In good agreement with the CV results, EIS measurements revealed only slightly higher impedances for the layers deposited from 40 °C baths than those deposited from 20 °C baths.

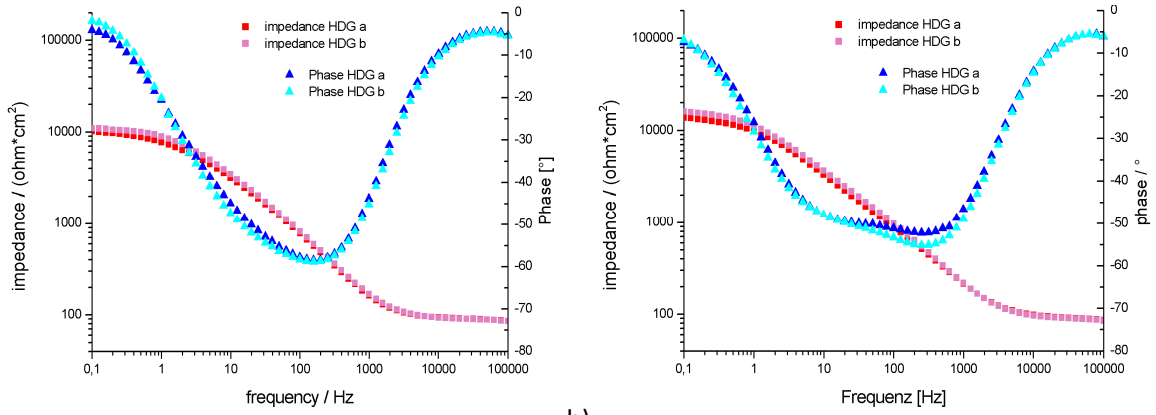

a) b)

Fig. 4.6.10: FT-IRRAS spectra on hybrid-layers on ZE deposited from a) 20 °C and b) 40 °C conversion baths.

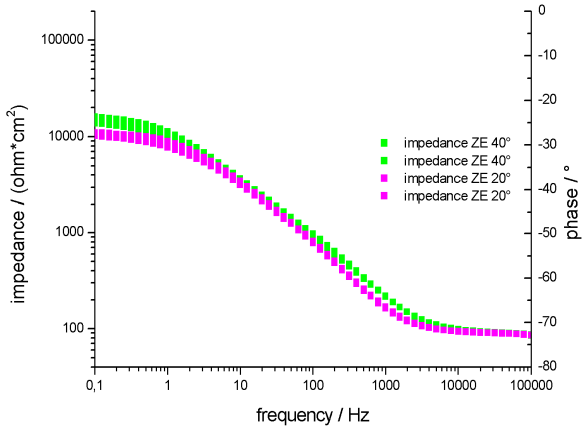

Fig. 4.6.11: Comparison of impedances recorded from hybrid-layers on ZE as a function of the bath temperature.

It can be summarized that slight improvement of the surface coverage and barrier properties can be achieved by increasing the bath temperature which is probably the result of accelerated film growth due to thermodynamic reasons. However, the obtained differences between both systems are so small that it cannot be excluded that these are results of statistical variance.

4.6.3 Influence of step-wise conversion coating and tempering on the properties of hybrid-layers

Since it was proven that hybrid-layers on different substrates reveal a nanoporous structure, the conversion process was changed from 3 min of continuous immersion into the hybrid-system to repeated immersions of 1 min. After each conversion step all samples were rinsed with deionized water. The conversion steps were repeated 3 times for each sample in order to reach the same total conversion time as in the previous studies. The idea was to achieve a higher coverage of the surfaces by step-wise coating with the hybrid-system.

It is known from other conversion processes that pores appear at those spots where the anodic dissolution of the substrate occurs. If the anodic reaction at those spots is stopped, the film formation would probably proceed at the spot area as well. Stopping the anodic reaction was achieved by interrupting the conversion process by pulling the samples out of the conversion bath and rinsing them with deionized water.

4.6.3.1 Barrier properties of hybrid-layers after step-wise coating and part-annealing

Electrochemical impedance and cyclovoltammetry measurements were conducted on samples coated with the hybrid-system by the three-step conversion process as mentioned above. Both studies were compared to samples which were coated by one step with the hybrid-system. As a reference for evaluation of the effect of step-wise coating and tempering on the barrier properties of hybrid-layers “classically” (3 min without any tempering) -coated hybrid-layers applied on HDG and ZE were chosen (see Fig. 4.6.12).

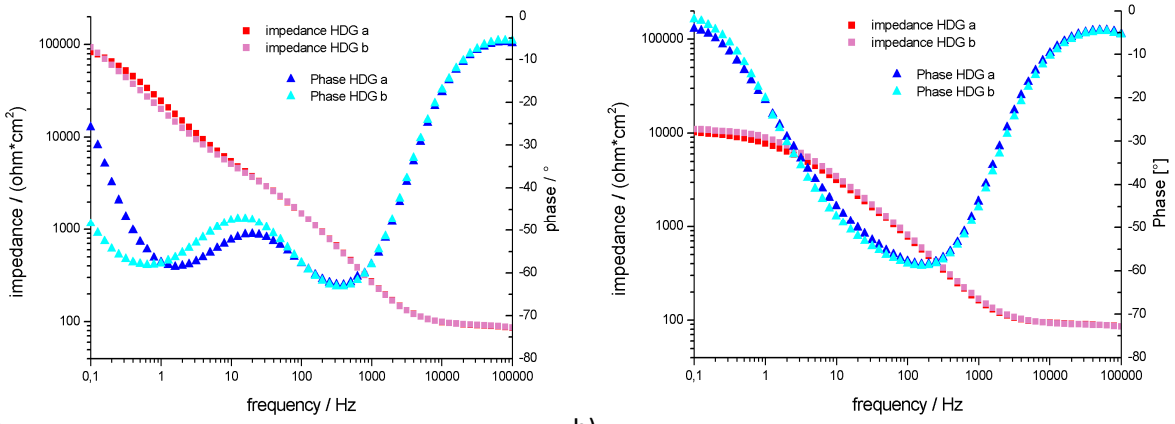

Fig. 4.6.12: Electrochemical impedance spectroscopy on a) HDG and b) ZE coated for 1 x 3 min with the hybrid-system.

The impedance plots of HDG immersed 3 times for 1 min into the hybrid-system are illustrated in Figure 4.6.13 dependent on tempering at 120 °C which was conducted 3 times, each for 10 min, after every immersion step. The corresponding results achieved by EIS measurement on coated ZE are shown in Figure 4.6.14.

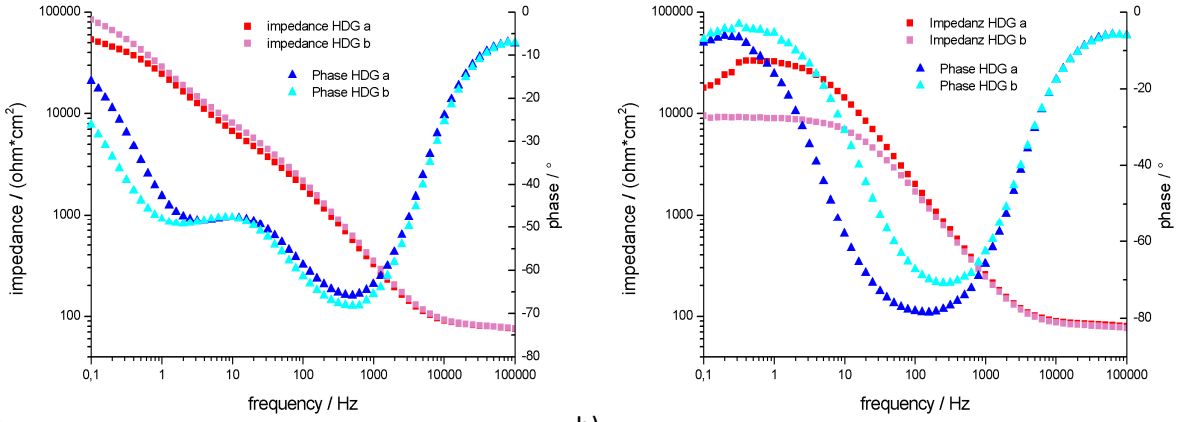

a) b)

Fig. 4.6.13: Electrochemical impedance spectroscopy on HDG coated for 3 x 1 min with the hybrid-system a) untempered b) 3 times tempered for 10 min at 120 °C.

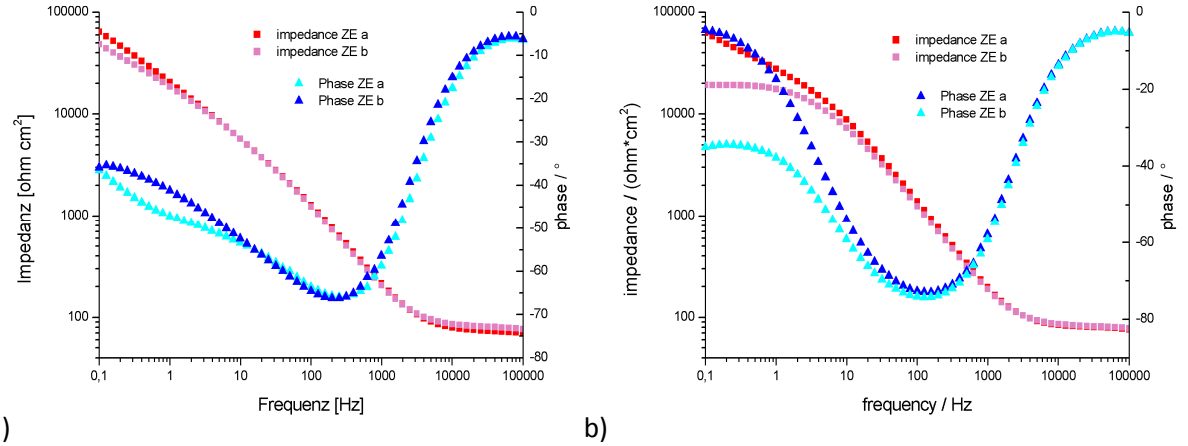

a) b)

Fig. 4.6.14: Electrochemical impedance spectroscopy on ZE coated for 3 x 1 min with the hybrid-system a) untempered b) 3 times tempered for 10 min at 120 °C.

In order to ease the comparison of the obtained results the recorded impedances are illustrated in Figure 4.6.15. EIS plots reveal higher impedances for the 3 x 1 min coated samples at the frequencies assigned to the layer resistance and to the pore resistance (see Figure 4.6.15b). These results showed that changing the process parameters from continuous immersion in the hybrid-system to a step-wise immersion leads to higher barrier properties of the conversion layers as measured by means of EIS.

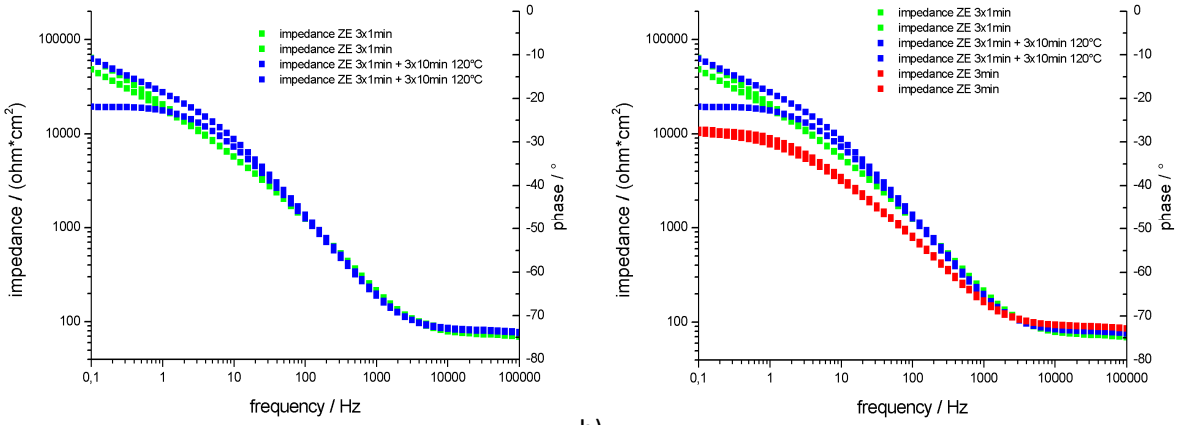

a) b)

Fig. 4.6.15: Comparison of impedances recorded from hybrid-layers on ZE as a function of the coating and the annealing time. a) Impedances after 3 x 1 min coating with the hybrid-system and optional tempering after each coating step (3 x 10 min at 120°C). b) Spectra from a) compared to the impedances recorded on a 1 x 3 min hybrid-system-coated ZE sample.

Focusing on the influence of 10 min annealing at 120°C after each coating during the step-wise conversion process, no significant increase in the barrier properties was achieved in comparison to the non-annealed samples.

Cyclovoltammetry was conducted in order to evaluate the surface coverage of hybrid-system-coated HDG and ZE. Since the measurements were carried out in an oxygen-containing borate buffer only the anodic current densities were significant for the degree of surface coverage. The maximum anodic current densities on HDG and ZE after continuous and step-wise conversion processes are presented in Table 4.6.4. The references which are necessary for calculating the surface coverage are presented below the table containing the current densities measured on bare HDG and ZE.

Table 4.6.4: Maximum anodic current densities from cyclovoltammetry on ZE coated either 3 x 1 min or 1 x 3 min with the hybrid-system.

Sample	substrate	$i_{an,max}$ / µA/cm^2		Ø $i_{an,max}$ / µA/cm^2	degree of surface coverage
continuous coating	HDG	11.5	9.7	**10.6**	**97%**
	ZE	75.7	52	**63.9**	**90%**
3 x 1 min coating	HDG	8.2	7.1	**7.7**	**98%**
	ZE	33	20	**26.5**	**96%**
3 x 1 min coating + 3 x 10 min 120 °C	HDG	0.9	0.7	**0.8**	**~100%**
	ZE	8.5	7.7	**8.1**	**~100%**

Reference	$i_{an,max}$ / µA/cm^2
Alkaline-cleaned HDG	312
Alkaline-cleaned ZE	653

Since the native passive layer on HDG consists of Al_2O_3 which acts as an insulating film, the results of CV on ZE are more significant for the real degree of surface coverage after coating with the hybrid-system. Thus only anodic current densities on ZE will be discussed. The continuously coated ZE showed a surface coverage of around 90%. In contrast, the step-wise conversion process led to coverage of 96% without annealing and +99% after annealing 3 times at 120 °C.

It can be concluded that the higher surface coverage values are in agreement with the higher barrier properties which were revealed by means of impedance measurements. So far, it is not clear why annealing of the samples during the coating process leads to a higher surface coverage (CV measurements) but not to higher barrier properties (according to EIS studies).

However, it was shown by electrochemical studies that changing the coating process from continuous to step-wise conversion leads to increased barrier properties of the films on the investigated alloys.

4.6.3.2 Morphologies of hybrid-layers after step-wise coating and part-annealing

FE-SEM images were collected on ZE and HDG after the three-step coating with the hybrid-system and part-annealing at 120 °C. Figures 4.6.16 and 4.6.17 show examples of HDG and ZE samples prepared without annealing and with annealing three times at 120 °C, respectively.

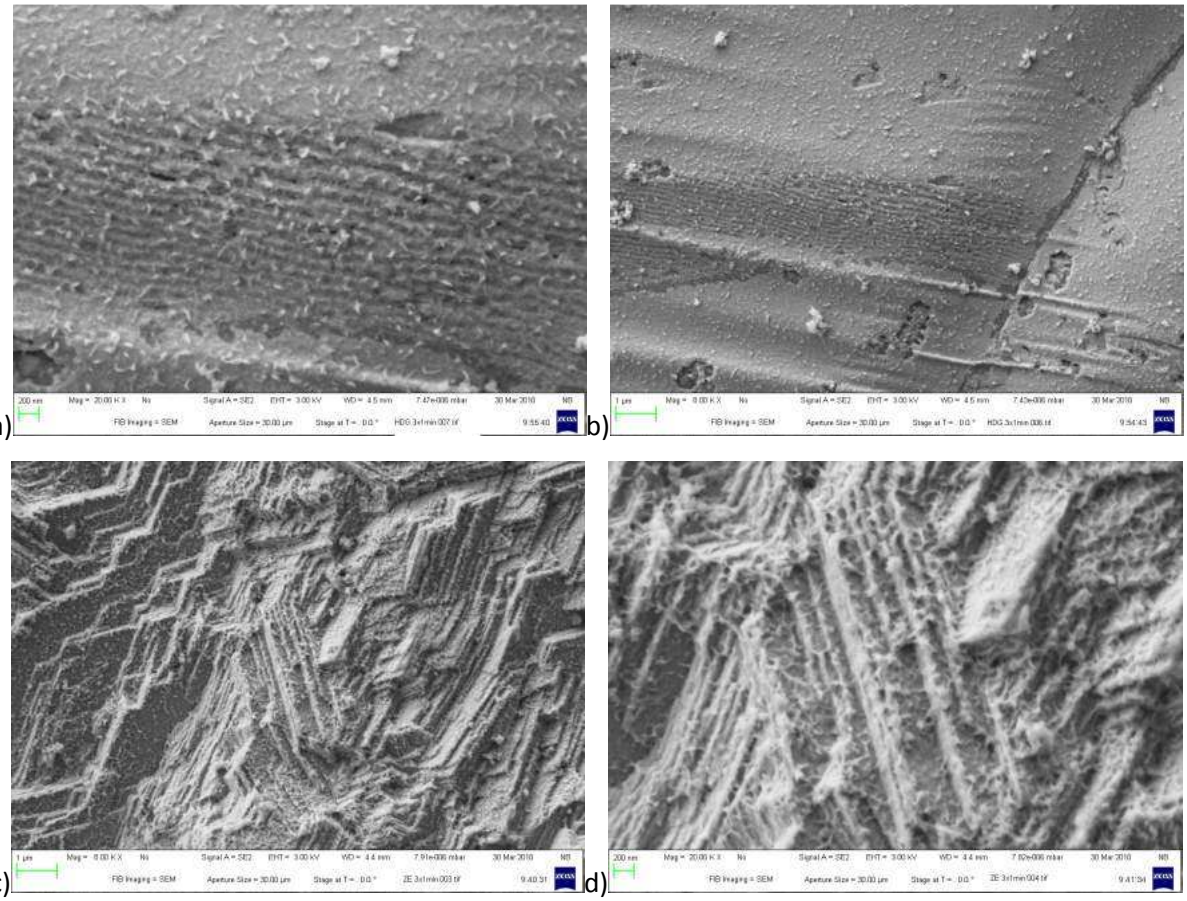

Fig. 4.6.16: FE-SEM images of HDG (a, b) and ZE (c, d) coated with the hybrid-system by step-wise conversion processes.

All images show a quite homogeneous coating of both alloys independent of the annealing. These images are in good agreement with the results of the previously illustrated electrochemical studies. Additionally, nanoscale, crater-like defects in the outer hybrid-layer were observed on HDG samples. The fact that these heterogeneities were still not completely filled after annealing could be an explanation for the unimproved barrier properties which were discussed in section 4.6.2.1.

However, annealing smooth the hybrid-layer on HDG and on ZE. This is due to the spreading of the organosilane polymer on the high energy surface during the annealing process.

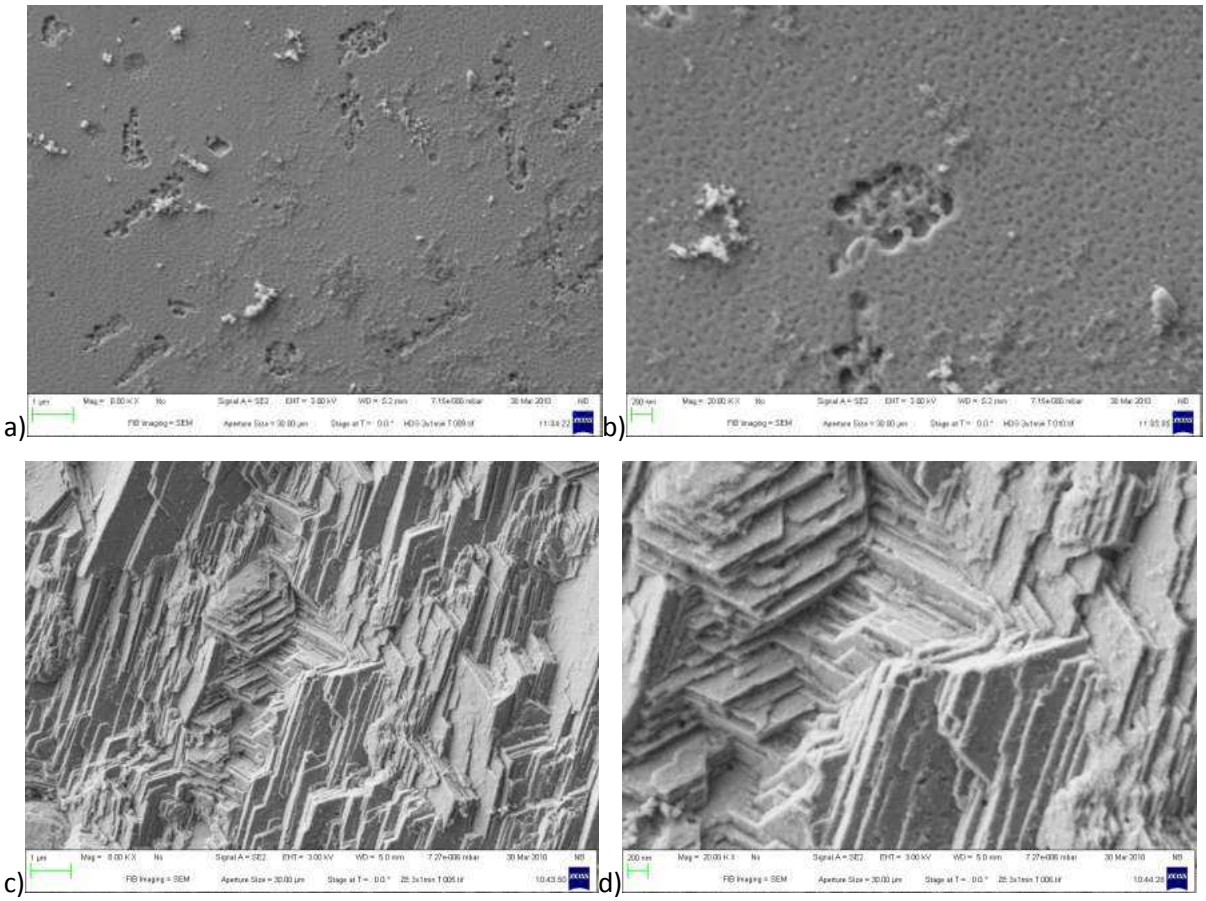

Fig. 4.6.17: FE-SEM images of HDG (a, b)) and ZE (c, d) coated with the hybrid-system by step-wise conversion processes and annealed for 10 min at 120 °C after each conversion step.

Focusing on the ZE images it is obvious that edges and terraces of the ZE surface are largely covered independent of annealing. In agreement with the images of HDG these results confirm the previous electrochemical analysis which revealed a high coverage of the surfaces after step-wise coating with the hybrid-system.

4.6.4 Conclusions

Influence of fluid dynamics on the formation and properties of hybrid-layers

No significant dependences of film morphologies, film compositions or barrier properties of copper-containing and copper-free hybrid-films on the fluid dynamics during the conversion process were revealed.

Influence of bath temperatures on the formation and properties of hybrid-layers

It was shown that increasing the bath temperatures from 20 °C to 40 °C slightly improves the surface coverage and barrier properties of the resulting hybrid-layers. Since these differences are nevertheless very small, no significant statistical improvements can be concluded. Thus it can only be concluded that the increase of the temperatures had no disadvantage to the resulting layer properties.

Influence of step-wise conversion coating and tempering on the properties of hybrid-layers

The reason for changing the parameters of the conversion process from continuous immersion to a three-step conversion process was that usually pores inside the conversion layers appear at those spots where the anodic dissolution of the substrate occurs. If the anodic reaction at those spots was stopped, the film formation would proceed at the spot area as well. This interruption of the anodic reaction was achieved by stopping the conversion process by removing the samples after 1 min of coating from the hybrid-system and rinsing the samples with deionized water. This procedure was repeated three times in order to obtain the same total coating time as the “classic” hybrid-layer-coating process.

EIS measurements on HDG and ZE coated 3 times for 1 min in the hybrid-system showed that changing the process parameters from continuous immersion to step-wise immersion leads to higher barrier properties of the applied conversion layers. Furthermore, a higher degree of surface coverage after the three-step coating process was supported by CV measurements.

Studies on samples which were additionally annealed for 10 min at 120 °C after each conversion step showed nearly 100% coverage of the alloy surface but no significantly higher barrier properties than the non-tempered samples.

FE-SEM images confirmed the results obtained by cyclovoltammetry. They illustrated that grains and grain boundaries of the HDG surface were largely covered by the hybrid-film. This result was also obtained from images of hybrid-films on ZE which showed an adequate coverage of the terraces and edges, which characterizes the ZE morphology. Furthermore, it was observed that annealing leads to smoother films on both alloys which was caused by the spreading of the organosilane on the high energy surface during the annealing process.

4.7 Studies after nanoengineering on organosilane-based hybrid-layers

4.7.1 Post-treatment of organosilane-based hybrid-layers with octadecylthiol (ODT) and octadecylphosphonic acid (ODPA)

In order to enhance the film barrier properties, self-assembling molecules were used for post-treatment of freshly applied hybrid-layers. For the purpose of strong adhesion at the metal surfaces inside of the submicroscopic pores, octadecylthiol (ODT) and octadecylphosphonic acid (ODPA) were chosen.

ODT is known to adsorb on metal surfaces under the formation of a thiol–metal bond which occurs in a two-step process. The first step is a physisorption to the surface and the second one the formation of a chemical bond (R-S-Me) by oxidation of the thiol function which was primarily investigated on pure gold substrates.[149-153,312]

Nevertheless, thiol adoption on commercial alloys was also investigated. Due to the liberation of electrons during the thiol oxidation in the second adsorption step, native oxide films become simultaneously reduced. This leads to chemisorption of the thiol to reduced metal atoms, as known from adsorption on noble substrates. Thus ODT is able to form SAMs on alloy surfaces even though they tend to form brittle native oxide films. SAM formation based on long alkyl chained thiols was already studied on zinc,[313-318] tin,[319] iron,[320,321] nickel,[311-325] and alloys like CuNi[326] or ZnNi.[327]

ODPA was additionally used as a self-assembling molecule since it is well known that organophosphonates adsorb properly to aluminium alloys.[154-158] Thereby X-R-PO_3^{2-} form stable and highly organized monolayers on aluminium oxide, where the hydroxyl-terminated surfaces promote the organophosphonate adsorption by acid–base interactions.[328,329] It was shown by Adolphi et al. that the organophosphonate adsorption leads to bidentate complexation in the case of oxide covered aluminium and tantalum surfaces but to the formation of tridentates on titanium oxide.[330]

However, with respect to post-treatments on multi-metal constructions, not only were both SAM systems used separately, but also a 50%/50% mixture of ODT and ODPA.

4.7.1.1 Adsorption of ODT and ODPA on hybrid-layers

In order to reveal whether ODT and ODPA can be adsorbed on HDG previously coated with the hybrid-system, FT-IRRAS measurements were conducted. The achieved results are illustrated in Figure 4.7.1. The blue spectra correspond in both graphics to the pure hybrid-layer and the green spectra correspond to the different spectrum of either ODPA (Fig. 4.7.1a) or ODT (Fig. 4.7.1b) adsorbed to the hybrid base coating.

Very characteristic of both ODT and ODPA, in FT-IRRAS spectra are the symmetric and asymmetric stretching modes of the octadecyl-group which appear in both spectra between 2800 cm^{-1} and 2900 cm^{-1}. Since these peaks are more intensive in the ODPA spectrum than in the ODT spectrum, it can be concluded that ODPA adsorbs in larger amounts on the hybrid-system pretreated HDG than ODT.

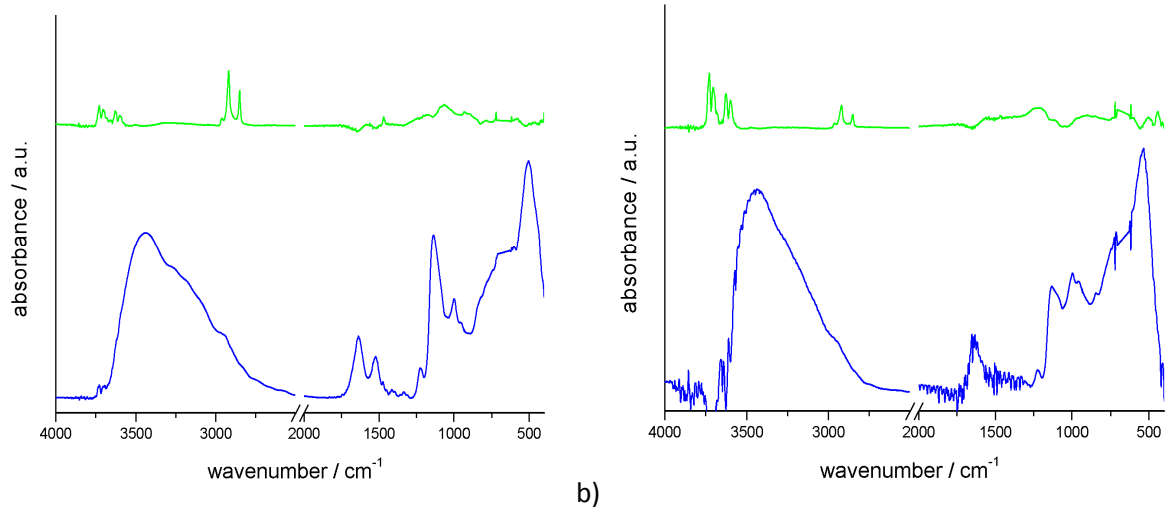

a) b)

Fig. 4.7.1: FT-IRRAS spectra on hybrid-layers on HDG post-treated with a) ODPA and b) ODT. Blue graphs: spectra of the hybrid-layers; green graphs: spectra of the post-treatment.

In order to confirm these spectroscopic results, contact angle measurements were conducted on HDG with a hybrid-layer and post-treatment with either ODPA or ODT or a 50%/50% mixture of both compounds. The average contact angles of multiple measurements are presented below.

			contact angle
HDG + hybrid-layer + ODPA		Ø	**138°**
HDG + hybrid-layer + ODT		Ø	**61°**
HDG + hybrid-layer + ODT/ODPA	50%/50%	Ø	**110°**

Since the hybrid-layer post-treated with ODPA reveals the highest average contact angle, the conclusion drawn from FT-IRRAS spectra that ODPA adsorbs in larger amounts on hybrid-layer-covered HDG than ODT was confirmed.

4.7.1.2 Barrier properties of hybrid-layers after post-treatment with ODT and ODPA

Electrochemical impedance measurements were conducted on HDG coated with the hybrid-layer and post-treated with either pure ODPA, pure ODT or a 50%/50% mixture of both in order to complement the FT-IRRAS and contact angle studies discussed above. In order to simplify the comparison of different EIS measurements all impedances and their corresponding phases are illustrated together in Figure 4.7.2.

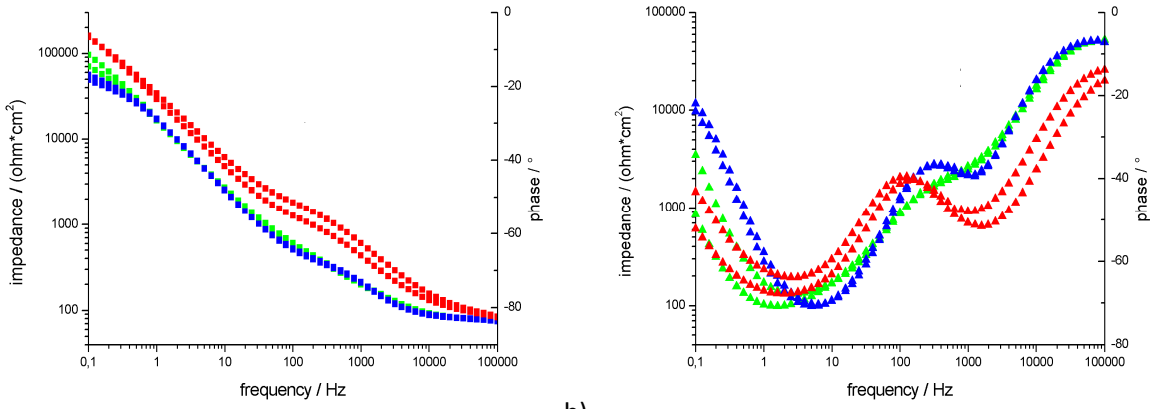

Fig. 4.7.2: EIS measurements on HDG coated with the hybrid-layer and post-treated with different compositions of octadecylphosphonic acid (ODPA) and octadeylthiol (ODT) (green graphs: hybrid-layer post-treated with ODT; red graphs: hybrid-layer post-treated with ODPA; blue graphs: hybrid-layer post-treated with 50/50 mixture of ODT/ODPA). a) Comparison of the impedances b) comparison of the phases.

The results of impedance measurements are in agreement with the previous studies that post-treatment of hybrid-layer-coated HDG with ODPA leads to films which show higher barrier properties than samples post-treatment with ODT or without any post-treatment. This result is reflected in significantly higher impedance values in both areas, that which is assigned to the film resistance and that which illustrates the pore resistance. In Figure 4.7.3 these results are compared to hybrid-layers without any post-treatment.

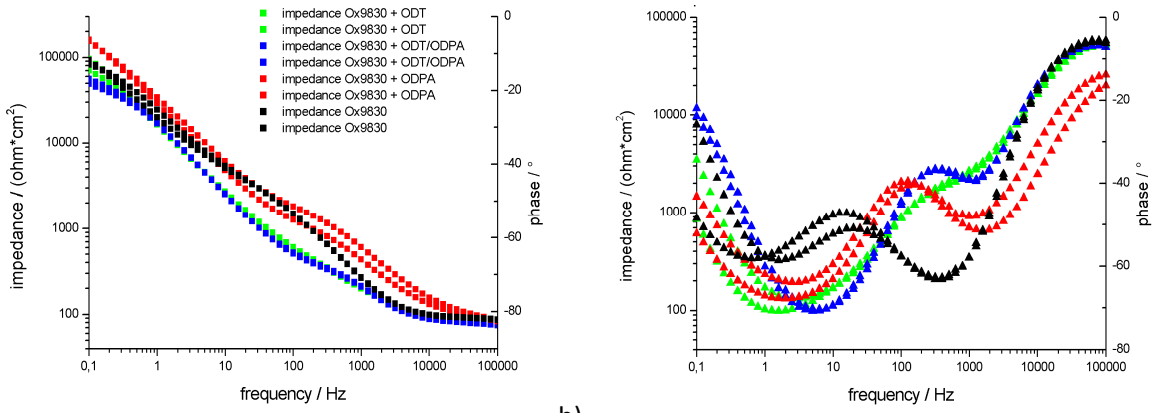

Fig. 4.7.3: EIS measurements on HDG coated with the hybrid-layer and post-treated with different compositions of octadecylphosphonic acid (ODPA) and octadecylthiol (ODT) as shown in fig. 4.7.2 compared to the non-post-treated hybrid-system (black graph) . a) Comparison of the impedances b) comparison of the phases.

Comparison of the impedances of hybrid-layer-coated HDG with and without ODPA or ODT post-treatment revealed that using only ODPA results in higher barrier properties which is in good agreement with the previous studies.

4.7.2 Conclusions

Post-treatment of hybrid-layers with octadecylthiol (ODT) and octadecylphosphonic acid (ODPA)

Since it is known that octadecylthiol (ODT) and octadecylphosphic acid (ODPA) adsorb on zinc oxide and form monolayers on the zinc oxide surface, both compounds were also used in order to block the submicroscopic surfaces inside of nanopores in the hybrid-layers. Therefore the hybrid-layers were post-treated with either ODT or ODPA or a 50%/50% mixture of both.

FT-IRRAS and contact angle measurements were conducted on hybrid-layer-coated HDG and revealed that ODPA adsorbs better on the base hybrid-layer than ODT. This result was confirmed by electrochemical impedance measurements which illustrated higher film and poreresistances for post-treatment with ODPA in comparison to ODT. Comparison of the impedances of hybrid-layer-coated HDG with and without ODPA or ODT post-treatment revealed that using only ODPA results in higher barrier properties.

4.8 Modification of organosilane-based hybrid-layers by incorporation of corrosion inhibitors

New options needed to be found with respect to the enhancement of the stability and anti-corrosion properties of organosilane-based hybrid-layers. Thereby, the focus was set on additives which enhance the buffering capacitance of the layers as well as the barrier properties at the metal/electrolyte interface during oxygen corrosion.

For the latter property strong adhesion on the metallic surfaces needs to be obtained which can be achieved by electron transfer from the adsorbate to unoccupied bands of the solid, which are usually low-energy d-electron orbitals. This leads to strong chemisorption between the substrate and the adhesive.[331,332] In order to arrange such a transfer of electron density the adsorbate needs to contain either atoms with a single pair of electrons or π-electrons. The higher the polarizability of the heteroatom, the stronger is the resulting adsorption as described by the principle of soft and hard acids and bases (SHAB). Hence molecules with either heteroatoms, like nitrogen, phosphor and sulfur, or with aromatics, illustrate strong adhesion properties.

Therefore nanocontainers which contain 2-(methylthio)benzothiazole (MTBT) embedded between silicon clays in poly(dimethylamino)ethyl methacrylate (PDMAEMA) were used since this component contains both sulfur heteroatoms and aromatic rings.

The second nanocontainers which were incorporated into the matrices of the hybrid-layers were magnesium-layered double hydroxide vanadate (Mg-LDH-VO_3) which works as an anionic ion exchange pigment. Vanadates were used since they are known to inhibit both anodic and cathodic reactions during corrosive processes.[333,334] It was revealed that the cathodic reaction is limited by adsorption of the vanadium species at the metal surfaces. The second benefit of these ion exchange pigments is that the vanadates are substituted by halides during the corrosion process. This effect decreases the concentration of the corrosive electrolyte inside the porous matrix which buffers the corrosiveness near to the metal/environment interfaces.

Both corrosion inhibitors were incorporated into hybrid-layers by co-deposition during the film formation process. The hybrid-systems were firstly composed according to the direction for unmodified hybrid-systems and set to pH 4.2 by the addition of Na_2CO_3. Subsequently 0.5 g/l of the corrosion inhibitors (loaded nanopigments) were added and the solutions were strongly stirred for

one hour which resulted in a turbid solution since the corrosion inhibitors are insoluble in aqueous solution with a moderate pH. Film formation was afterwards achieved by 3 min of immersion of HDG and ZE into the modified hybrid-system. The freshly applied films were then rinsed with water and dried in a nitrogen stream.

4.8.1 Chemical characterization of corrosion inhibitors in hybrid-layers

The corrosion inhibitors were firstly characterized by ATR-IR spectroscopy to later enable the identification of the incorporated inhibitors in the hybrid-films. The obtained spectra of Mg-LDH-VO_3 and PDMAEMA/MTBT are shown in Figures 4.8.1a and b.

The Mg-LDH-VO_3 spectrum is dominated by the hydroxyl vibrations around 1600 cm^{-1} and 3300 cm^{-1} and a strong absorbance peak at wavenumbers lower than 1000 cm^{-1}, which can be assigned to the vibration of arbitrarily coordinated inorganic ions, which are manganese, zinc and vanadium in this case. However, one sharp peak appeared at 440 cm^{-1} (indicated by the orange ellipse) which is characteristic for these pigments and unknown for the hybrid-layers, and can therefore be identified as a marker for Mg-LDH-VO_3 pigments incorporated into the hybrid-layer matrices.

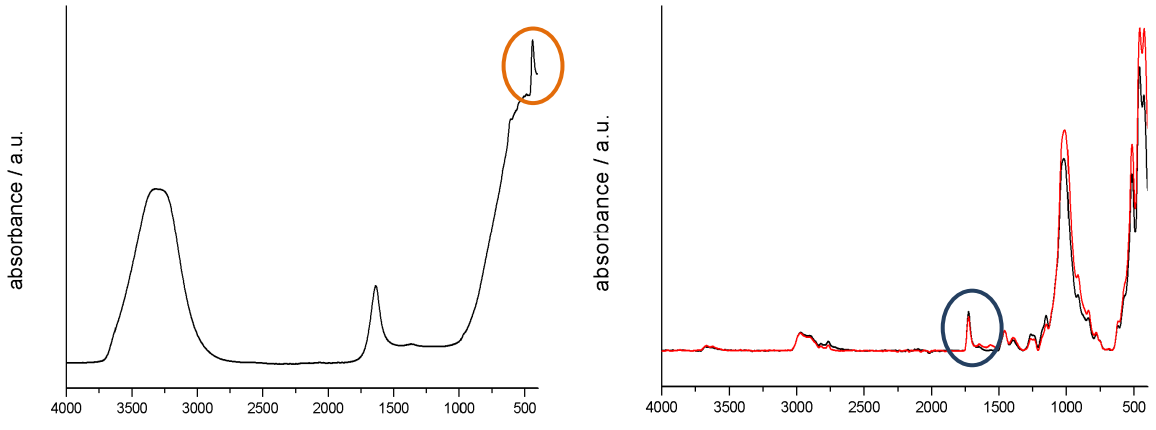

Fig. 4.8.1: ATR-IR spectra of a) MG-LDH-VO_3 pigments and b) PDMAEMA nanocontainers with 0.3% MTBT (black graph) and 0.5% MTBT (red graph).

The IRRAS spectra in Figure 4.9.1b were collected from nanocontainers made of silica clays and MTBT encapsulated into PDMAEMA. The black spectrum is assigned to nanocontainers with 0.3 wt% MTBT whereas the red one records those with 0.5 wt% MTBT. Both spectra show several peaks of vibrations of the organic and inorganic compounds where the carbonyl stretching vibration of acrylic acid ester at 1720 cm^{-1} (indicated by the blue ellipse) can also be used as a marker for nanocontainers inside the hybrid-layer-matrices.

After the evaluation of the IR spectra of the pure corrosion inhibitors, hybrid-layers modified with both compounds were studied by FT-IRRAS in order to reveal any information about the incorporation of the inhibitors into the organosilane matrices. The collected spectra are illustrated in Figure 4.8.2 where both modified hybrid-layers refer to the corresponding unmodified films applied on ZE (Fig. 4.8.2a) and HDG (Fig. 4.8.2b).

Evaluating the spectra with respect to the corrosion inhibition markers, only the vibrations of the acrylic acid ester in the PDMAEMA nanocontainers were revealed which appear at 1720 cm^{-1} and are indicated by the blue ellipses. The Mg-LDH-VO_3 marker at 440 cm^{-1} is not visible in either spectra on ZE and HDG. This result does not necessarily lead to the conclusion that Mg-LDH-VO_3 pigments are not incorporated into the hybrid-films, since the marker can be overlaid by the intensive absorbance derived from the zirconium oxide matrix, especially if it can be assumed that the concentration of Mg-LDH-VO_3 is small in the hybrid-layers.

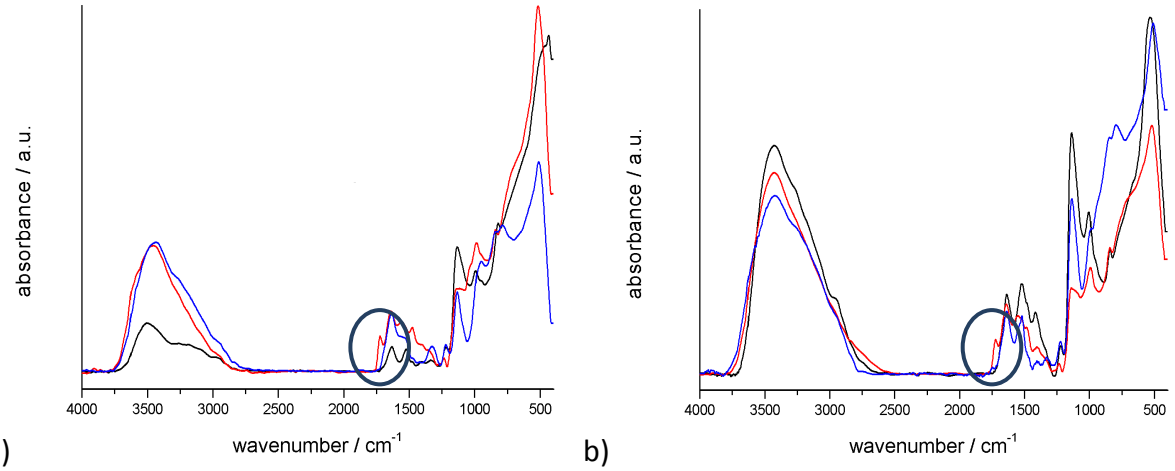

Fig. 4.8.2: FT-IRRAS spectra of a hybrid-layer (black graph), a hybrid-layer modified with PDMAEMA/0.5%MTBT nanocontainers (red graph) and with Mg-LDH-VO_3 pigments (blue graph) on a) ZE and b) HDG.

However, the co-deposition of the PDMAEMA/MTBT nanocontainers from modified hybrid-systems was revealed independently of the used metallic substrates.

Since Mg-LDH-VO_3 pigments could not be detected in the hybrid-layers by FT-IRRAS, XPS studies were additionally conducted on these samples for the purpose of revealing vanadium inside the layers. Vanadium was chosen since it can only be derived from the Mg-LDH-VO_3 due to its absence in pure hybrid-layer-matrices. The detected XPS spectra are shown in Figure 4.8.3; the hybrid-layer on ZE is illustrated in Figure 4.8.3a, and the one on HDG in Figure 4.8.3b.

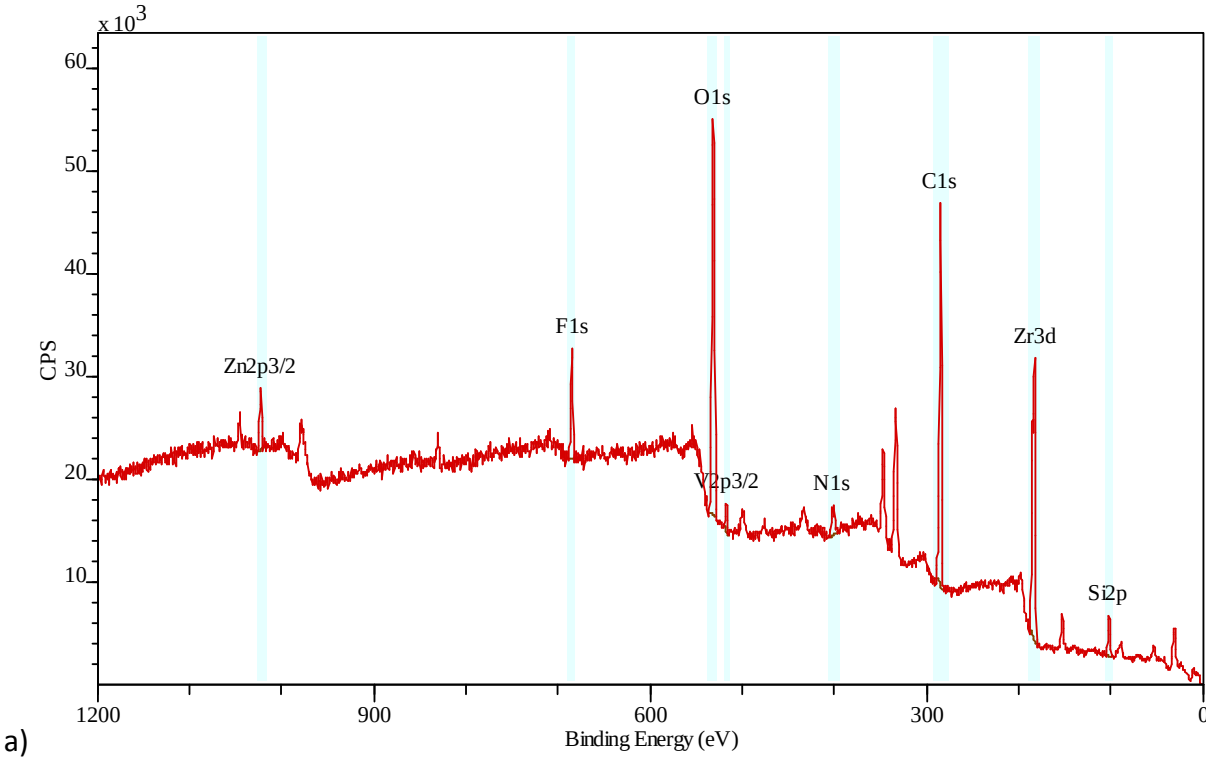

a)

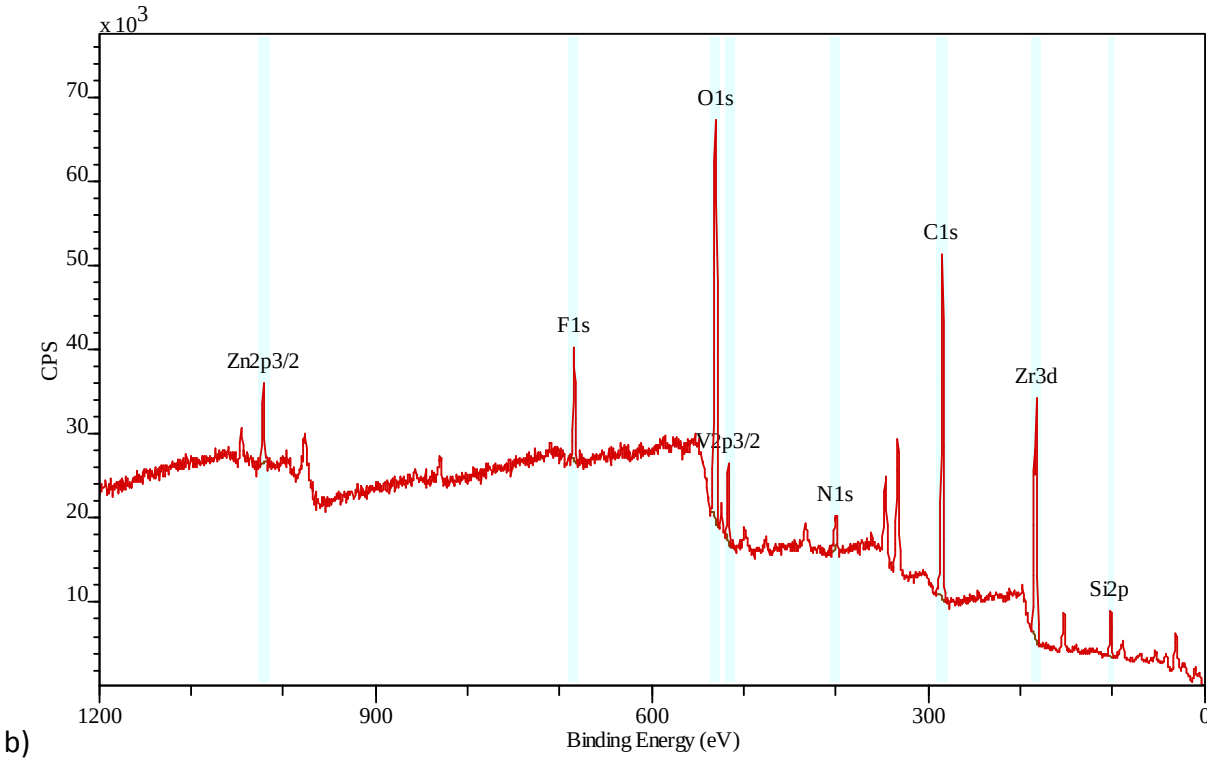

b)

Fig. 4.8.3: XPS survey spectra on hybrid-layers modified by Mg-LDH-VO_3 pigments, applied on a) ZE and b) HDG.

On both samples vanadium was detected. The most intense peaks appear at 517 eV and 525 eV and can be assigned to vanadium 2p orbitals. In Figure 4.8.3 only the V 2p 2/3 peak at 517 eV is marked,

for the purpose of simplification. Both spectra were furthermore fitted to enable the comparison of the atomic percentages of the elements inside the modified hybrid-layers, whereas it is necessary to bear in mind that the penetration depth of XPS is only 2–3 nm, which limits the significance of the element distribution for the upper atomic layers. This cannot be generalized for deeper structures.

However, the element distribution gained from XPS shown in Table 4.8.1 reveals vanadium concentrations between 0.5 at% for hybrid-layers deposited on ZE and 1.5 at% for those deposited on HDG. Even though these results do not expose information for the deeper hybrid-layers the comparison of the element distribution enables predictions about the amount of incorporated Mg-LDH-VO_3. Since the main compounds of the hybrid-layer, which are the inorganic fluor-rich zirconia matrix and the amino-functional organosilane matrix, did not reveal higher fluor and nitrogen concentrations than 3 at% and an average vanadium concentration of 1 at%, this leads to the conclusion that the incorporated Mg-LDH-VO_3 amount is not negligible.

Table 4.8.1: Element distribution of hybrid-layers modified with Mg-LDH-VO_3 pigments, applied on ZE and HDG.

peak	binding energy / eV	atomic concentration / at%	
		HDG	**ZE**
Zn2p3/2	1021.5	0.5	0.3
F1s	684	3.1	2.6
O1s	531	25.7	21.9
V2p3/2	516.5	**1.5**	**0.5**
N1s	400.5	3.2	3.4
C1s	284	50.5	54
Zr3d	181.5	7.6	9.3
Si2p	101.5	7.9	8

Moreover, vanadium element spectra were recorded by XPS in order to analyze the oxidation state of vanadium, as is shown in Figure 4.8.4. The vanadium 2p 3/2 peak appeared for both substrates at 516.5 eV which is characteristic for vanadium(V) and illustrates that vanadate was not reduced during the film formation process.

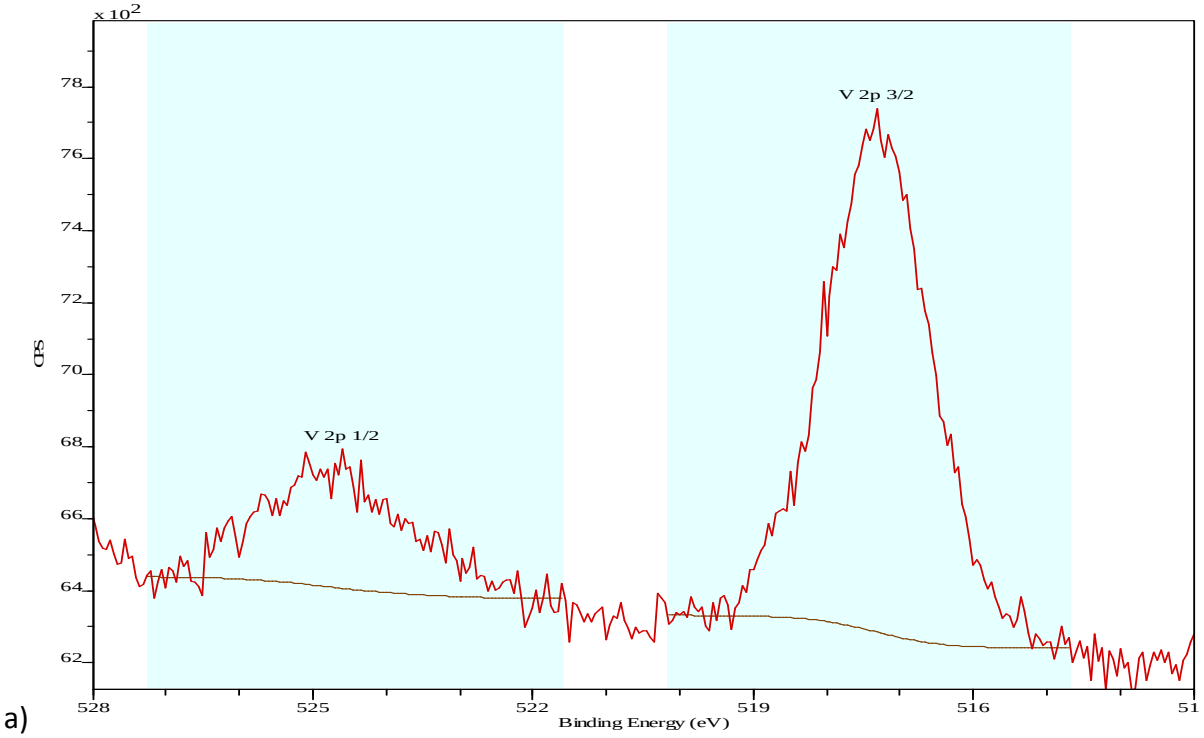

a)

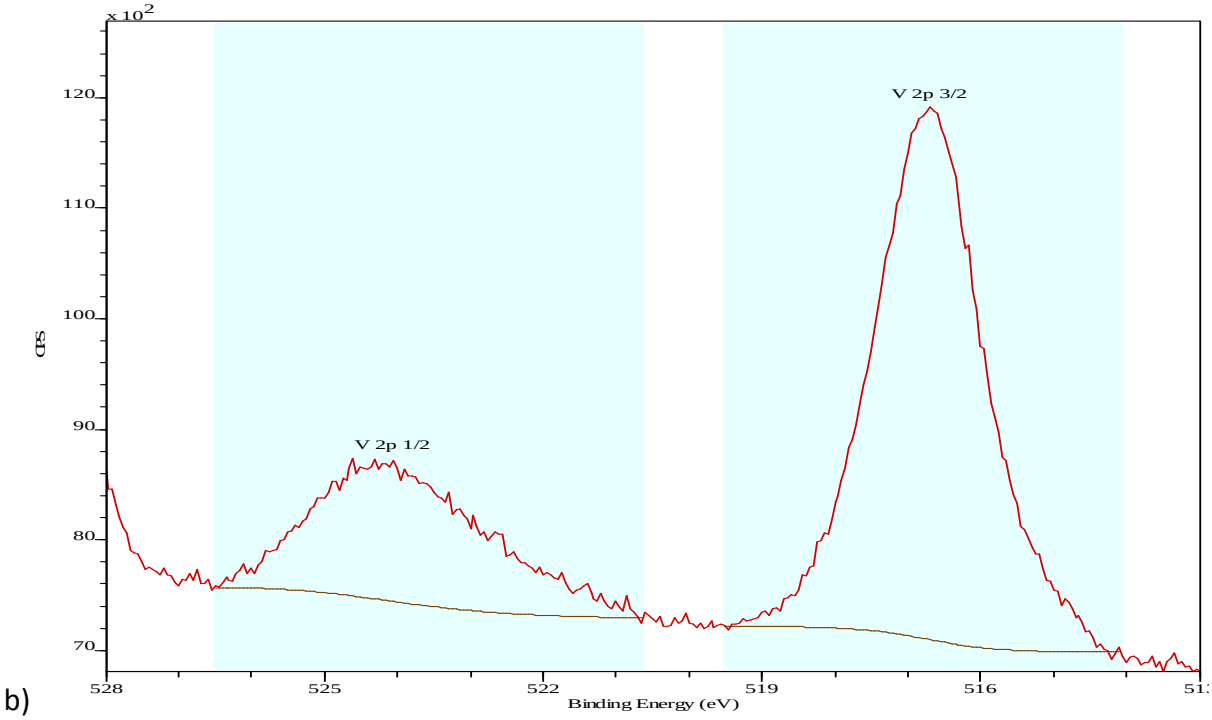

b)

Fig. 4.8.4: XPS V 2p element spectra on hybrid-layers modified by Mg-LDH-VO_3 pigments, applied on a) ZE and b) HDG.

4.8.2 Evolution of the barrier properties of modified hybrid-layers in corrosive media

The barrier properties and the layer resistances under corrosive environments were investigated by means of electrochemical impedance spectroscopy and cyclic voltammetry on unmodified and modified hybrid-layers as well as copper-containing hybrid-layers, all applied on ZE. Thereby the studied samples were exposed to 0.5 M sodium chloride solution. For the purpose of in-situ detection of the degradation of the layers and the simultaneously occurring reduction of the surface coverage cycles, electrochemical studies were conducted. These cycles contained 300 s open circuit potential (OCP) detection, subsequently EIS, and finally CV measurements. The OCP was recorded in order to ensure that the system always reached a steady state with respect to the thermodynamic equilibrium between anodic and cathodic processes at the metal/electrolyte interface before the following EIS measurement was started.

However, all cycles were converted into the elapsed time under a corrosive environment in order to ease their evaluation. The evolution of degradation of the barrier properties and pore resistances of the investigated samples are illustrated for the initial states and then after 1 h, 3 h, 6 h (see Figure 4.8.5), 9 h, 12 h, 15 h and 18 h (see Figure 4.8.6). In both figures only the impedances are shown for simplification. The corresponding phases are illustrated with further impedance graphs in the appendix.

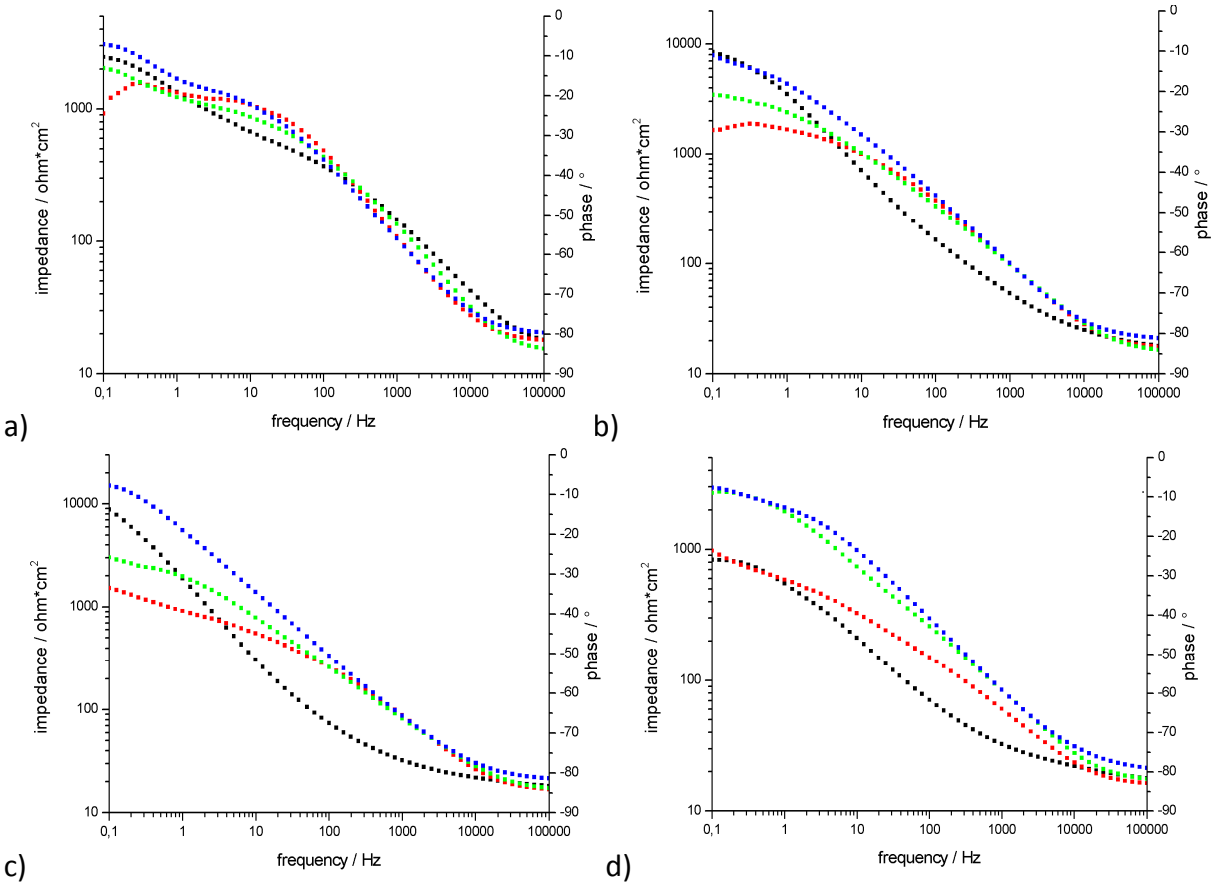

Fig. 4.8.5: Impedances up to 6 h of EIS measurements on ZE coated with non-modified copper-free (red graphs) and copper-containing (black graphs) hybrid-layers as well as with copper-free hybrid-layers modified with PDMAEMA/0.5%MTBT nanocontainers (green graphs) and Mg-LDH-VO_3 pigments (blue graphs). All spectra were recorded in 0.5 M NaCl solution by continuously proceeded cycles of electrochemical measurements containing EIS and CV. a) start of measurement; b) after 1 h; c) after 3 h; d) after 6 h.

The initial impedances shown in Figure 4.8.5a reveal similar impedances for all samples in both frequency regions assigned to the film capacitances and their pore resistances. This fact enables the evaluation of the velocity of film degradation just by comparison of the pure impedance curves. The results which are presented in Figure 4.8.5b show the impedances after 1 h of corrosion. It is obvious that pore resistances of both modified hybrid-systems and the copper-containing hybrid-film have been increased while the ones for the pure hybrid-system seem to remain unaffected. This assumption is indeed not true with respect to the evolution of impedances within the first 60 min of corrosion as illustrated by the spectra shown in the appendix. There it becomes obvious that the pore resistance of the hybrid-layer also increased after the first cycle of measurements and subsequently continuously decreased reaching a level, after 1 h, comparable to the initial impedance.

However, the increase of the pore resistance by impact of the corrosive electrolyte is initially affected on all samples by the additional coverage at the metal/electrolyte interface inside the pores by corrosive products which probably consist mainly of $Zn(OH)_2$ in this case. Further corrosion then

leads to an enlargement of the pores by beginning the corrosive degradation of the film matrix and cathodic delamination at the metal/film interface which easily overcomes (already after 20 min) the above-mentioned additional barrier effect on pure hybrid-layers.

For the modified copper-containing and copper-free hybrid-layers, the increase of the pore resistances remains ongoing within the first 60 min of corrosion (see appendix 1). It finally ends in impedances which are significantly higher in comparison to the initial states. It can be concluded that this result was caused by the release of the corrosion inhibitors for the modified hybrid-layers and by the higher film thickness of the copper-containing hybrid-layers which also effect a higher buffer capacitance than is available in unmodified and copper-free hybrid-layers.

Since the effect of both corrosion inhibitors, PDMAEMA/MTBT and Mg-LDH-VO_3, is temporally delayed, their anti-corrosion properties are increasingly exposed within several hours of corrosion as illustrated in Figures 4.8.5c and d. Thereby the MTBT is gradually released from the capsules when the pH increases, caused by oxygen reduction, whereas the vanadate is exchanged little by little with chloride in the case of the Mg-LDH-VO_3 modified system. These processes cause significantly higher pore resistances as well as barrier properties after 3 h and even more after 6 h of measurements for both modified hybrid-layers, whereas the performance of the Mg-LDH-VO_3 pigments is slightly better than that of the PDMAEMA/MTBT nanocontainers.

Long-term stability of the modified systems can only be evaluated by continuing the electrochemical measurements till breakdown of the complete barriers which is almost reached after 18 h of measurement, as shown in Figure 4.8.6.

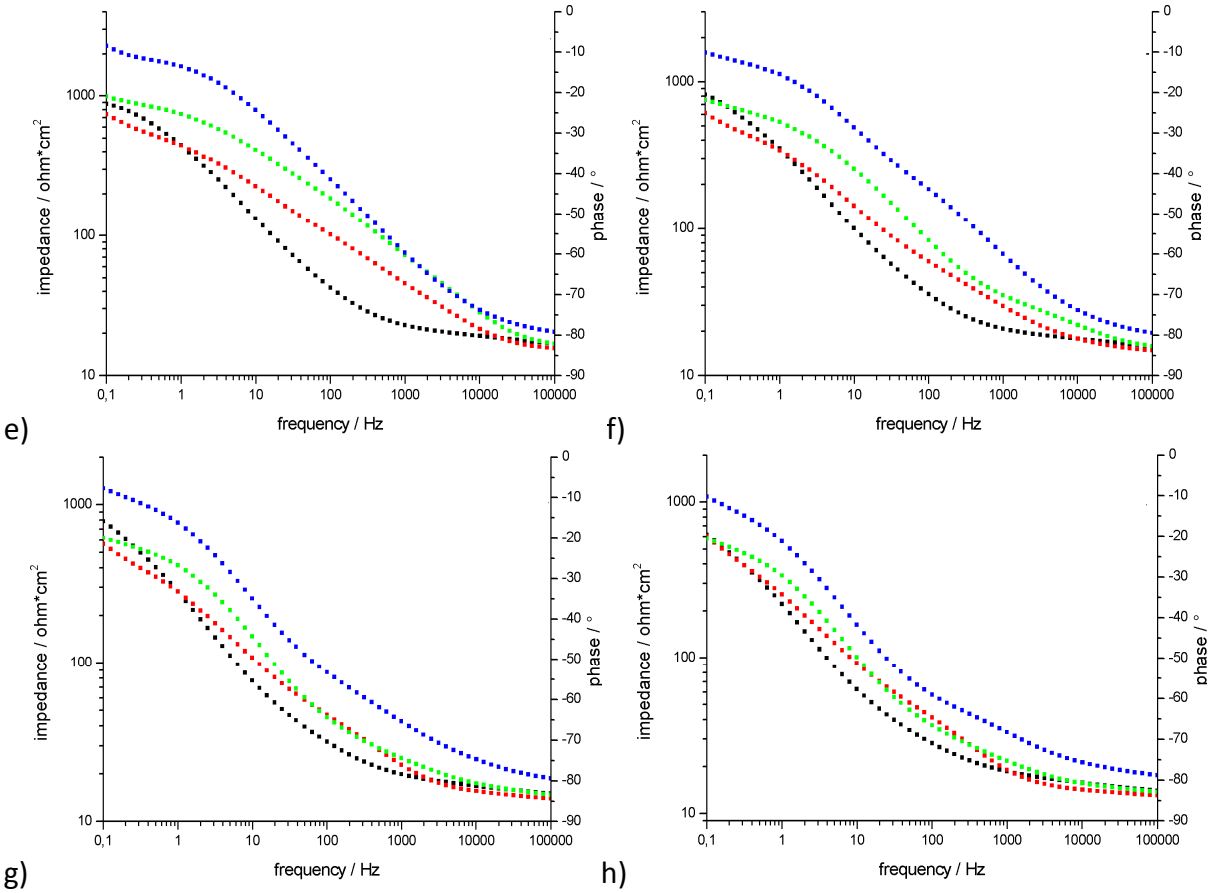

Fig. 4.8.6: Impedances between 6 h and 18 h of EIS measurements on ZE coated with non-modified copper-free (red graphs) and copper-containing (black graphs) hybrid-layers as well as with copper-free hybrid-layers modified with PDMAEMA/0.5%MTBT nanocontainers (green graphs) and Mg-LDH-VO_3 pigments (blue graphs). All spectra were recorded in 0.5 M NaCl solution by continuously proceeded cycles of electrochemical measurements containing EIS and CV. e) after 9 h; f) after 12 h; g) after 15 h; h) after 18 h.

After 9 h (see Fig. 4.8.6e) of measurement, the impedances of all samples were significantly reduced compared to the results obtained after 6 h. The pore resistances and layer capacitances of the Mg-LDH-VO_3 modified hybrid-layers remained significantly higher than for the ones modified with PDMAEMA/MTBT and even more than those for the pure hybrid-layers.

The impedances detected after 12 h and 15 h of measurement (see Figs. 4.8.6f and g) show a further convergence of the values for the unmodified hybrid-layers and those with PDMAEMA/MTBT while the one with Mg-LDH-VO_3 pigments still remains at a higher resistance. Thereby all the impedances are furthermore decreased compared to the values after 6 h and 9 h of corrosion.

After 18 h the impedances of PDMAEMA/MTBT reached equality with the values measured for the unmodified hybrid-layers while the values for the Mg-LDH-VO_3 modified sample remain a little higher. Hence it is concluded that either the complete supply of the nanocontainers is consumed and

can therefore not cover newly released parts of the metal surface, or that the already released MTBT is partly removed from the surface due to weak initial adsorption on the surface.

However, all results in Fig. 4.8.6 confirm the conclusions drawn by the previous results (see Fig. 4.8.5) which were that the corrosion inhibition properties of Mg-LDH-VO_3 pigments are better than of those of PDMAEMA/MTBT nanocontainers, especially with respect to long-term stability.

Beside EIS measurements, CVs were also conducted in order to study in-situ the dependency between the decrease of the layer impedances and its surface coverage. CVs are shown in Figure 4.8.7 according to the previous EIS spectra containing the initial state and further results after 1 h, 3 h and 6 h under a corrosive environment.

The CV of the initial state is presented in Figure 4.8.7a. The hybrid-layer modified with Mg-LDH-VO_3 (the blue graph) revealed the highest anodic and cathodic current densities, which indicates a lower surface coverage than the other hybrid-layer-coated samples under the assumption of equal film thicknesses. This result is suggested to be caused by a higher porosity of the Mg-LDH-VO_3 modified hybrid-layer since significant defects of the films are not visible, as shown on FE-SEM images later on (see Fig. 4.8.9).

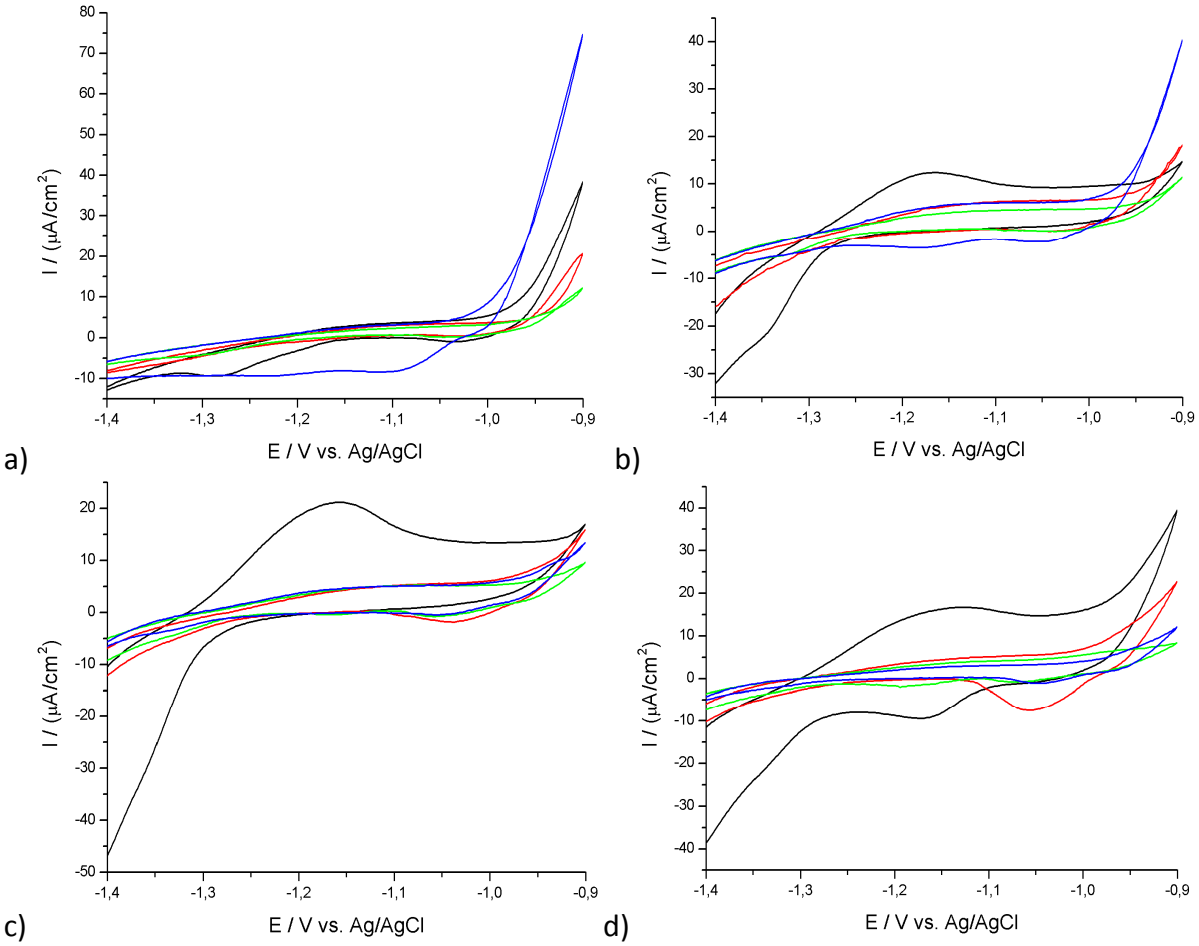

Fig. 4.8.7: Cyclovoltammograms of up to 6 h of CV measurements on ZE coated with non-modified copper-free (red graphs) and copper-containing (black graphs) hybrid-layers as well as with copper-free hybrid-layers modified with PDMAEMA/0.5%MTBT nanocontainers (green graphs) and Mg-LDH-VO_3 pigments (blue graphs). All spectra were recorded in 0.5 M NaCl solution by continuously proceeded cycles of electrochemical measurements containing EIS and CV. a) start of measurement; b) after 1 h; c) after 3 h; d) after 6 h.

In contrast, the CVs measured on the hybrid-layer modified with the PDMAEMA/MTBT nanocontainer reveal the lowest current densities concerning anodic as well as cathodic processes. This result is assumed to be caused by the additional barrier properties of the silica clays inside the nanocontainers which hinder the electrolyte diffusion to the metal/organosilane interface. Hence these nanocontainers reveal blocking abilities which are independent of the time-delayed release of the 2-(methylthio)benzothiazole.

Comparing the voltammograms which were recorded after 1 h, 3 h and 6 h, the time-delayed impact of the corrosion inhibitors becomes obvious since the anodic and cathodic currents of both modified systems are decreased, whereas the values detected for the unmodified layers increase.

Both modified hybrid-systems show the highest inhibition of electrochemical reactions after 6 h which is clear by comparison of the graphs illustrated in Figure 4.8.7 with those shown in Figure 4.8.8. The loss of the barrier properties of the corrosion inhibitors after 9 h (see Fig. 4.8.8a) is well detected by the increased zinc reduction peak at around -1.08 $V_{Ag/AgCl}$.

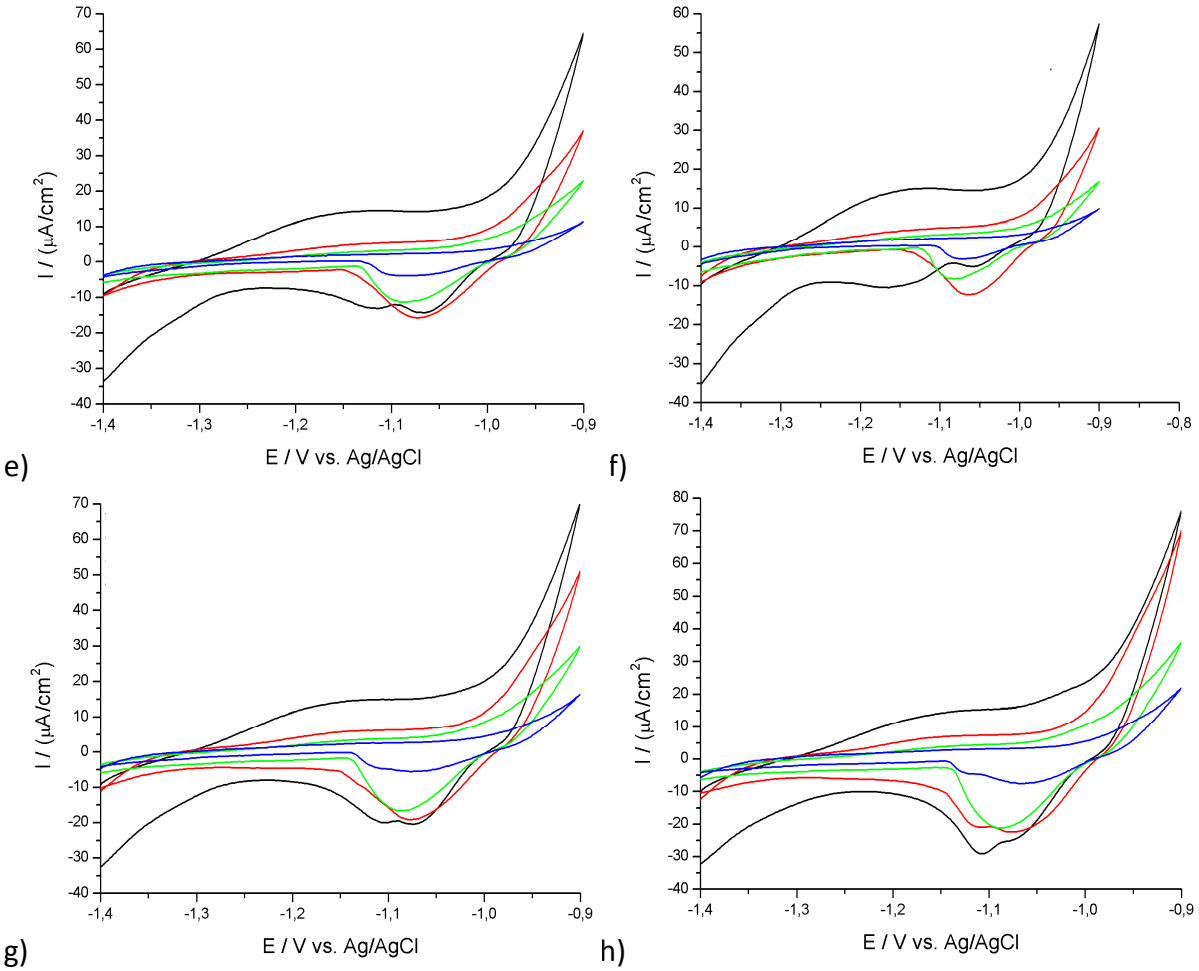

Fig. 4.8.8: Cyclovoltammograms between 6 h and 18 h of CV measurements on ZE coated with non-modified copper-free (red graphs) and copper-containing (black graphs) hybrid-layers as well as with copper-free hybrid-layers modified with PDMAEMA/0.5%MTBT nanocontainers (green graphs) and Mg-LDH-VO_3 pigments (blue graphs). All spectra were recorded in 0.5 M NaCl solution by continuously proceeded cycles of electrochemical measurements containing EIS and CV. e) after 9 h; f) after 12 h; g) after 15 h; h) after 18 h.

However, these results are in good agreement with the previous EIS measurements, in which both modified hybrid-layers showed the best barrier properties after 6 h of corrosion and significantly decreased impedances after 9 h, while the long-term stability of the Mg-LDH-VO_3 modified layers is better than that of those with PDMAEMA/MTBT. Additionally, these results are confirmed by the CVs measured after 12 h, 15 h and 18 h where anodic and cathodic current densities are much higher for the hybrid-layers modified with PDMAEMA/MTBT nanocontainers than with Mg-LDH-VO_3 pigments.

The CVs detected on the copper-containing hybrid-layers cannot be compared with the modified and unmodified hybrid-layers with respect to the surface coverage as already discussed for the EIS measurements. However, characteristic of the copper-containing hybrid-layers are higher cathodic current densities by cathodic polarization of more than -1.1 $V_{Ag/AgCl}$ where oxygen reduction and finally cathodic water dissociation takes place. Also, higher anodic current densities are measured even after 1 h of corrosion, which cannot be directly connected to one anodic process as the copper-containing hybrid-system is more complex than the copper-free one. Finally, it can just be noticed for copper-containing hybrid-layers that the CVs are also in good agreement with the reduction of the layer impedances as measured by EIS and that these layers are also degraded in a highly corrosive environment.

4.8.3 Morphologies of hybrid-layers containing corrosion inhibitors

In order to gain information about the morphology and surface coverage of hybrid-layers with respect to any influence by modification of corrosion inhibitors, FE-SEM images were collected on modified hybrid-layers applied on ZE (see Fig. 4.8.9) and HDG (see Fig. 4.8.10).

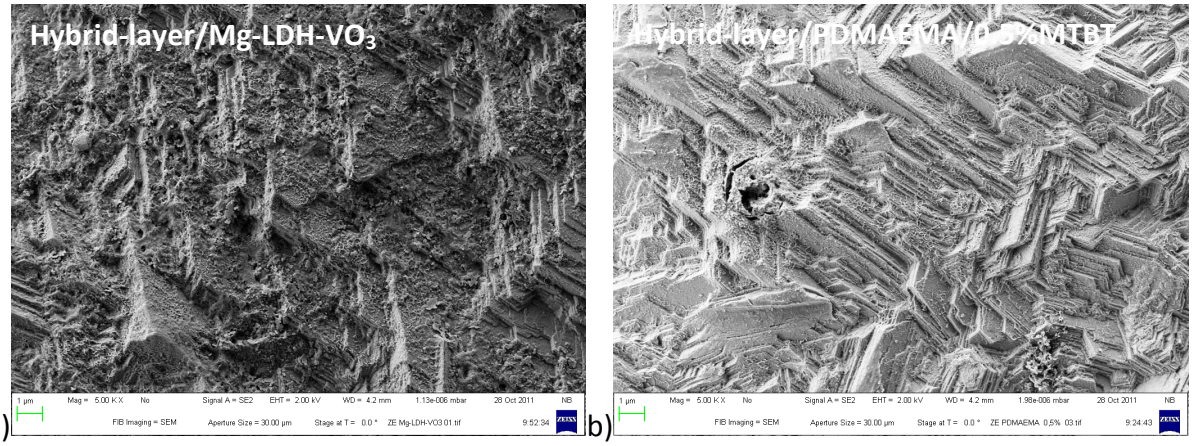

Fig. 4.8.9: FE-SEM images on ZE coated with differently modified hybrid-layers. a) Hybrid-layer with Mg-LDH-VO_3 pigments; b) Hybrid-layer with PDMAEMA nanocontainers including 0.5% MTBT.

For both modified hybrid-systems, the layer morphology is independent of the substrate's nature. Both surfaces are widely covered, which is obvious from the coated edges and terraces in the case of ZE as well as the coverage of grains and grain boundaries on HDG. Regarding the structure of both modified hybrid-systems, no significant differences between the incorporation of Mg-LDH-VO_3 or PDMAEMA/MTBT are visible. Thus no confirmation of the CV results, which indicated a lower surface coverage of the hybrid-layers as a result of incorporation of Mg-LDH-VO_3 pigments, can be drawn.

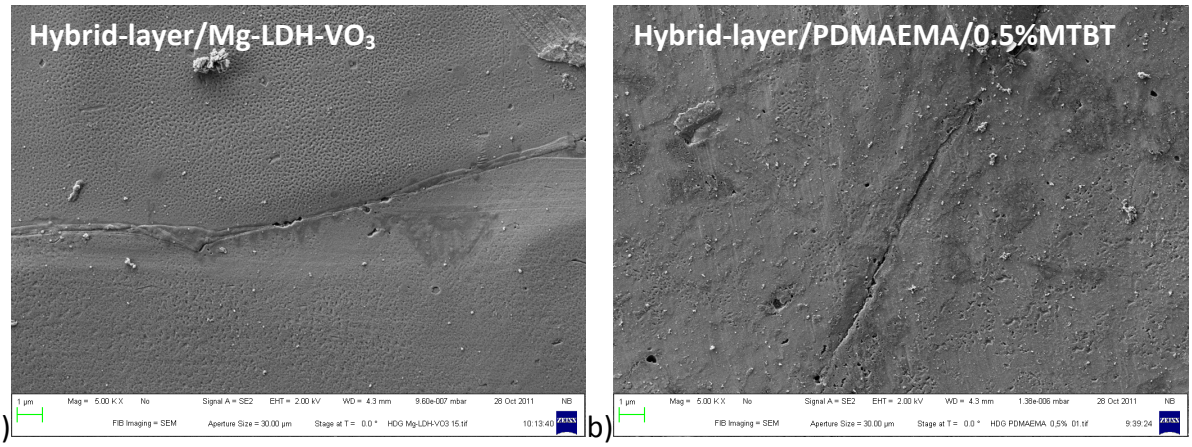

a) b)

Fig. 4.8.10: FE-SEM images on HDG coated with differently modified hybrid-layers. a) Hybrid-layer with Mg-LDH-VO_3 pigments; b) Hybrid-layer with PDMAEMA nanocontainers including 0.5% MTBT.

With respect to the morphologies of unmodified hybrid-layers on HDG, which are known to be mainly characterized by different porous needle-like or even cubic structures on the surfaces, rather flat morphologies were imaged on modified hybrid-layers on HDG. However, by the coverage of the grain boundaries in both images presented in Fig. 4.8.10, it is clearly shown that the HDG surface is widely coated independently of any film modification.

Moreover, no conclusions could be drawn from the FE-SEM images about the structure of the incorporated corrosion inhibitors since their unique shape is, so far, unknown.

4.8.4 Conclusions

Mg-LDH-VO_3-pigments, as well as nanocontainers made of Si-clays and MTBT encapsulated in PDMAEMA, was incorporated into the hybrid-layers by co-deposition during the hybrid-film formation. This result was shown on ZE and HDG by means of FT-IRRAS and XPS, while the incorporation PDMAEMA/MTBT nanocontainers was revealed by FT-IRRAS, and the incorporation of Mg-LDH-VO_3 by XPS. Furthermore, XPS element studies of the 2p vanadium peaks showed that vanadate was not reduced during the conversion process, which is the reason for unhindered anion exchange.

In the case of Mg-LDH-VO_3, vanadate is exchanged with chloride which leads to a lower halide concentration as well as to repassivation at the metal/electrolyte interface by deposition of vanadium hydroxide. XPS survey spectra reveal moreover that the atomic distribution of vanadium at the hybrid-layer surface varied between 0.5 at% (on HDG) and 1.5 at% (on ZE).

Electrochemical studies of both modified hybrid-layers revealed the corrosion inhibition properties of both systems, which were simulated by treatment with 0.5 M NaCl solution. The increased barrier properties were only achieved by time-delay in a corrosive environment and were not found for the freshly modified hybrid-layers as compared to the unmodified layers. The long-term stability of the Mg-LDH-VO_3 modified system was significantly higher than that of the one modified with PDMAEMA/MTBT nanocontainers. However, CV studies on hybrid-layers modified with Mg-LDH-VO_3 indicated a lower surface coverage, which could not, in the end, be confirmed by FE-SEM imaging.

5 Overall Conclusions and Outlook

Aqueous, acidic conversion solutions consisting of γ-APS oligomers and hexafluorozirconic acid was studied. The steady-state of the solution was characterized by weakly crosslinked poly-organosilanes which are electrostatically diluted and stabilized by NH^{3+}-functions. The silanol functions are either condensed or remain unaffected.

The resulting films, obtained by immersion of metallic substrates into the conversion solutions, were characterized as nano-porous layers with thicknesses between 60 nm and 130 nm which properties are influenced by the chemical compositions of the conversion baths as well as the chemical natures of the coated alloys. The inorganic compounds of the hybrid-layers are described by condensed fluorhydroxooxozirconates, which are crosslinked by O-Zr-O bondings. The inorganic particles show very compact structures and are embedded into the nanoporous organosilane. This matrix is also crosslinked, even directly after the film formation process, but can be further proceeded by tempering at 70 °C.

The stability of organosilane-based layers was investigated by a zirconia/γ-APS bilayer system applied on pure iron surfaces in order to separate degradative and corrosive effects occurring at organic and inorganic matrices, respectively. In this way it was revealed, with regard to the corrosion protection properties of the different films, that organosilane and zirconia single layers as well as the zirconia/γ-APS bilayer system inhibit the cathodic and anodic processes. Moreover, the inhibition of the oxygen reduction process at the electrolyte/electrode interface could be directly correlated with the kinetics of electrowetting under atmospheric conditions.

As shown by the HR-SKP studies, the progress of cathodic oxygen reduction along the iron surface is inhibited for both single layer systems, based on γ-APS and zirconia. The fact that the progress of cathodic electrowetting is even more strongly inhibited by the zirconia than by the organosilane layer is supposed to be a result of the high stability of zirconia under the conditions of oxygen reduction. Moreover it was concluded that the oxygen reduction at the γ-APS single layer system occurs at the whole substrate/γ-APS interfacial region but only in pores of the undamaged inorganic matrix in the zirconia single layer system. This is additionally the reason why it was assumed that the cathodic

delamination on the γ-APS/zirconia-bilayer system proceeds at the γ-APS/zirconia interface and not at the iron/zirconia interface area.

By comparing the corrosion studies conducted on the zirconia/γ-APS bilayer system to hybrid-layers, it was shown that the inhibition of cathodic delamination at the metal/polymer interface is significantly higher for hybrid-layer-coated metal surfaces than for γ-APS/ZrO_x bilayer-coated ones. As shown by ellipsommetry and FE-SEM imaging, the γ-APS layer of the γ-APS/ZrO_x bilayer system is around 10 nm thick while the hybrid-layers are at least 50 nm thick. Thus one reason for the higher stability of the hybrid-layers during cathodic delamination is its higher buffer capacitance due to thicker layer matrices. Furthermore the inorganic matrix, consisting of fluorhydroxooxozirconates, is stable under conditions of oxidative degradation. Hence it can be concluded that the delamination velocity for the hybrid-layer is additionally decreased by the inorganic compounds which are embedded into the organosilane matrix.

In order to enhance the anti-corrosion properties of hybrid-layers these were studied with regard to modification of the parameters during the conversion process as well as to establish additional post-treatment. In terms of parameter modification, the influence of the bath temperature, as well as the stirring velocity during the conversion process, was investigated. While the latter did not reveal any significant dependency of the film properties on the stirring velocity, the increased bath temperature slightly increased the barrier properties and the surface coverage.

In contrast, a significant enhancement of layer properties was achieved by changing the deposition process from continuous coating to a step-wise conversion process. Electrochemical studies illustrated that a step-wise immersion (3 x 1 min) leads to higher barrier properties of the applied conversion layers. Furthermore, a higher degree of surface coverage after the three-step coating process was revealed, especially if the samples were additionally annealed for 10 min at 120 °C after each conversion step.

The thicknesses and morphologies of the copper-containing hybrid-layers were significantly influenced by the copper nitrate, as shown by FE-SEM. These layers, deposited within the same immersion time, were found to be around twice as thick as known from copper-free hybrid-layers and led hence to better surface coverage, especially on ZE. Depending on the coated substrate layer, thicknesses between 110 nm and 130 nm were revealed.

Moreover, the morphologies of the copper-containing hybrid-layers were characterized by globular particles which were embedded into the film matrices and showed crystalline shapes. XPS measurements illustrated furthermore that the zirconium/silicon ratio on the surfaces of the copper-containing hybrid-layer were twice as high as those known from copper-free hybrid-layers. By this 14–15 at% zirconium was detected on the surfaces, depending on the substrate. Thus it was concluded that the globular particles mainly consist of zirconium.

The increased layer thicknesses and different morphologies of copper-containing hybrid-layers as compared to copper-free ones can be explained by the electrochemical properties of copper. If the film formation processes start by the anodic dissolution of the metallic substrate surfaces, the copper reduction at the metal/NDL interface is thermodynamically superior to the hydrogen reduction due to the relatively higher cathodic electrochemical potential of copper as compared to hydrogen.
Thus copper is initially deposited on the substrate surfaces, which can subsequently act as a local electrochemical cell and accelerate both the anodic and cathodic electrochemical processes. Thereby the anodic metal dissolution is unlimited whereas the copper deposition is limited by the supply from the bulk solution. Hence the migration of copper nitrate through the NDL is rate-determining for this process and leads to a depletion of copper nitrate near the interfacial area. As a result of this, proton reduction appears mainly as the counter-reaction to the metal dissolution which leads in turn to a stronger pH gradient inside the NDL. In this way the destabilization and co-aggregation of the bath compounds also accelerate which finally ends in higher film thicknesses.

In addition to the increased pH gradient in the NDL, heterogeneous nucleation of zirconia-based pre-colloids is initiated by the copper nitrate. Zirconia particles grow up from “copper islands” on the metal surfaces while they are embedded into the simultaneously deposited organosilane matrix. This process is the reason for the appearance of globular particles incorporated into the copper-containing hybrid-layers.

Moreover, post-treatment of hybrid- layers was conducted with solutions containing self-assembling molecules. Since it was known that octadecylthiol (ODT) and octadecylphosphic acid (ODPA) adsorb on zinc oxide and form monolayers on the zinc oxide surface, both compounds were used in order to block the submicroscopic surfaces inside the nanopores in the hybrid-layers. Therefore hybrid- layers were post-treated with either ODT or ODPA or a 50%/50% mixture of both. It was shown that ODPA adsorbs better on the base hybrid-layer than ODT. This result was confirmed by electrochemical studies which also illustrated that higher film and pore resistances could be obtained based on ODPA in comparison to ODT.

In order to improve the buffer effects of the hybrid-layers nanocontainers were incorporated into their matrices. Mg-LDH-VO_3-pigments as well as nanocontainers made of Si-clays and MTBT encapsulated in PDMAEMA were used. Electrochemical studies of the nanocontainer-modified hybrid-layers revealed in a 0.5 M NaCl solution significantly higher stabilities than the unmodified systems. The long-term stability of the Mg-LDH-VO_3 modified system was significantly higher than that of the one modified with PDMAEMA/MTBT nanocontainers.

In order to confirm these results, studies of the cathodic delamination of the modified systems under conditions of oxygen reduction should be conducted. Furthermore, other additives need to be found which can either increase the film thicknesses or improve the leaching abilities of the resulting layers. Finally, these systems need to be compared by VDA test in order to confirm their long-term stability.

6 References

[1] D.D. Macdonald, *J. Electrochem. Soc*. **139** (12) (1992) 3434.

[2] W.P.Yang, D. Costa and P. Marcus in *Oxide Films on Metals and Alloys* (B. MacDougall, R.S. Alwitt and T.A. Ramanarayanan eds), *Proceedings*, Vols. 92-22, The Electrochemical Society, Princeton, NJ (1992) 516.

[3] P. Marcus and J.M. Herbelin, *Corros. Sci*. **34** (1993) 1123.

[4] H.H. Strehblow, *Proc. Corros*. **91**, NACE, Houston, TX (1991) 76.

[5] K. J. Vetter, *J. Electrochem. Soc.* **110** (6) (1963) 597.

[6] W.Pasche. *Surf. Sci.* **37** (1973) 59.

[7] H.Gobrecht, W. Paatsch and R.Thull, *Ber. Bunsen-Ges.* **75** (12) (1971) 1353.

[8] M. Pourbaix, *Atlas d´Equilibres Electrochimiques*, Guthier Villars + Cie, Paris, France (1963).

[9] M. Pourbaix, *Atlas of the Electrochemical Equilibria in Aqueous Solutions*, Pergamon, Oxford (1966).

[10] H.H. Strehblow, *Passivity of Metals*, R.C. Alkire and D.M. Kolb, eds., Advances in Electrochemical Science and Engineering, ‘’Vol. 8, Wiley-VCH, Weinheim, Germany (2003).

[11] H.H. Strehblow, *Werkst. Korros*. **27** (1976) 792.

[12] T.P. Hoar, D.C. Mears and G.P. Rothwell, *Corros. Sci*. **5** (1965) 279.

[13] C.Y. Chao, L.F. Lin and D.D. Macdonald, *J. Electrochem. Soc.* **128** (1981) 1191.

[14] C.Y. Chao, L.F. Lin and D.D. Macdonald, *J. Electrochem. Soc.* **128** (1981) 1194.

[15] K.J. Vetter and H.H. Strehblow, *Ber. Bunsen. Ges. Phys. Chem*. **74** (1970) 1024.

[16] N. Sato, *Electrochim. Acta* **16** (1971) 1683.

[17] N. Sato, K. Kudo and T. Noda, E*lectrochim. Acta* **16** (1971) 1909.

[18] Y.J. Kolotyrkin, *Corrosion* **19** (1964) 261.

[19] T.P. Hoar and W.R. Jacob, *Nature* **216** (1967) 1299.

[20] B.P. Löchel and H.H. Strehblow, *Electrochim. Acta* **28** (1983) 565.

[21] K.E. Heusler and L. Fischer, *Werkst. Korros*. **27** (1976) 551.

[22] H.H. Strehblow, B. Titze and B.P. Löchel, *Corros. Sci*. **19** (1979) 1047.

[23] H.H. Strehblow, *Werkst. Korros*. **35** (1984) 437.

[24] R. Grauer, *Werkstoffe und Korrosion* **32** (1981) 113.

[25] U.R. Evans, *Trans. Inst. Met. Finishing* **37** (1960) 1.

[26] U.R. Evans, *Nature* **206** (1965) 980.

[27] U.R. Evans and C.A. Taylor, *Corros. Sci.* **12** (1972) 227.

[28] M. Stratmann, K. Bohnenkamp, H.J. Engell, *Werkstoffe und Korrosion* **34** (1983) 604.

[29] N.Pilling and R. Bedworth, *J. Inst. Metals* **29** (1923) 534.

[30] M.V. Veazey, *Mater. Perform.* **40** (8) (2001) 18.

[31] S. Szabo and I. Bakos, *Corros. Rev*. **24** (1-2) (2006) 39.

[32] R.H. Heidersbach in *AMS Handbook , vol. 13: Corrosion*, ASM international, The Materials Society, (1987) 466.

[33] P.A. Schweitzer, *Corros. Engineer. Handbook*, Marcel Dekker, Inc. New York (1996) 545.

[34] R.H. Heidersbach, in *ASM Handbook, vol. 13A: Corrosion*, ASM international, Materials Park, USA (2003) 855.

[35] Zink-Taschenbuch, Zinkberatung e.V. Düsseldorf.

[36] DIN 1706 Zink, DIN 9722 Bleche und Bänder aus Zink, DIN 17 770 Bleche und Bäder aus Zink, techn. Lieferbedingungen.

[37] K.A. von Oeteren „Feuerverzinkung“ expert. Verlag 1988.

[38] H. Gerischer, *Advances in Electrochemistry and Electrochemical Engineering* (P. Delahay and C.W. Tobias Editors), New York, *Interscience Publs.* (1961) 139.

[39] A. Many, Y. Goldstein, N.B. Grover, *Semiconductor Surfaces*, J. Wiley, New York 1965.

[40] S.R. Morrison, T. Freund, *Electrochim Acta* **13** (1968) 1343.

[41] B. Dettinger, H.R. Schöppel, T. Yokoyama, H. Gerischer, *Ber. Bunsendes. Phys. Chem.* **78** (1974) 1024.

[42] O. Fruhwirth, J. Friedmann, G.W. Herzog, *Surface Technology* **4** (1967) 417.

[43] H. Kaesche, Die Korrosion der Metalle, *Springer-Verlag Berlin, Heidelberg, New-York* 1966.

[44] R.S. Alwitt, The Aluminium-Water-System, in J.W. Diggle and A.K. Vijh (Ed.) Oxide and Oxide Films, Vol 4, Marcel Dekker Inc., New York 1976.

[45] K. Wefers, G.M. Bell, Oxides and Hydroxides of Aluminium, Technical Paper No. 19, Alcoa Research Laboratories 1972.

[46] L. Young, *Anodic Oxide Films*. Academic Press, London, New York 1961.

[47] *Oxides and Oxide Films* (J.W.Diggle, ed.), Marcel Dekker, New York 1973.

[48] L. Reschke in Korrosion und Korrosionsschutz (F. Tödt ed.), DeGruyter, Berlin, 1961.

[49] M. Stratmann, R. Feser and A.Leng, *Electrochim. Acta* **39** (1994) 1207.

[50] H. Leidheiser, W. Wang, L. Igetoft, *Prog. Org. Coat*. **11** (1983) 19.

[51] M. Stratmann, A. Leng, W. Fürbeth, H. Streckel, H. Gehmecker, K.H. Große-Brinkhaus, *Prog. Org. Coat*. **27** (1996) 261.

[52] W. Fürbeth, M. Stratmann, *Prog. Org. Coat*. **39** (2000) 23.

[53] A. Leng, H. Streckel, M. Stratmann, *Corr. Sci.* **41** (1999) 547.

[54] A. Leng, H. Streckel, M. Stratmann, *Corr. Sci.* **41** (1999) 579.

[55] A. Leng, H. Streckel, K. Hofmann, M. Stratmann, *Corr. Sci*. **41** (1999) 599.

[56] R. Posner, Thesis, Universität Paderborn (2009).

[57] W.S. Tait and K.A. Handrich, *Corrosion* **50** (1994) 373.

[58] T.N. Nguyen and J.B. Hubbard, *J. Coat. Technol.* **63** (1991) 43.

[59] K. Wapner, Thesis, Ruhr-Universität Bochum (2006).

[60] W. Fürbeth, M. Stratmann, *Corr. Sci.* **43** (2001) 207.

[61] W. Fürbeth, M. Stratmann, *Corr. Sci.* **43** (2001) 229.

[62] W. Fürbeth, M. Stratmann, *Corr. Sci.* **43** (2001) 243.

[63] J.M.C. Mol, B.R.W. Hinton, D.H. Van der Weijde, J.H.W. De Wit and S. Van der Zwaag, *J. Mater. Sci.* **35** (7) (2000) 1629.

[64] W. Funke, *Ind. Eng. Chem. Prod. Res. Dev*. **24** (1985) 343.

[65] J.R.H. Leidheiser, *Corrosion* **38** (1982) 374.

[66] R. T. Ruggeri and T. R. Beck, *Corrosion*, **39**, 452 (1983).

[67] T. Narayanan, *Rev. Adv. Mater. Sci*. **9** (2) (2005) 130.

[68] F.W. Eppensteiner, M.R. Jenkins, *Met. Finish.* **98** (1) (2000) 497.

[69] E.P. Plueddemann, *Silane Coupling Agents,2nd edn. Plenum Press*, New York (1990).

[70] Franquet, J. De Laet, T. Schram, H. Terryn, V. Subramanian, W.J. van Ooij, J. Vereecken, *Thin Solid Films* **384** (2001) 37.

[71] J. Bouchet, G. M. Pax, Y. Leterrier, V. Michaud, J.-A. E. Manson, *Compos. Interfaces* **13** (7) (2006) 573.

[72] N. Fink, B.Wilson, G.Grundmeier, *Electrochim. Acta* **51** (2006) 2956.

[73] B.Wilson, N.Fink, G.Grundmeier, *Electrochim. Acta* **51** (2006) 3066.

[74] P. Thissen, M. Valtiner, G. Grundmeier, *Langmuir* **26** (1) (2010) 156.

[75] M. Maxisch, C. Ebbert, B. Torun, N. Fink, T.de los Arcos, J. Lackmann, H.J. Maier, G. Grundmeier, *Appl. Surf. Sci*. **257** (2011) 2111.

[76] K. Wapner, M. Stratmann, G. Grundmeier, *Int. J. Adhes. Adhes.* **28** (1-2) (2008) 59.

[77] M. Santa, R. Posner, G. Grundmeier, *J. Electroanal. Chem.* **643** (1-2) (2010) 94.

[78] M.P. Desimone, G. Grundmeier, G. Gordillo, S.N. Simison, *Electrochim. Acta* **56** (8) (2011) 2990.

[79] E.P. Plueddemann, Silane *Coupling Agents, Plenum Press*, New York (1982).

[80] K.L. Mittal , *Silanes and Other Coupling Agents*, VSP, Utrecht (1992).

[81] K. Wapner and G. Grundmeier, *Adv. Eng. Mater*. **6** (2004) 163.

[82] K. Wapner, M. Stratmann, G. Grundmeier, *Electrochim. Acta* **51** (2006) 3303.

[83] G. Grundmeier, C. Reinartz, M. Rohwerder, M. Stratmann, *Electrochim. Acta* **43** (1998) 165.

[84] M. Rohrweiler, M. Stratmann and G. Grundmeier in Corrosion Mechanisms in Theory and Practice, Third Edition, ed. P.Marcus, *CRC Press* (Taylor and Francis), Boca Ranton, (2012) 617.

[85] K. Wapner and G. Grundmeier, *Surf. Coat. Technol*., **200** (1-4) (2005) 100.

[86] E.P. Plueddemann, *Silane Coupling Agents,2nd edn. Plenum Press*, New York (1990).

[87] Wang, H. Tang, T. Cao, S. O. Salley, K.Y. Simon Ng, *J. Colloid Interface Sci.* 291 (2005) 438.

[88] W. J. van Ooij and D. Zhu, *Corrosion* **57** (2001) 413.

[89] M-L. Abel, R. P. Digby, I. W. Fletcher, J. F. Watts, *Surf. Interface Anal.* **29** (2000) 115.

[90] C.M. Mustafa and S.M. Shahinoor Islam Dulal, *Corrosion* **52** (1) (1996) 16.

[91] A.K. Bairamov and S.C. Verdiev, *Brit. Corr. Jour.* **27** (2) (1992) 128.

[92] M.S. Vukasovich, *Mat. Perf*. **29** (5) (1990) 48.

[93] Y.N. Mikhailovskii and G.A. Berdzenishvili, *Prot. Met*. **21** (6) (1986) 704.

[94] G.M. Treacy, G.D. Wilcox, M.O.W. Richardson, *J. Appl. Electrochem.* **29** (1999) 647.

[95] E. Almeida, T.C. Diamantino, M.O. Figueiredo, C. Sa, *Surf. Coat. Tech*. **106** (1998) 8.

[96] A.A.O. Magalhaes, I.C.P. Margarit, O.R. Mattos, *J. Electroanal. Chem.* **572** (2004) 433.

[97] D. Basher and A. Kingsbury, *Trans. Faraday Soc.* **54** (1958) 1214.

[98] J.B. Lusdem and Z. Szklarska-Smialowska, *Corrosion* **34** (5) (1978) 169.

[99] B.S. Scerry, G.E. Thompson G.C. Wood, et al., *Proc. 6th Eur. Symp. On Corrosion Inhibitors*, Ferrara vol. 1 (1985) 521.

[100] N.N. Greenwood and A. Earnshaw, Chemistry of the Elements, Pergamon Press, Oxford, England (1984) 1437.

[101] T.J. Haley, *J. Pharm. Sci.* **54** (1965) 633.

[102] P.J. Falconnet, *J. Alloys and Comp.* **192** (1993) 114.

[103] G.K. Muecke and P. Möller, *Sci. Amer.* **258** (1) (1988) 72.

[104] S.R. Taylor, *Geochim. Cosmochim. Acta* **28** (1964) 1273.

[105] S. Mrowec, *Werks. Korr*. **38** (10) (1987) 536.

[106] W.J. Quadakkers, H. Schuster and P.J. Ennis (eds.), *High Temperature Corrosion of metals* (1988) 353.

[107] R.C. Lobb and M.J. Bennett, *Werks. Korr*. **41** (12) (1990) 657.

[108] M.F. Stroosnijder, M.J. Bennet, V. Guttmann, J.F. Norton and J.H.W. deWit, *Oxidation of Metals* **35** (1-2) (1991) 19.

[109] R.C. Lobb and M.J. Bennett, *Oxidation of Metals* **35** (1-2) (1991) 35.

[110] Y.C. Lu and M.B. Ives, *Corr. Sci*. **34** (11) (1993) 1773.

[111] B.R.W. Hinton and L. Wilson, *Corr. Sci*. **29** (8) (1989) 967.

[112] S.J. Li, *Mat. Prot*. **26** (11) (1993) 6.

[113] S.J. LI, J.P. He, W.H. Chen and Y. Zhang, *Jour. of Rare Earths* **12** (1) (1994) 18.

[114] N. Verma, W.R. Singh, S.K. Tiwari and R.N. Singh, *Brit. Corr. Jour*. **25** (2) (1990) 131.

[115] R.N. Singh, S.K. Tiwari and W.R. Singh, *J. Appl. Electrochem*. **55** (12) (1992) 1175.

[116] F. Czrewinski and W.W. Smeltzer, *Oxidation of Metals* **40** (5-6) (1993) 503.

[117] H.S. Isaaca, A.J. Davenport and A. Shipley, *J. Electrochem. Soc*. **138** (2) (1991) 390.

[118] P.K. Lai and B.R.W. Hinton, Paper No 336. In *13th International Corrosion Conference*, Melbourne, Australia, Nov. 1996.

[119] G. Aguilar, J.C. Colson, L. Dupont and A. Foissy, *Rev. Metall. Ca. Inf. Tech*. **90** (12) (1993) 1607.

[120] T. Suwa, *Corr. Eng.* **37** (2) (1988) 73.

[121] S.K. Mitra, S.K. Roy and S.K. Bose, *Oxidation of Metals* **39** (3-4) (1993) 221.

[122] Y.C. Lu and M.B.Ives, *Corr. Sci.* **37** (1) (1995) 145.

[123] S. Bernal, F.J. Botana, J.J. Calvino, M.A. Cauqui, M. Marcos, J.A. Perez and H. Vidal, *J. Alloys Comp*. **225** (1995) 638.

[124] B.R.W. Hinton, D.R. Arnott and N.E. Ryan, *Met. Forum* **7** (4) (1984) 11.

[125] B.R.W. Hinton, N.E. Ryan, D.R. Arnott P.N. Trathen, L. Wilson and B.E. Williams, *Corr. Austral*. **10** (3) (1985) 12.

[126] B.R.W. Hinton, D.R. Arnott and N.E. Ryan, *Mater. Forum* **9** (3) (1986) 162.

[127] B.R.W. Hinton, in *Proc. 19th REPC*, Kentucky (1991).

[128] A.K. Bhattamishra and M.K. Banerjee, *Z. Metallkd*. **84** (10) (1993) 734.

[129] A.J. Aldykewicz, H.S. Isaacs and A.J. Davenport, *J. Electrochem. Soc.* **142** (10) (1995) 3342.

[130] B.R.W. Hinton, *Met. Finish*. **89** (1991) 15.

[131] B.R.W. Hinton, *Met. Finish.* **89** (1991) 55.

[132] L. Wilson and B.R.W. Hinton, Austr. Patent P10649, March 1987.

[133] F. Mansfeld, Y. Wang and H. Shih, *J. Electrochem. Soc.* **138** (12) (1991) 74.

[134] F. Mansfeld, Y. Wang, S. Lin and L. Kwiatkowski, *Proc. 12th Int. Corrosion Congr*, Housten, vol. 1 (1993) 219.

[135] Yu Xingwen, Cao Chunan, Yao Zhiming, Zhou Derui and Yin Zhongda, *Corros. Sci*. 43 (2001) 1283.

[136] J.H. Nordlien, J.C. Walmsley, H. Osterberg, K. Nisancioglu, *Surf. Coat. Technol*. **153** (2002) 72.

[137] T. Scram, G. Goeminne, H. Terryn, W. Vanhoolst, *Trans. Institute Met. Finish.* **70** (3) (1995) 91.

[138] K. Wapner, M. Stratmann and G. Grundmeier, *Int. J. Adhes. Adhes.**28*** (2007) 59.

[139] E. Jaehne, S. Oberoi and H.J.P Adler, *Prog. Org. Coat*. **61** (2008) 211.

[140] S. Oberoi, E. Jaehne and H.J.P. Adler, *Macromol. Symp.***217** (2004) 147.

[141] J. Mathiyarasu, S.S. Pathak and V. Yegnaraman, *Corr. Rev.* **24** (2006) 307.

[142] A. Algata, I. Felhösi, I. Bertoti, and E. Kálmán, *Corr. Sci.* **50** (2008) 1644.

[143] D.Q. Zhang, X.M. He, Q.R. Cai, L.X. Gao and G.S. Kim, *Thin Solid films* **518** (2010) 2745.

[144] F.P. Zamborini and R.M.Crooks, *Langmuir* **44** (1998) 3279.

[145] D.L. Allara and R.G. Nuzzo, *Langmuir* **1** (1985) 45.

[146] I. Maege, E. Jaehne, A. Henke, H.J.P. Adler, C. Bram, C. Jung and M. Stratmann *Prog. Org. Coat.* **34** (1998) 1.

[147] M. Maxisch, C. Ebbert, B. Torun, N. Fink, T. de los Arcos, J. Lackmann, H.J. Maier and G. Grundmeier, *Appl. Sur. Sci.* **257** (2011) 2011.

[148] I. Doudevski and D.K. Schwartz, *Appl. Surf. Sci*. **175-176** (2001) 17.

[149] E.M. Cheadle, D.N. Batchelder, S.D. Evans, H.L. Zhang, H. Fukushima, S. Miyashita, M. Graupe, A. Puck, O.E. Shmakova, R. Jr. Colorado and T.R. Lee, *Langmuir* **17** (2001) 6616.

[150] D.A. Hutt and G.I. Leggett *J. Phys. Chem.* **100** (1996) 6657.

[151] E.R. Vago, K. de Weldige, M. Rohweder and M. Stratmann, *Fresenius J. Anal. Chem.* **353** (1995) 316.

[152] L.H. Guo, J.S. Facci, G.M. McLendon and R. Mosher *Langmuir* **10** (1994) 4588.

[153] R.G. Nuzzo, L.H. Dubois and D.L. Allara,. *J. Am. Chem. Soc.***112** (1990) 558.

[154] P. Thissen, M. Valtiner and G. Grundmeier, *Langmuir* **26** (2010) 156.

[155] E. Hoque, J.A. DeRose, G. Kulik, P. Hoffmann, H.J. Mathieu and B. Bhushan, *J. Phys. Chem. B* **110** (2006) 10855.

[156] K.M. Pertays, G.E. Thompson and M.R. Alexander, *Surf. Interf. Anal*. **36** (2004) 1361.

[157] J. v. d. Brand, O. Baljiev, P.C.J. Beentjes, H. Terryn and J.H.W. de Wit, *Langmuir* **20** (2004) 6308.

[158] J. v. d. Brand, O. Baljiev, P.C.J. Beentjes, H. Terryn and J.H.W. de Wit, *Langmuir* **20** (2004) 6318.

[159] N. Adden, L.J. Gamble, D.G. Castner, A. Hoffmann, G. Gross and H. Menzel, *Langmuir* **22** (2006) 8197.

[160] R. Quinones and E.S. Gawalt, *Langmuir* **23** (2007) 10123.

[161] P.H. Mutin, v. Lafond, A.F. Popa, M. Granier, L. Markey and A. Dereux, *Chem. Mater.* **16** (2004) 5670.

[162] S. Pawsey, K. Yach and L. Reven, *Langmuir* **18** (2002) 5205.

[163] C. Viornery, Y. Chevolot, D. Léonard, B.O. Aronsson, P. Péchy, H.J. Mathieu, P. Descouts and M. Grätzel, *Langmuir* **18** (2002) 2582.

[164] E.S. Gawalt, M.J. Avaltroni, N. Koch and J. Schwartz, *Langmuir* **17** (2001) 5736.

[165] G. Guerrero, H.P. Mutin and A. Vioux, A. *Chem. Mater.* **13** (2001) 4367.

[166] M. Giza, P. Thissen and G. Grundmeier, *Langmuir* **24** (2008) 8688.

[167] A.V. Pocius in Adhesion and Adhesive Technology: An Introduction, 2nd ed.; Hanser Gardner, Cincinatti (2002).

[168] P.J. Frantzis, *Mater. Civil Eng.* **20** (2008) 635.

[169] W. Cloete and W. Focke, *Int. J. Adhes. Adhes.* **30** (2010) 208.

[170] G.B. Wiggins and D.C. Currie. In Trichoptera Families; R.W. Merritt, K.W. Cummins and M.B., Eds. Kendall/Hunt Publishing Company: Dubuque, Iowa (2008).

[171] J.H. Waite, *Chemtech.* **17** (1987) 692.

[172] M Wiegemann, *Aquat. Sci*. **67** (2005) 166.

[173] R.A. Jensen and D.E. Morse*, J. Comp. Physiol. B* **158** (1988) 317.

[174] A.J. Kohn, *Pacific Sci*. **XV** (1961) 163.

[175] L. Petrone, R. Easingwood, M.F. Barker and A.J. McQuillan, *J. R. Soc. Interface* **8** (2011) 410.

[176] L.A. Thomas and C.O. Hermans, *Biol. Bull*. **169** (1985) 675.

[177] J.W. Costerton, The Biofilm Primer, Springer, Berlin (2007).

[178] D. Crisp, G. Walker, G. Young and A. Yule, *J. Colloid Interface Sci*. **104** (1985) 40.

[179] M. Wiegemann and B. Watermann, *J. Adhes. Sci. Technol*. **17** (2003) 1957.

[180] N. Aldred, L. Ista, M. Callow, J. Callow, G. Lopez and A. Clair, *J. R. Soc. Interface* **3** (2006) 37.

[181] J. Callow, M. Callow, L. ista, G. Lopez and M. Chaudhury, *J. R. Soc. Interface* **2** (2005) 319.

[182] C.J. Kavanagh, M.P. Schultz, G.W. Swain, J. Stein, k. Truby and C.D. Wood, *Biofoulding* **17** (2001) 155.

[183] J.R. Burkett, J.L. Wojtas, J.L. Cloud and J.J. Wilkers, *J. Adhes.* **85** (2009) 601.

[184] H. Zhao and J.H. Waite, *J. Bio. Chem.* **281** (2006) 26150.

[185] H. Zhao, N.B. Robertson, S.A. Jewhurst and J.H. Waite *J. Biol. Chem.* **281** (2006) 11090.

[186] J.H. Waite and M.L.Tanzer, *Science* **212** (1981) 1038.

[187] H. Lee, N.F. Scherer and P.B. Messersmith, *Proc. Natl. Acad. Sci*. **29** (2006) 12999.

[188] A.A. Ooka and R.L. Garrell, *Biopolymers* **57** (2000) 92.

[189] J.H. Waite and X. Qin*, Biochemistry* **40** (2001) 2887.

[190] J.H. Waite, R.A. Jensen and D.E. Morse, *Biochemistry* **31** (1992) 5733.

[191] H. Zhao, C. Sun, R.J. Steward and J.H. Waite, *J. Biol. Chem.* **280** (2005) 42938.

[192] R.J. Steward, J.C. Weaver, D.E. Morse and J.H. Waite, *J. Exp. Biol.* **207** (2004) 4727.

[193] R.J. Steward and C.S. Wang, *Biomacromolecules* **11** (2010) 969.

[194] J.L. Dalsin, B.H. Hu and B.P. Messersmith, *J. Am. Chem. Soc*. **125** (2003) 4253.

[195] S. Saxer, C. Portmann, S. Tosatti, K. Gademann, S. Zurcher and M. Textor, *Macromolecules* **43** (2009) 1050.

[196] B. Malisova, S. Tosatti, M. Textor, K. Gademann and S. Zurcher, *Langmuir* **26** (2010) 4018.

[197] J.L. Dalsin, L. Lin, S. Tosatti, J. Voros, M. Textor and P.B. Messersmith, *Langmuir* **21** (2005) 640.

[198] G. Westwood, T.N. Horton and J.J. Wilker, *Macromolecule*s **40** (2007) 3960.

[199] M. Yu and T.J. Deming, *Macromolecules* **31** (1998) 4739.

[200] M. Yu, J. Hwang and T.J. Deming *J. Am. Chem. Soc*. **121** (1999) 5825.

[201] Q. Lin, D. Gourdon, C. Sun, N. Holten-Andersen, T.H. Andersen, J.H. Waite and J.N. Israelachvili, *Proc. Natl. Acad. Sci.* **104** (2007) 3782.

[202] M. McBride and L. Wesselink, *Environ. Sci. Technol.* **22** (1988) 703.

[203] P. Connor, K. Dobson and A. McQuillan, *Langmiur* **11** (1995) 4193.

[204] H. Zhao, N.B. Robertson, S.A. Jewhurst and J.H. Waite, *J. Biol. Chem.* **281** (2006) 11090.

[205] D. Vasudevan and A. Stone, Environ. *Sci. Technol.* **30** (1996) 1604.

[206] A. Furubayashi, S. Hiradate and Y.Fujii, *J. Chem. Ecol*. **33** (2007) 239.

[207] E. Elzinga and D. Sparks, *J. Colloid Interface Sci*. **308** (2007) 53.

[208] R. Rahnemaine, T. Hiemstra and W. van Riemsdijk, *Langmuir* **23** (2007) 3680.

[209] P. Connor and A. McQuillan, *Langmuir* **15** (1999) 2916.

[210] S.Y. Hui, A. Herve and J. Kiplinger, JCT Coatings Tech. 2 (2005) 44.

[211] R. de Majistre, U.S. Patent, PPG Industries Inc., Pittsburgh, PA 3,754,972 (1973).

[212] R. Janda, B. Homburg and B. Eppinger, U.S. Patent, Kulzer & Co, GmbH Wehrheim, DE 4,640,936 (1987).

[213] M.E. Yu and T.J. Deming *Macromolecules* **31** (1998) 4739.

[214] H. Tatchata, A. Mochizuki, K. Ohkawa, M. Yamada and H. Yamamoto, *Adhes. Sci. Technol.* **15** (2001) 1003.

[215] H. Yamamoto, S. Kuno, A. Nagai, A. Nishida, S. Yamauchi and K. Ikeda Int. *J. Biol. Macromol.* **12** (1990) 305.

[216] M. Yu and T.J. Deming *Polym. Mater. Sci. Eng.* **79** (1998) 248.

[217] T.J. Deming *Curr. Opin. Chem. Biol.* **3** (1999) 100.

[218] T.J. Deming, M. Yu and J. Hwang *Polym. Mater. Sci. Eng.* **80** (1999) 471.

[219] J.L. Dalsin, B.-H. Hu, B.P. Lee and P.B. Messersmith *J. Am. Chem. Soc.* **125** (2003) 4253.

[220] M.E. Yu, J.Y. Hwang and T.J. Deming *J. Am. Chem. Soc.* **121** (1999) 5825.

[221] A. Statz, J. Finlay, J. Dalsin, M. Callow J.A. Callow and P.B. Messersmith Biofoulding 22 (2006) 391.

[222] X. Fan, L. Lin and P.B. Messersmith Biomacromolecules 7 (2006) 2443.

[223] A.R. Statz, R.J. Meagher, A.E. Barron and P.B. Messersmith J. Am. Chem. Soc. 127 (2005) 7972.

[224] S.M. Kang, I. You, W.K. Cho, H.K. Shon, T.G. Lee, I.S. Choi, J.M. Karp and H. Lee *Angew. Chem. Int. Ed. Engl.* **49** (2010) 9401.

[225] B.P. Lee, J.L. Dalsin and P.B. Messersmith *Biomacromolecules* **3** (2002) 1038.

[226] C.E. Brubaker, H. kissler, L.J. Wang, D.B. Kaufmann and P.B. Messersmith *Biomaterials* **31** (2010) 420.

[227] H. Lee, B.P. Lee and P.B. Messersmith *Nature* **448** (2007) 338.

[228] H. Shao and R.J. Stewart *Adv. Mater.* **22** (2010) 729.

[229] H. Shao, K.N. Bachus and R.J. Stewart *Macromol. Biosci.* **9** (2009) 464.

[230] B.D. Winslow, H. Shao, R.J. Stewart and P.A. Tresco *Biomaterials* **31** (2010) 9373.

[231] S. Kaur, G.M. Weerasekare and R.J. Stewart *ACS Appl. Mater. Interfaces* **3** (2011) 941.

[232] C.Stromberg, P.Thissen, I.Klueppel, N.Fink and G.Grundmeier, *Electrochim. Acta* **52** (2006) 804.

[233] M.F. Montemor, A.M. Simoes, M.G.S. Ferreira, B.Williams and H.Edwards *Prog. Org. Coat*. **38** (2000) 17.

[234] K.Yamamoto and H. Ishida, V*ibrational Spectrocoy* **8** (1994) 1.

[235] H. Günzler and H.-U. Gremlich, IR-Spektroskopie, Wiley-VCH 2003.

[236] G.Grundmeier, *Dissertation* Tech. Fak. Universität Erlangen-Nürnberg (1997).

[237] S.A. Francis and A.A. Ellison, *J. Opt. Soc. Am*. **49** (2) 131.

[238] R.G. Greenler, *J. Chem. Phys*. **44** (1) 310.

[239] J.F. Moulder, W.F. Stickle, P.E. Solbol and K.D. Bomben; Handbook of *X-ray Photoelectron Spectroscopy* J. Chastain, R.C. King, Ed. Physical Electronics, Inc. USA (1995) 9.

[240] M.P. Seah, *Vacuum* **34** (1984) 463.

[241] J.M. Hollas *Modern Spectroscopy 4th ed*. Wiley, England (2004) 290.

[242] F.Reniers and C. Tewell, *J. Electron. Spectrosc. Relat. Phenom.* **142** (2005) 1.

[243] M. Stöcker, *Microporous Mater*. **6** (1996) 235.

[244] H. Seiler, *Ultramicroscopy* **17** (1985) 1.

[245] I. Klüppel, Thesis, University of Paderborn (2008).

[246] G.Wedler, *Lehrbuch der physikalischen Chemie*, 5.Aufl. Wiley VCH, Weinheim (2004).

[247] P.W. Atkins, *Physikalische Chemie*, 3.Aufl., Wiley VCH, Weinheim (2001).

[248] C.H. Hamann, W. Vielstich, *Elektrochemie*, 3.Aufl., Wiley VCH, Weinheim (1998).

[249] W. Schmickler, *Grundlagen der Elektrochemie*, Vielweg, Braunschweig (1996).

[250] M. Stratmann and H. Streckel, *Corr. Sci.* **30** (1990) 681.

[251] R. Gomer and G. Tryson, *J. Chem. Phys.* **66** (1987) 4413.

[252] W. Zisman, *Rev. Sci. Instrum*. **3** (1932) 367.

[253] H. Vogel, *Gerthsen Physik*, Springer Verlag, Berlin (1997).

[254] A.J. Bard and L.R. Faulkner, *Electrochemical Methods, Fundamentals and Applications*, John Wiley & Son, Hoboken (2001).

[255] J.R. MacDonald, Impedance Spectroscopy; Emphasizing solid Materials and Systems, John Wiley & Son, New York (1987).

[256] Gamry, *Basics of Electrochemical Impedance Spectroscopy* (2008).

[257] F. Mansfeld, *J. Appl. Electrochem.* **25** (1995) 1145.

[258] A. Losch, and J.W. Schultze *Appl. Surf. Sci.* **52** (1991) 29.

[259] E. Klusmann, U. König and J.W. Schultze, *Mater. Corros.* **46** (1995) 83.

[260] A. Losch and J.W. Schultze, *Electroanal. Chem.* **359** (1993) 39.

[285] A. Becker and M. Schmidt Mac*romol. Chem. Macromol. Symp*. **50** (1991) 249.

[286] G. Grundmeier, P. Thiemann, J. Carpentier, N. Shirtcliffe, and M. Stratmann, *Thin Solid Films*, **446** (2004) 61.

[287] C. Rau and W. Kulisch, *Thin Solid Films*, **249** (1994) 28.

[288] D. Theirich, C. Soll, F. Leu, and J. Engemann, *Vacuum*, **71** (2003) 349.

[289] M. Fernandez-Garcia and M. Y. M. Chiang, *J. Appl. Polym. Sci.*, **84** (2002) 1581.

[290] A. Franquet, C. Le Pen, H. Terryn and J. Vereecken, *Electrochimica Acta* **48** (2003) 1245.

[291] D.*G.* Kurth and T. Bein, *Langmuir,* **11** (1995) 3061-3067.

[292] C.M. Phillipps and K.S. Mazdiyasni, *J. Am. Ceram. Soc*., **54** (5) (1971) 254.

[293] C. Pecharroman, M. Ocana and C.J. Serna, *J. Appl. Phys.* **80** (6) (1996) 3479.

[294] D. A. Neumayer and E. Cartier, *J. Appl. Phys.* **90** (4) (2001) 1801.

[295] M. Niknahad, S. Moradian and S.M. Mirabedini, *Corr. Sci.* **52** (2010) 1948.

[296] R.Posner, K.Wapner, M.Stratmann and G.Grundmeier, *Electrochim. Acta* **54** (2009) 891.

[297] R.Posner, T.Titz, K.Wapner, M.Stratmann and G.Grundmeier, *Electrochim. Acta* **54** (2009) 900.

[298] K. Itano, J. Choi and M.F. Rubner, *Macromolecules* **38** (2005) 3450.

[299] D.K. Kim, S.W. Han, C.H. Kim, J.D. Hong and K. Kim, *Thin Solid Films* **350** (1999) 153.

[300] J. Gallardo, A. Duran, D. Di Martino and R.M. Almeida, J*. Non-Cryst. Solids* **298** (2002) 219.

[305] J.T.G. Overbeek, *J. Colloid Interf. Sci*. **58** (1977) 408.

[306] D.G. Abebe and T.R. Farhat, *Soft Matter* **6** (2010) 1325.

[307] A.I. Petrov, A.A. Antipo and, G.B. Sukhorukov*, Macromolecules* **36** (2003) 10079.

[308] J. Suh, H.J. Paik and B.K. Hwang, *Bioorg. Chem*. **22** (1994) 318.

[309] Y. Yoshikawa, H. Matsuoka and N. Ise*, Br. Polym. J*. **18** (1986) 242.

[310] H. Ochiai, Y. Anabuki, O. Kojima, K. Tominaga and I. Murakami, *J. Polym. Sci., Part B* **28** (1990) 233.

[311] M.M. Fang, C.H. Kim, G.B. Saupe, H.N. Kim, C.C. Waraksa, T. Miwa, A. Fujishima and T.E. Mallouk, *Chem. Mater*. **11** (1999) 1526.

[312] M. Rohrweiler, K. de Weldige and M. Stratmann, *J. Solid State Electrochem*. **2** (1998) 88.

[313] F. Sinapi, L. Forget, J. Delhalle and Z. Mekhalif, *Appl. Surf. Sci*. **212-213** (2003) 464.

[314] A.R. Noble-Luginbuhl and R.G. Nuzzo, *Langmuir* **17** (2001) 3937.

[315] F. Sinapi, T. Issakova, J. Delhalle and Z. Mekhalif, *Thin Solid Films* **515** (2007) 6833.

[316] Z. Mekhalif, L. massi, F. Guittard, S. Geribaldi and J. Delhalle, *Thin Solid Films* **405** (2002) 186.

[317] H. Zang and S. Baldelli, *J. Phys. Chem. B* **110** (2006) 24062.

[318] C Nogues and P. Lang*, Langmuir* **23** (2007) 8385.

[319] C. Yan, M. Zharnikov, A. Gölzhäuser and M. Grunze, *Langmuir* **16** (2000) 6208.

[320] M. Volmer-Uebing and M. Stratmann, *Appl. Surf. Sci*. **55** (1992) 19.

[321] H.P. Zhang, C. Romero and S. Baldelli*, J. Phys. Chem. B* **109** (2005) 15520.

[322] Z. Mekhalif, J. Riga, J.-J. Pireaux and J. Delhalle, *Langmuir* **13** (1997) 2285.

[323] L. Tortech, Z. Mekhalif, J. Delhalle, F. Guittard and S. Geribaldi, *Thin solid films* **491** (2005) 253.

[324] Z. Mekhalif, F. Laffineur, N. Couturier and J. Delhalle, *Langmuir* **19** (2003) 637.

[325] Z. Mekhalif, J. Delhalle, , J.-J. Pireaux, S. Noel, F. Houze and L. Boyer, S*urf. Coat. Technol*. **100-101** (1998) 463.

[326] F. Laffineur, Z. Mekhalif, L. Tristani and J. Delhalle*, J. Mater. Chem.* **15** (2005) 5054.

[327] F. Berger, J. Delhalle and Z. Mekhalif, *Electrochim. Acta* **53** (2008) 2852.

[328] I. Maege, E. Jaehne, A. Henkel, H.-J. P. Adler, C. Bram, C. Jung and M. Stratmann, *Macromol. Symp.* **126** (1997) 7.

[329] I. Maege, E. Jaehne, A. Henkel, H.-J. P. Adler, C. Bram, C. Jung and M. Stratmann, *Progr. Org. Coat.* **34** (1998) 1.

[330] B. Adolphi, E. Jahne, G. Busch and X.D. Cai, *Anal. Bioanal Chem.* **379** (2004) 646.

[331] R.G. Parson, *Science* **151** (1966) 172.

[332] L. Horner, *Chem. Ztg.* **100** (1976) 247.

[333] M. Iannuzzi, J. Kovac, and G. S. Frankel, *Electrochim. Acta*, **52** (2007) 4032.

[334] K. S. Ralston, S. Chrisanti, T. L. Young, and R. G. Buchheit, *J. Electrochem. Soc*. **155** (2008) C350.

7 Abbreviations

Acronyms

Al6016	Aluminium alloy 6016
AFM	atomic force microscopy
γ-APS	γ -aminopropyltriethoxysilane
At%.	atomic percentage
ATR-IR	Attenuated Total Reflection-Infrared Spectroscopy
a.u.	arbitrary unit
CA	contact angle
CRS	Cold rolled steel
CV	cyclovoltammetry
DLS	dynamic light scattering
DLVO	named after **D**erjaguin, **L**andau, **V**erwey and **O**verbeek
DTGS	deuterium triglycinsulfate
e.g.	exempli gratia
EIS	Electrochemical Impedance Spectroscopy
etc.	et cetera
eV	electron volt
Fig.	Figure
FE-SEM	Field-Emission Secondary Electron Microscopy
FT-IRRAS	Fourier-Transformed Infrared-Reflection-Absorption-Spectroscopy
HBW	half-band-width
HDG	Hot dipped galvanized steel
LSV	Linear sweep voltammetry
MCT	mercury cadmium telluride
Mg-LDH-VO_3	Magnesium-layered double hydroxide-vanadate
min	minute
MTBT	2-(methylthio)benzothiazole
NDL	Nernst diffusion layer
OCP	Open Circuit Potential
ODPA	octadecyl phosphonic acid
ODT	octadecyl thiol
PDMAEMA	Poly(dimethylamino)ethyl methacrylate
pH	potentia Hydrogenii
ppm	parts per million
PZC	point of Zero Charge
SAM	self-assembled monolayer
SHE	Standard Hydrogen Electrode
SLS	Static light scattering
HR-SKP	Height-Regulated Scanning Kelvin Probe
TR-SLS	time resolved static light scattering
XPS	x-ray photoelectron spectroscopy
ZE	Electro galvanized steel

Latin symbols

a	activity
Å	Angstrom
A_2	second osmotic viral coefficient
A_3	third osmotic viral coefficient
c	concentration
C	capacitance
°C	degree Celsius
C_C	coating capacitance
C_{DL}	double layer capacitance
cm	centimeter
cm^{-1}	wavenumber
d	difference/or: distance/or: penetration depth
d_0	mean plate distance
E	energy
E	electric field
eV	electron volt
$E_{binding}$	binding energy
E_{corr}	corrosion potential
E_{kin}	kinetic energy
f	frequency
F	Faraday constant
g	gram
h	Planck constant/or: hour
Hz	hertz
i	current density
I	intensity
I_0	current amplitude or intensity of primary beam
K	Kelvin/or: constant factor
k_B	Boltzmann-constant
kHz	kilohertz
l	liter
ln	natural logarithm
M	molar mass
M_w	weight average molar mass
mm	millimetre
mV	millivolt
N_A	Avogardo constant
n_{sol}	refractive index of solution
n_{solv}	refractive index of solvent
dn/dc	refractive index increment
nm	nanometer
$pK_{1/2}$	pH value when half of the acid is ionized
Q	charge
Q_k	normal coordinate
r	radius
R_{el}	electrolyte resistance
R_C	coating resistance
R_{CT}	charge transfer resistance
R_θ	net scattering intensity
R_g	radius of gyration

R_h	hydrodynamic radius
s	second
t	time
T	temperature
U	voltage
U_0	voltage amplitude
Z	impedance
z_e	electron charge number

Greek symbols

α	polarizability
γ	degree of surface coverage
Δ	difference
ε_0	dielectric constant in vacuum
ε_r	material dependent dielectric constant
η	viscosity
θ	scattering angle
λ	wavelength
μ	chemical potential
μ_0	chemical potential for standard conditions
$\tilde{\mu}$	electrochemical potential
$\tilde{\mu}_e$	electrochemical potential of an electron
$\vec{\mu}$	dipole moment
μm	micrometer
ν	frequency
Φ	electron work function
φ	Galvani potential
χ	surface potential
ψ	Volta potential
ω	angular frequency
Ω	ohm

8 Appendix

8.1 EIS plots on modified hybrid-layers measured during oxygen corrosion

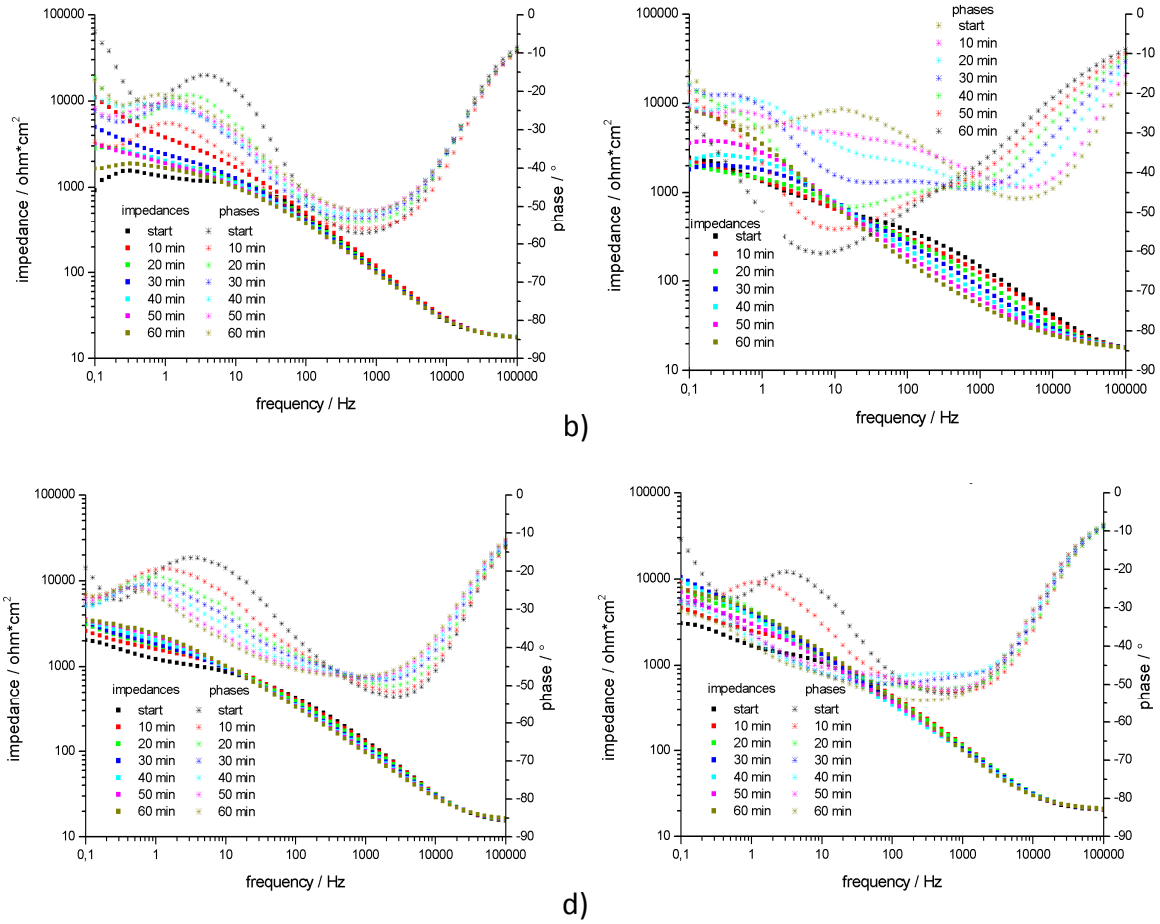

Fig. 8.1: Impedances and phases on ZE coated with a) hybrid layer b) copper-containing hybrid-layer c) hybrid-layer/PDMAEMA/0.5%MTBT and d) hybrid-layer/Mg-LDH-VO_3 within 60min impact of 0.5M NaCl.

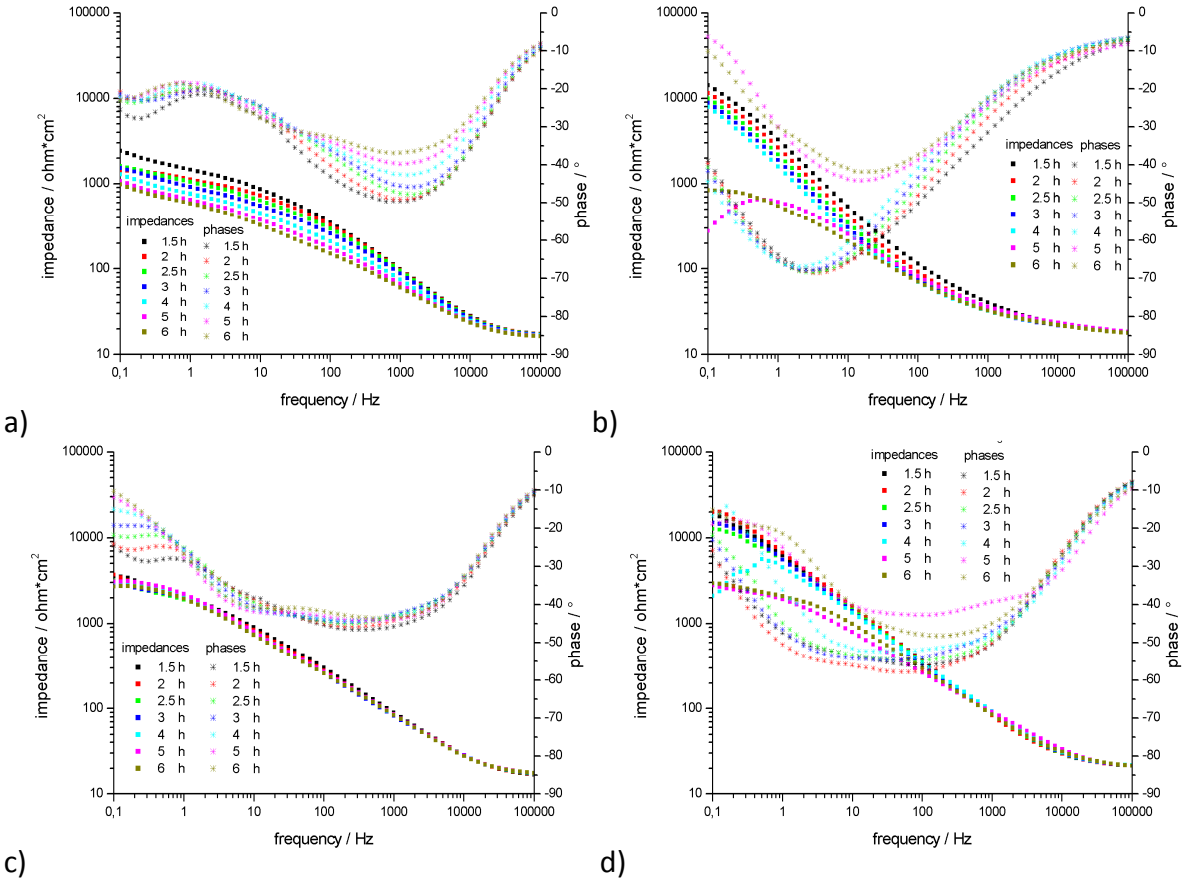

Fig. 8.2: Impedances and phases on ZE coated with a) hybrid layer b) copper-containing hybrid-layer c) hybrid-layer/PDMAEMA/0.5%MTBT and d) hybrid-layer/Mg-LDH-VO_3 after 1.5-6h impact of 0.5M NaCl.

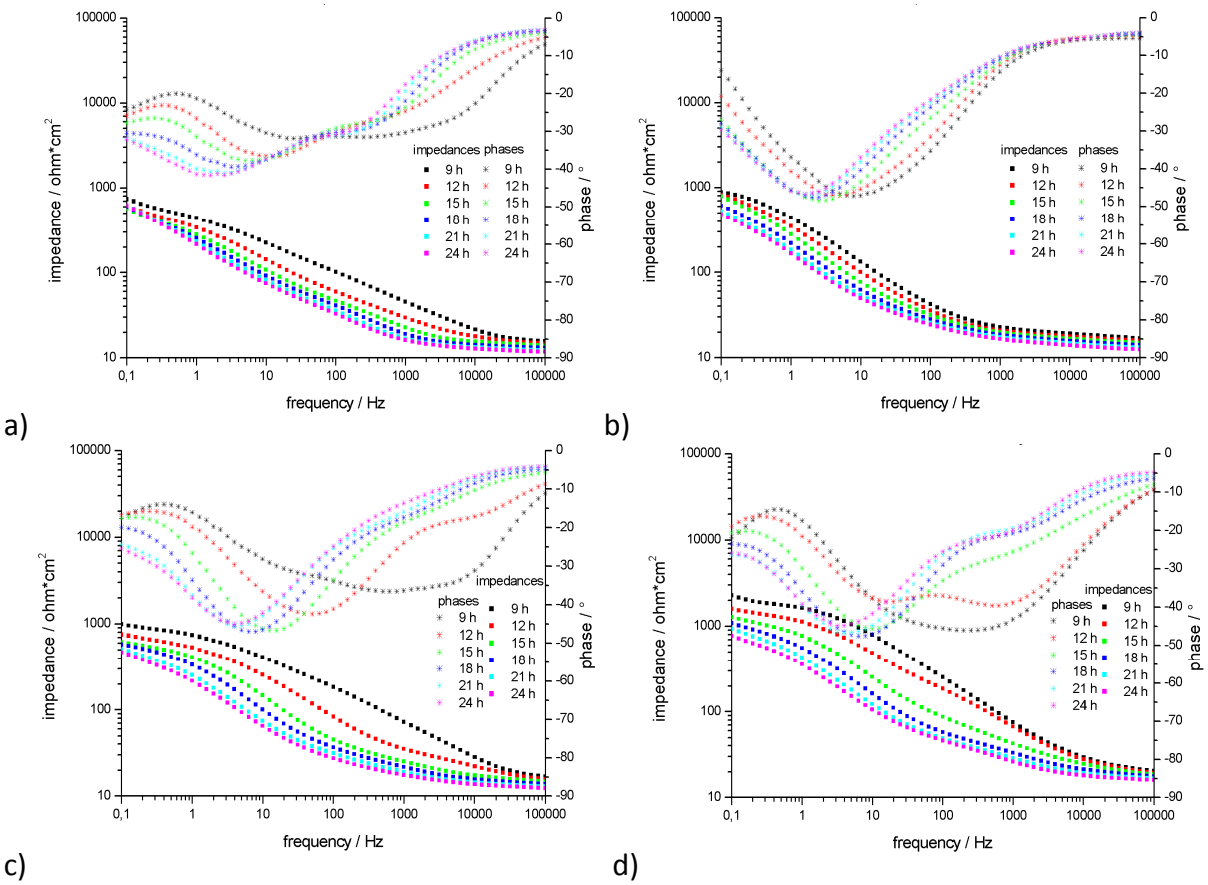

Fig. 8.3: Impedances and phases on ZE coated with a) hybrid layer b) copper-containing hybrid-layer c) hybrid-layer/PDMAEMA/0.5%MTBT and d) hybrid-layer/Mg-LDH-VO_3 after 9-24h impact of 0.5M NaCl.